Characterization and tailoring of MHz-repetition-rate XFEL pulses using dynamical diffraction in crystals

Dissertation zur Erlangung des Doktorgrades des Department Physik der Universität Hamburg

vorgelegt von

Ilia Petrov

Hamburg

2022

Eidesstattliche Versicherung

Hiermit versichere ich an Eides statt, die vorliegende Dissertationsschrift selbst verfasst und keine anderen als die angegebenen Hilfsmittel und Quellen benutzt zu haben.

02.11.2022   Ilia Petrov

Gutachter/innen der Dissertation:	Prof. Dr. Christian Schroer
	Prof. Dr. Anders Madsen
Zusammensetzung der Prüfungskommission:	Prof. Dr. Wolfgang J. Parak
	Prof. Dr. Christian Schroer
	Prof. Dr. Anders Madsen
	Dr. Harald Sinn
	Prof. Dr. Franz Kärtner
Vorsitzender der Prüfungskommission:	Prof. Dr. Wolfgang J. Parak
Datum der Disptutation:	17.10.2022
Vorsitzender Fach-Promotionsausschusses PHYSIK:	Prof. Dr. Wolfgang J. Parak
Leiter des Fachbereichs PHYSIK:	Prof. Dr. Günter H. W. Sigl
Dekan der Fakultät MIN:	Prof. Dr.-Ing. Norbert Ritter

Contents

Zusammenfassung

Freie-Elektronen-Röntgenlasern (XFELs) erzeugen Pulse von extrem kurzer Dauer, hoher räumlicher Kohärenz und hoher Intensität die einzigartige Experimente in der Materialforschung, Femtosekundenchemie und weiterer Forschungsfelder ermöglichen. Diffraktionsoptische Systeme werden an XFELs zur Charakterizierung und Modifikation der Pulse für die jeweiligen Experimente eingesetzt. Da jeder Puls aufgrund der stochastischen Natur der XFEL-Pulse individuelle spektrale Eigenschaften hat, ist eine pulsaufgelöste Diagnostik erforderlich. Stark gekrümmte Kristalle ermöglichen es, verschiedene Photonenenergien über einen breiten Winkelbereich zu beugen und somit das Energiespektrum des XFEL Pulses zu messen. In dieser Dissertation wird der Einfluss der Beugung eines gekrümmten Kristallspektrometers auf das Spektrum mittels dynamischer Diffraktion untersucht. Es wird gezeigt, dass die Kristalldicke das Auflösungsvermögen des Spektrometers begrenzt. Aufgrund der hohen Intensität der Pulse führt die durch die Absorption in den Kristallen verursachte Erwärmung zu einer erheblichen Gitterverzerrung, die die Leistung der jeweiligen optischen Instrumente beeinträchtigt. Ein Modell wurde entwickelt, um den Einfluss dieser Erwärmung auf die Leistungsfahigkeit eines kryo-gekühlten Monochromators abzuschätzen. Weiter wurde eine Software zur Wellenfrontsimulation wurde verwendet, um die räumlichen und zeitlichen Effekten der asymmetrischen dynamischen Diffraktion zu simulieren.

Abstract

Short duration, high spatial coherence and the high intensity of pulses generated by X-ray Free-Electron Lasers (XFELs) enable unique experimental techniques in material studies, femtosecond chemistry and others. Crystal optics are widely used at XFELs as diagnostics devices and to tailor the pulses for the experiments. The diagnostics is required due to the random nature of XFEL pulses, which leads to each pulse having individual spectral properties. Strongly bent crystals allow to disperse various photon energies over angles thus allowing to measure the spectrum. In this thesis, the effect of diffraction on the bent crystal spectrometer is studied within the frame of dynamical diffraction. It is shown that the crystal thickness limits the resolving power of the device. Due to the high intensity of the pulses, the heating caused by the absorption in the crystals leads to a significant distortion of the lattice which affects the performance of optical devices based on crystal optics. A model for the estimation of the heat load effect on the performance of a cryo-cooled monochromator is presented. A wavefront simulation software is used to simulate the spatio-temporal effects of asymmetric dynamical diffraction.

Introduction

This thesis addresses various application of crystal optics at hard X-ray Free-Electron Lasers (XFELs). The principles of X-ray generation at XFELs and an overview of XFEL facilities is presented. The second chapter presents novel studies of crystal heating and its effect on dynamical diffraction, as well as studies of the effect of asymmetric on diffraction of pulses. In monochromators, the heating hinders monochromator optimal performance, and in order to design a method to mitigate the heating effect on monochromator performance, a simulation tool for the effect of heat load on monochromator performance is desirable. A novel theoretical model of crystal heating under intense XFEL pulses and its effect on diffraction is presented and applied to experimental studies in the third chapter. The model does not require additional tools such as FEA software, it is implemented in Python and is publicly available. Such a model is transparent to the user, can be easily modified, does not require high computational power and can be used by a broad community. Also, asymmetric diffraction and its effect on spatiotemporal properties of XFEL pulses are studied in second chapter. After asymmetric diffraction, the wavefront has skewed spatial coherence, which has a potential to be beneficial for some coherent scattering experiments.

In the third chapter, studies of XFEL monochromators for hard X-rays are presented. An overview of crystal monochromators is followed by experimental studies of cryo-cooled monochromator performance. CW mode considerations are presented.

Fourth chapter addresses the effect of diffraction on the resolution of spectrometers based on strongly bent crystals. Previously, diffraction in the crystal volume was not addressed in scope of the effect on crystal resolution, and no elaborate simulations of XFEL pulses diffraction in strongly bent crystals were done. Here, a model to simulate the diffraction of XFEL pulses in strongly bent crystals is presented, which allows to estimate whether for given conditions resolution is limited due to diffraction. Moreover, it is shown that at short distances between

crystal and detector, the resolution of the device does not reach optimal values, and at a given experimental setup the distance between crystal and detector might be insufficient for optimal resolution.

Chapter 1

Properties of XFEL pulses and their application in material studies

This chapter provides an overview of the XFEL pulse generation concepts, various methods of pulse generation, and their application in material science.

1.1 Synchrotron radiation and SASE process

One of Maxwell's equations dictates that in the presence of an electric current magnetic field is produced. Namely,

$$\left[\vec{\nabla}\vec{H}\right] = \vec{j} + \frac{\partial \vec{D}}{\partial t}, \tag{1.1}$$

where $\vec{H}$ is the magnetic field, $\vec{j}$ is the current density, t is time, $\vec{D}$ is the electric displacement, and $\vec{\nabla}$ is the Hamilton operator. In particular, when an electron has acceleration, the electric charge flow in the selected volume changes, which acts as a current density in Eq. 1.1 and therefore an electromagnetic wave is generated.

When an electron bunch travels through a magnet with a constant magnetic field, the trajectory of electron beam changes and due to acceleration of the electron electromagnetic waves are emitted. Due to the changing direction of electron beam, such magnets are called "bending
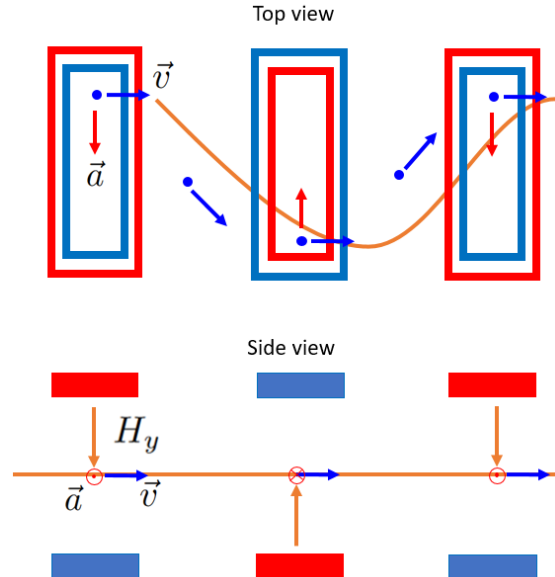
Figure 1.1: Electron oscillation in an undulator. Red and blue rectangles denote the poles of magnets, orange arrow denotes magnetic field, red arrow - electron acceleration, blue arrow - electron speed, orange curve - trajectory of an electron. The vertical magnetic field causes horizontal oscillation of electrons.

magnets". At synchrotrons, electrons travel through a set of bending magnets arranged in a circle, such that photons are generated constantly. Between bending magnets so-called "insertion devices" can be installed, which consist of a series of magnets with the changing direction of magnetic field. Depending on the magnet period and magnetic field strength, one usually differentiates inserted devices between wigglers and undulators. In undulators, where magnetic field is weaker than in wigglers, the electrons oscillate with a smaller amplitude than in wigglers, which leads to the coherent emission of electromagnetic waves by electrons.

The principle of electromagnetic emission in periodic magnets is shown in Fig. 1.1. In such devices, the electron bunch propagates between a series of magnets whose polarization changes between two opposite orientations at regular distances. This results in the electrons travelling along a sinusoidal trajectory, which means that the electrons constantly have an acceleration along the same direction. This persistent acceleration leads to the constantly emitted electromagnetic waves in the same direction.

In case of short electron bunches of high energies and strong magnetic fields of undulators, electromagnetic waves emitted by electrons affect the electrons themselves. This self-action leads to increased coherence, such that the devices are called Free-Electron Lasers (FELs), since lasers provide pulses with high coherence. At X-ray Free-Electron Lasers (XFELs), the speed of
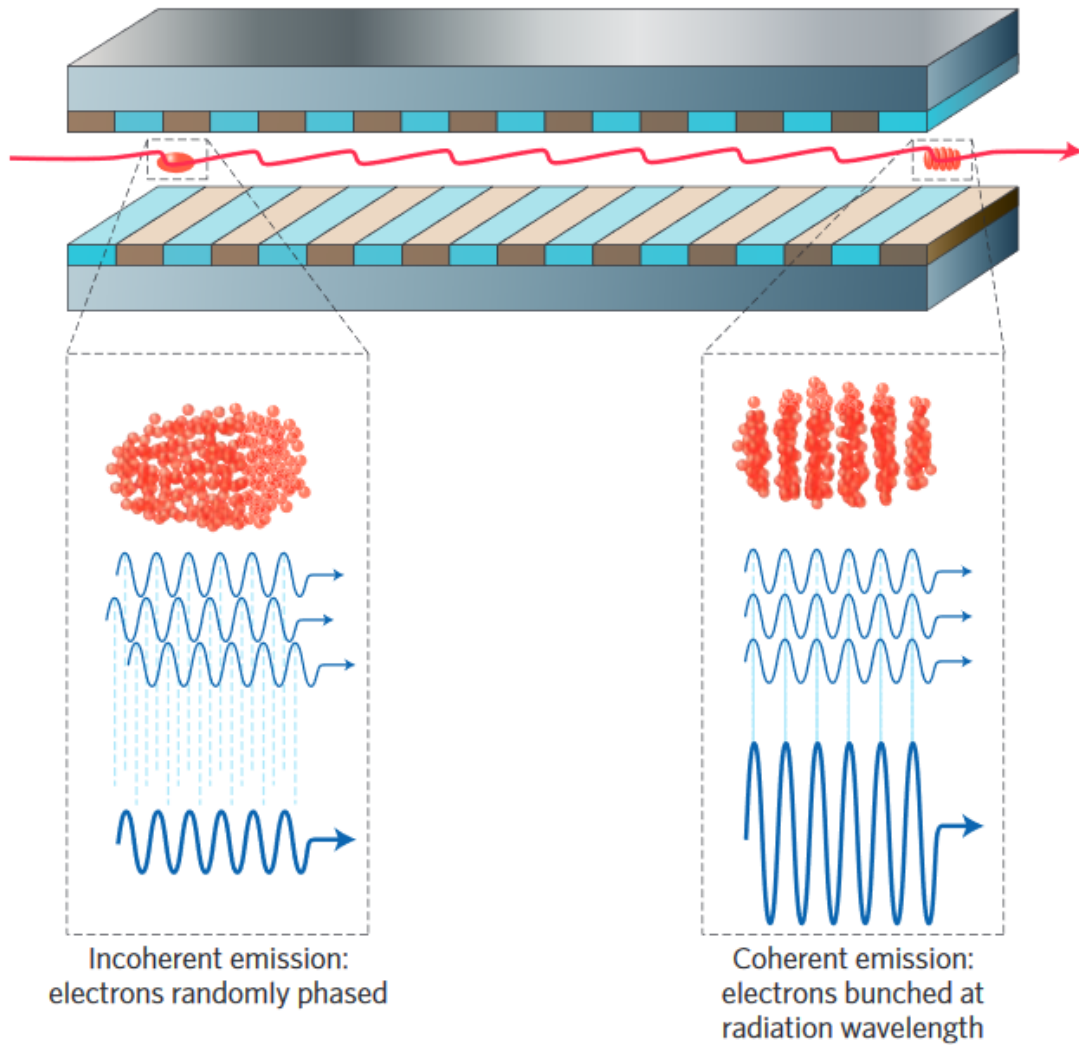
Figure 1.2: Principle of SASE pulses generation [1]. During propagation through undulator the electrons regroup into slices which produce transversely coherent X-rays.

electrons, the longitudinal size of the electron bunch and the length of undulators lead to the redistribution of electrons in a bunch into thin layers, which is called "microbunching". Due to a growing self-effect of the radiation produced by electrons, electrons group into layers during propagation through undulator. Fig. 1.2 shows how the electrons interact with the waves created by other electrons. The interaction makes the electrons group into bunches located at regular distances defined by the electromagnetic field of undulators, undulator steps and electrons mean speed.

Let us demonstrate the physical principle behind the self-amplification of FEL radiation in

Figure 1.3: Principle of coherent self-amplification, top view at undulators. Red and blue rectangles denote north and south poles of undulator cells, green wave denotes a fraction of a wave generated by electrons, blue dot is an electron, the orange line is the electric field, blue arrow is the electron speed along undualtor, green arrow - the speed of light. Electromagnetic waves are generated at wavelength for which over one undulator period the electromagnetic wave overtakes the electrons by the wavelength.

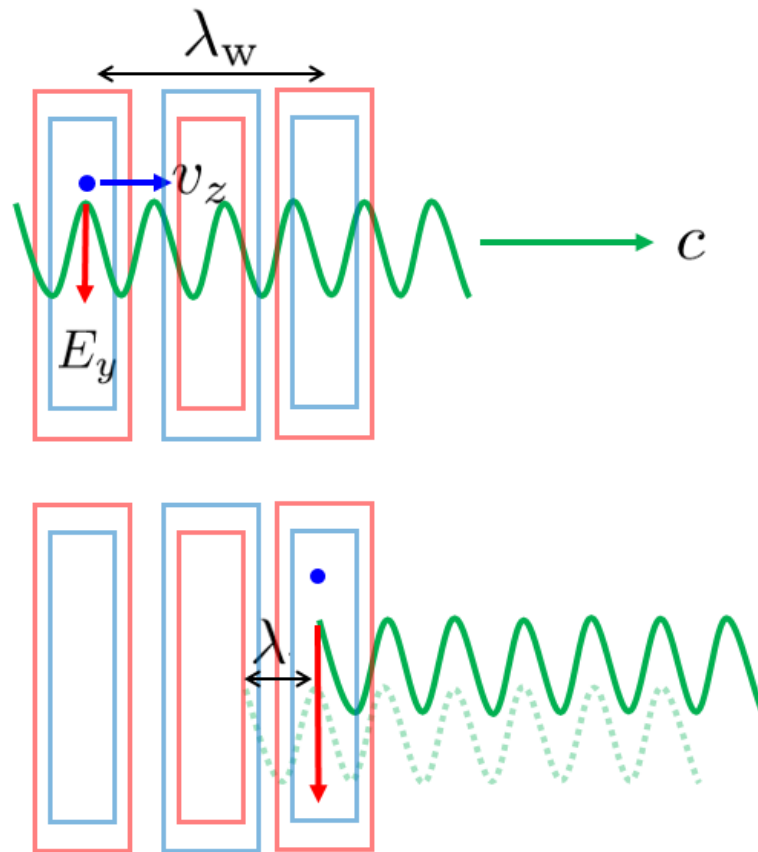undulator. If electrons travel in an undulator with a period λ_{w} and the generated X-rays have a wavelength λ, the self-amplification will take place if electron reaches each undulator cell together, or in phase, with the peak of the wave. This principle is demonstrated in Fig. 1.3. The electron speed along undulator v_z is close to speed of light c. In the coherent radiation mode, by the time an electron travels between two undulator cells with the same orientation of magnetic field, the electromagnetic wave generated by electrons needs to overtake the electron by the radiation wavelength. In that case, the electric field of the electromagnetic waves created by electrons and the Lorentz force on a moving electron in magnetic field are in phase. Therefore, the decreasing kinetic energy of electron is transformed into electromagnetic radiation. These electromagnetic waves, in turn, are in phase with the magnetic field of the undulator and contribute to the

coherent radiation. Moreover, since the initial spatial distribution of electrons is random, the
coherent radiation principle leads to regrouping of electrons into slices, as shown in Fig. 1.2. Since
the radiation produced by an electron bunch with an intrinsically random distribution affects
the bunch itself, such process of light generation is called Self-Amplified Spontaneous Emission
(SASE).

The following equation defines the condition of XFEL resonant amplification [2]:

$$\frac{\lambda_{\mathrm{w}}}{v_z} = \frac{\lambda}{c - v_z} \tag{1.2}$$

That is, the coherent radiation wavelength is defined by the undulator period and the electron
speed along undulator:

$$\lambda = \frac{\lambda_{\mathrm{w}}}{2\gamma_z^2}, \tag{1.3}$$

where $\gamma_z = 1/\sqrt{1 - v_z^2/c^2}$. During propagation through undulator, the intensity of X-ray pulse
increases exponentially. Moreover, due to the interaction with electromagnetic waves, electrons
are arranged into slices which satisfy Eq. 1.2. During further propagation through undulator,
the X-ray pulse intensity growth slows down, reaching saturation at some stage. This happens
due to decrease of electron energy and diffraction effects.

Fig. 1.4 shows a gain curve of EuXFEL, which shows how the intensity of a pulse changes
during the propagation of electron bunch through undulator. Initially, the intensity of the pulse
grows exponentially, such that the intensity curve in logarithmic scale is linear. Further down
the undulator, the growth rate decreases and the intensity of pulses reaches a saturation value.

At European XFEL (EuXFEL), electron bunch is generated by an UV-Laser incident on
Cs_2Te photocathode [4], which are next accelerated to energies of around 100 MeV, and various
diagnostics are done. The electrons are accelerated in superconducting Radio-Frequency (RF)
Niobium cavities. The electric field is oriented along the cavities' axis and oscillates at a frequency
which allows the electrons to enter each cavity with the same phase thus constantly accelerating.
There are several accelerator modules so to allow for bunch compression during acceleration. Due
to Coulomb repulsion of electrons, the compression is required to keep the bunch compact so to
provide a short duration of the photon pulses generated in undulators. Undulators at EuXFEL
consist of 35 undulator modules each 5 m long [3], and the undulator configuration allows to
generate X-ray pulses with photon energies of up to 24 keV.
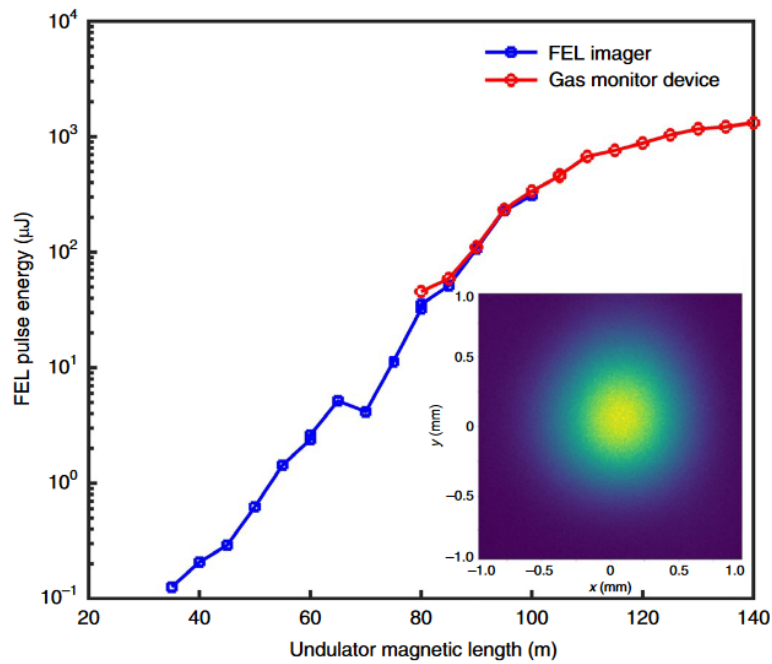
Figure 1.4: Gain curve of EuXFEL [3]. The inset shows a single pulse image at 100 m magnetic length.
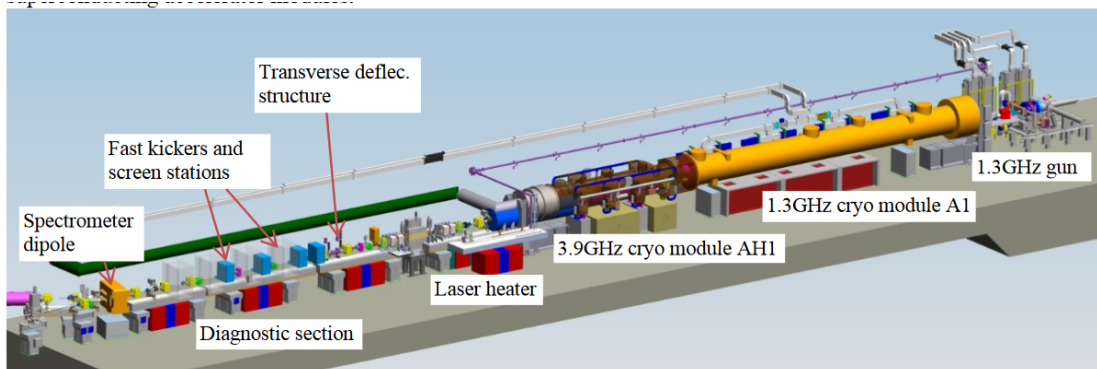
Figure 1.5: The schematics of the injector module at EuXFEL [4].

1.2 Overview of XFEL facilities

The first XFEL to operate was Linac Coherent Light Source [5]. There, the electron energy amounts up to 15 GeV and undulator length is 132 m. The repetition rate of 120 Hz is limited by the copper accelerator which cannot withstand higher repetition rates. The energy of individual pulses reached 2.5 mJ. Later, entry into operation was reported from SPring-8 Angstrom Compact free-electron LAser (SACLA) facility [6], where pulse energy reached several hundreds of µJ, while repetition rate is 60 Hz at maximum. Start of operation of another facility Pohang

Accelerator Laboratory XFEL (PAL-XFEL) with performance similar to SACLA was reported later. Here, pulse energy amounted to 130 µJ, and repetition rate of 30 Hz was demonstrated.

Short time intervals between X-ray pulses benefit experiments in various ways. Firstly, the more X-ray flux reaching a sample, the faster sufficient data can be measured, which reduces the required beamtime. Secondly, the interval between pulses defines the timescale of the effects that can be studied. LCLS-II and SHINE facilities foresee repetition rates up to 1 MHz [7, 8]. At both facilities, the pulses are designed to be generated in so-called continuous wave mode, when pulses arrive constantly.

The main reason for the limited repetition rate is the heating of the RF cavities used to accelerate electrons. At European XFEL, a 1.7 km long superconducting accelerator provides electrons that have up to 17.5 GeV energy. Despite the cryogenic cooling that enables superconductivity, the heating of the accelerator limits the number of pulses by 2700 each 0.1 s. That is, every 0.1 s a train of up to 2700 pulses is generated. Inside a train, the pulses arrive at repetition rates up to 4.5 MHz. This enables time-resolved studies on the timescales down to sub-µs level without additional optical devices.

Because of the CW mode foreseen at LCLS-II and SHINE project, the average brilliance at these XFELs is expected to surpass the one of EuXFEL by about an order of magnitude, as shown in Fig. 1.6 [9].

1.3 Self-seeding and XFEL oscillator

The distribution of electrons in a bunch into layers leads to the pulses generated by SASE process having ~ 0.2 fs coherence time, which is the duration of temporally coherent fractions of a pulse [2]. One way to generate pulses with higher temporal coherence is to combine a low-intensity pulse that has a high temporal coherence (seed pulse) and an electron bunch in an XFEL undulator. The electromagnetic field of the seed pulse modifies the electron bunch in such a way that the X-ray pulse generated during propagation through undulator has similar temporal coherence properties as the seed pulse.

One of the techniques [11] suggests dividing the undulator into two sections and inserting thin diamond crystals into the gap. The first section generates a low-intensity X-ray pulse. Due to the small thickness of the crystal and a broad $\sim$10 eV bandwidth of the pulse, most of the X-ray intensity is transmitted. However, X-rays within a narrow $\sim$0.1 eV photon energy range undergo
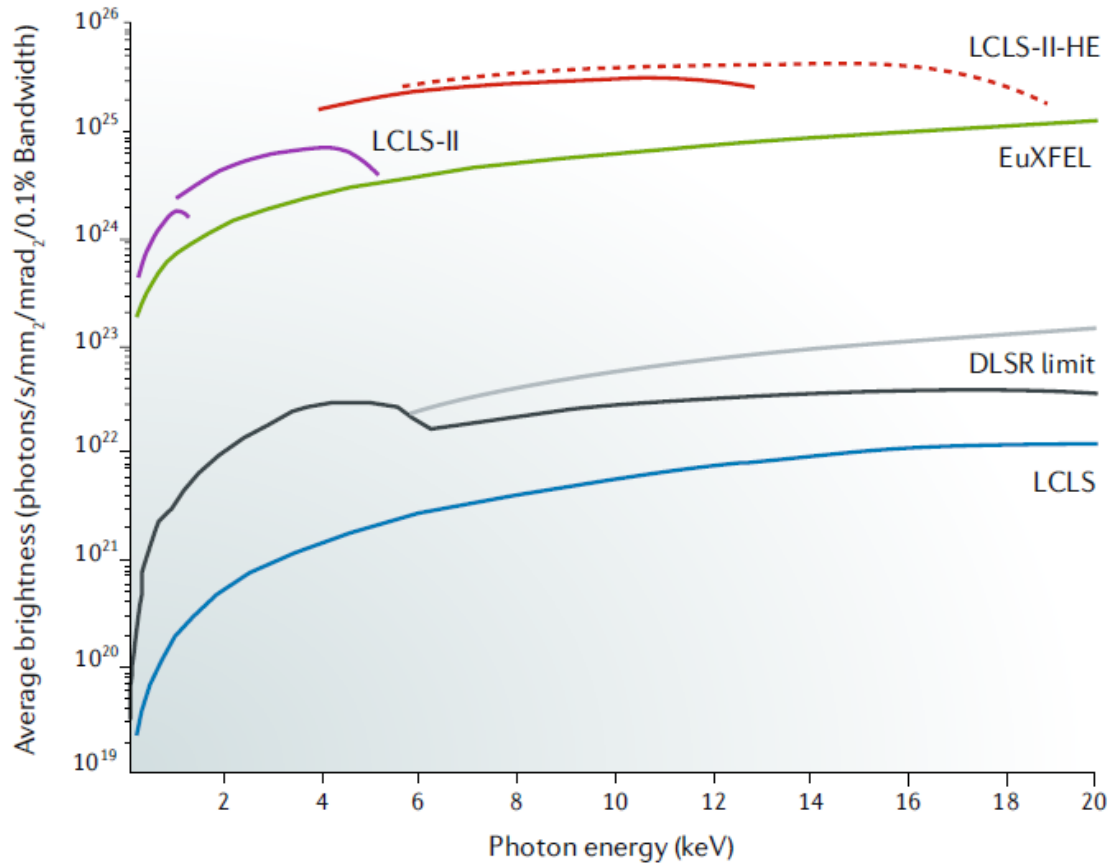
Figure 1.6: Average brightness at various photon sources [9].
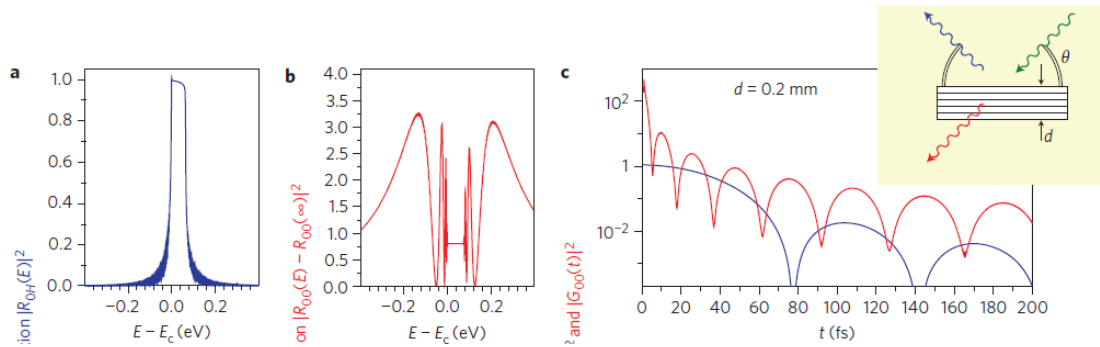
Figure 1.7: The principle of the formation of delayed coherent pulse [10]. a) shows the spectrum of diffracted pulse, b) - of the transmitted pulse. A part of the X-rays that undergo diffraction within the narrow bandwidth in a) exit the crystal in the transmission direction. c) shows the temporal structure of the transmitted (red line) and reflected (blue line) radiation. The electrons bunch is overlapped with the first most intense delayed pulse. The inset shows the geometry of the diffracted and transmitted directions. The photon energy is 8.33 keV, C(400) reflection.

dynamical diffraction, which provides a delayed pulse that travels in the same direction as the intense transmitted pulse. At the same time, the electrons travel through a bypass around the

crystal such that the electron bunch and the delayed pulse with a high temporal coherence are recombined to overlap and travel through the second part of the undulator. Since this technique applies to hard X-rays, it is called Hard X-rays Self-Seeding (HXRSS).
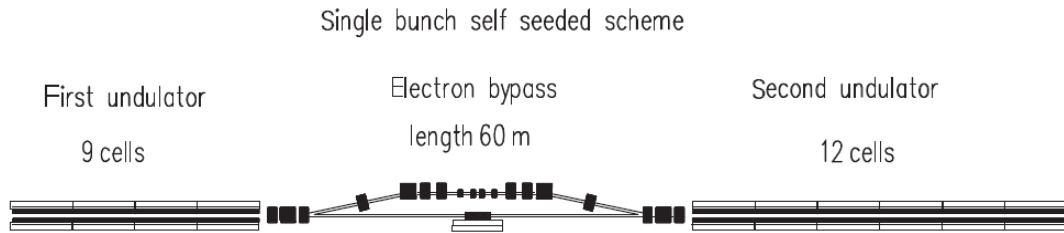
Figure 1.8: The schematics of HXRSS [11].

Such method has been realized at LCLS [10]. The bandwidth of 0.4 eV was demonstrated, though the pulse energy had large fluctuations and had the average value of 0.053 mJ. At European XFEL, HXRSS has been demonstrated at 9 and 12.9 keV photon energies using C(220) reflection. The bandwidth of the HXRSS signal was around 1 eV, and the energy of pulses reached values of around 1 mJ. At the Materials Imaging and Dynamics (MID) instrument of European XFEL, the HXRSS mode is available to users.
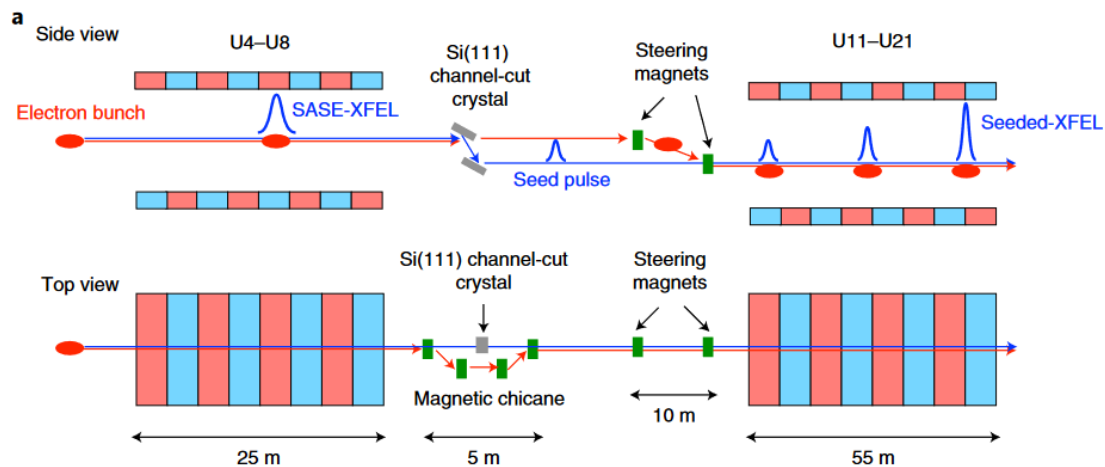
Figure 1.9: The schematics of self-seeding at SACLA using two reflections from silicon crystals [12].

At SACLA, due to relatively low pulse energies, it is feasible to use two consecutive reflections from silicon crystals to generate a monochromatic seed pulse [12]. The schematics is shown in Fig. 1.9.
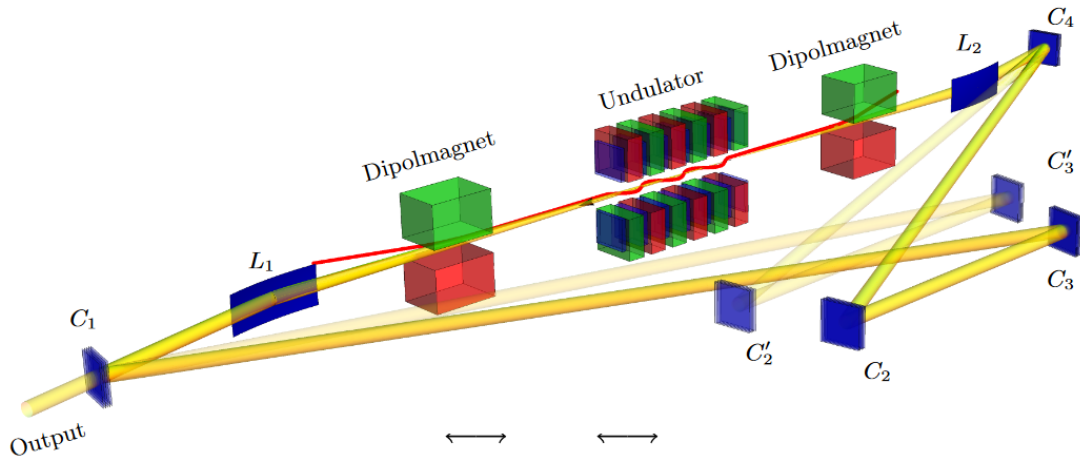
Figure 1.10: The schematics of the XFELO using 4 Bragg reflections [13].

Another way of generating XFEL pulses with even higher temporal coherence implements high order reflections in backscattering geometry from multiple crystals [14]. In this case, the reflectivity curve is narrower compared to lower order reflections. For instance, C(440) reflection has a width as low as 30 meV for 1.03 Å wavelength [13]. That way, due to a low photon energy bandwidth of the seed pulse, the generated pulse has a high temporal coherence. Moreover, by using multiple reflections, one can redirect the generated temporally coherent pulse into the undulator, recombine it with the fresh electron bunch and repeat the generation process thus gradually increasing the generated intensity.

Fig. 1.10 shows the scheme of such method. Initially, a low-energy SASE pulse is generated in the undulator, when there is no seed pulse. Then, the pulse is reflected by the crystals C_1, C_3, C_2 and C_4 that are aligned such that they are in diffraction positions. By varying the position of crystals C_2 and C_3 and orientation of all crystals, one can adjust the scheme within a wide range of photon energies. The focusing elements $L_{1,2}$ are used to direct the reflected pulse into the undulator, where the seed pulse after four crystals is coupled with a fresh electron bunch, and X-rays with a narrow bandwidth are generated. That way, each cycle increases the intensity of the pulse and the temporal coherence is conserved because of reflection from crystals at each cycle. Having reached a certain saturation energy, however, the signal does not increase since the intense pulse causes overmodulation of the existing wavefield [15] and thus hinders the coherent emission by the fresh electron bunch. The output of the scheme is defined by the transmission of C_1 crystal and the accumulated saturation power of the XFEL oscillator.

1.4   Material studies with XFEL pulses

The unique properties of the pulses generated at X-ray Free-Electron Lasers (XFELs) enable
novel experimental methods. In particular, high intensity, femtosecond duration and full spatial
coherence enable scattering experiments for material studies such as X-ray Photon Correlation
Spectroscopy (XPCS) at the molecular level [16–18]. Moreover, the short duration of the pulses
enables studying chemical reactions at the temporal scale of femtoseconds [19, 20]. The high
intensity of the pulses enables sufficient signal at crystallographic studies of protein crystals
and single-particle imaging of biological molecules [21]. The sub-µs separation between pulses
achieved at European XFEL [3] allows time-resolved studies at MHz repetition rate.

Despite their high transverse coherence, XFEL pulses generated by Self-Amplified Sponta-
neous Emission (SASE) [2] have a low temporal coherence. Along with the methods to increase
temporal coherence of the pulses exiting undulator [11, 22] discussed above, crystal optics can
be used to increase temporal coherence of SASE pulses. In particular, two parallel crystals cut
out a narrow part of a spectrum [23] thus increasing the temporal coherence. The increased
temporal coherence leads to a larger coherence volume, which increases contrast at coherent
scattering experiments with XFELs. Therefore it is crucial at experiments to maintain the sta-
ble and effective monochromatisation of pulses. However, the highly intense pulses arriving at
MHz repetition rate heat up the crystal to an extent that the lattice is distorted so significantly
that the diffraction of the pulse in the crystal is affected. In this thesis, a theoretical model for
the heat flow in the crystal and the diffraction is presented, which provides a tool to estimate
the monochromator performance for various pulse energies, pulse sizes and temporal separations
between pulses. The simulated monochromator transmission is in a good agreement with the
experiment [24]. The simple simulation model can assist researchers in modelling the heat load
effects on crystal optics, which can improve the design of existing and potential optical devices.

The random nature of the SASE process results in pulses having random temporal structure.
This, in turn, leads to the random spectrum of each pulse. The spectrum can help estimate the
temporal properties of the pulse which is crucial for some scattering experiments. For instance,
information about the pulse duration provides the limit on the timescale of the observed physical
effect. Strongly bent crystals are capable of effectively dispersing the X-rays of different photon
energies over different angles due to the curved surface. This thesis addresses the problem of
XFEL pulse diffraction in bent crystals in the frame of the kinematical and dynamical theory
of X-ray diffraction. The approach described in this thesis can be used to evaluate the validity

13

of the measured spectra and simulate the resolving properties of spectrometers based on bent

crystals. A novel method to estimate the pulse duration is proposed which allows to restore the

temporal properties from spectra of individual pulses.

Chapter 2

Diffraction of hard X-rays in perfect crystals and wavefront propagation through optical elements

2.1 Kinematical diffraction of X-rays

In the framework of kinematical diffraction [25], the resulting amplitude in a point with radius-vector $\vec{\rho}$ is defined by the integral

$$E_s \propto \int\limits_{\rho_0} \frac{\exp(ik|\vec{\rho} - \vec{\rho_0}|)}{|\vec{\rho} - \vec{\rho_0}|} d^3\rho_0, \tag{2.1}$$

which represents the sum of waves scattered by each point of a scattering object with radius-vectors $\vec{\rho_0}$, $k = 2\pi/\lambda$, λ is the wavelength. That is, the interaction of X-rays with crystals is considered as a singular scattering from the atoms, without secondary scattering. Eq. 2.1 is written under assumption of an incident plane wave, which is the simplest approach to treating diffraction. A particular temporal structure can be decomposed into a set of plane waves, and a particular spatial distribution of radiation will lead to the dependence of incident wave amplitude on $\vec{\rho}$. In case of a crystal lattice where the atoms are positioned in a regular manner, only the

15

intensity of diffracted wave will be significant at certain directions defined by the constructive
interference of waves scattered from atoms. The Bragg law

$$2d \sin \theta_B = \lambda \tag{2.2}$$

represents the condition for the coherent addition of waves scattered by a lattice and defines the
Bragg angle θ_B at which the strongest scattering is observed for the given lattice spacing d.

In a thick perfect crystal, the secondary scattering of X-rays will have a significant effect
on the resulting diffraction amplitude. This re-scattering in ideal crystals is described by the
theory of dynamical diffraction of X-rays [26, 27]. X-rays that are scattered by a given atom are
strongly scattered by other atoms before leaving the crystal.
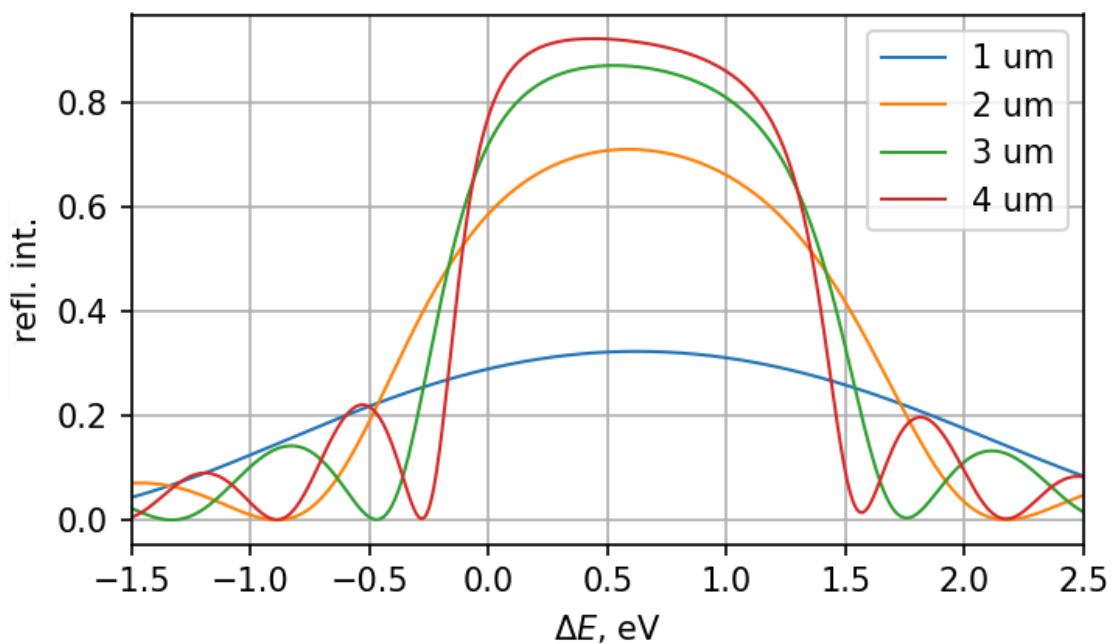
Figure 2.1: The effect of the crystal thickness on the rocking curve at 9 keV photon energy.
Crystal is Si(111), at the given photon energy extinction length is 1.5 µm. When crystal thickness
is larger than extinction length, the re-scattering of X-rays affects becomes strong. The curves
are calculated using dynamical diffraction [26, 27].

Fig. 2.1 shows how an increasing thickness of a crystal affects the diffraction at different
photon energies, calculations are done using dynamical diffraction theory presented below. In
a thin crystal, the rocking curve (blue line) is wide since no secondary scattering takes place.
With an increasing thickness, the rocking curve gets narrower and the oscillations on the edges

that are characteristic of diffraction appear. The multiple re-scattering of X-rays from atoms happens predominantly around the angle at which Eq. 2.2 is satisfied. For a thicker crystal, the rocking curve gets narrower and the oscillating features at the edges also get narrower.

2.2 Dynamical diffraction

Let us assume that the Bragg condition is fulfilled for a photon energy $E_0 = hc/\lambda$ in the case of a non-deformed crystal lattice, where h is the Planck constant and c is the speed of light. The diffraction of X-rays with a photon energy E at an instant t and at the position r is defined by the deviation of the wave vector from the exact Bragg condition [28, 29]
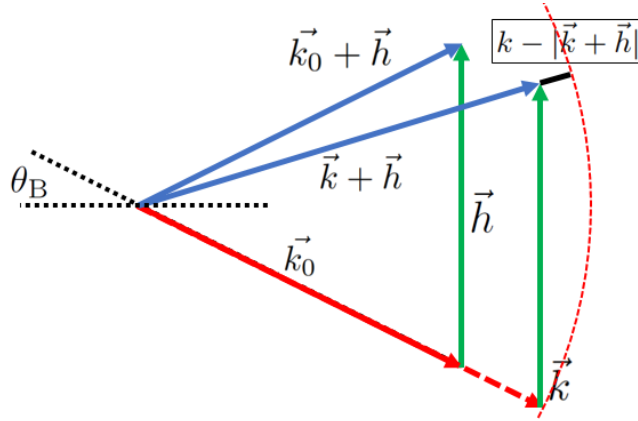
Figure 2.2: The geometry of vectors in Eq. 2.3.

$$\eta(E, t, r) = \frac{k^2 - (\vec{k} + \vec{h})^2}{k^2},$$
(2.3)

where $\vec{k}$ is the wavevector for the incident wave and $\vec{h}$ is the reciprocal lattice vector. Fig. 2.2 depicts the calculation of Eq. 2.3. The deviation η is defined by the difference of squares of lengths of incident wavevector $\vec{k}$ and $\vec{k} + \vec{h}$. For wavevector $\vec{k_0}$, which corresponds to central photon energy E_0 and incidence at Bragg condition, $\eta = 0$, since the length of $\vec{k_0} + \vec{h}$ is the same as the length of $\vec{k_0}$. When incident wavevector $\vec{k}$ is different from $\vec{k_0}$, either in length and/or direction, $\vec{k}$ and $\vec{k} + \vec{h}$ have different lengths.

We assume that all photon energies are incident at the same angle θ_B. Fig. 2.3 shows the geometry of vectors in this case. Following the geometry, Eq. (2.3) can be calculated as
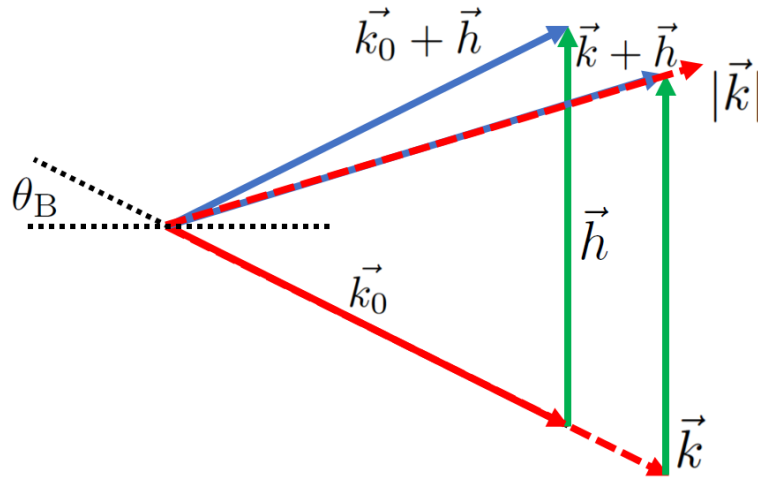
Figure 2.3: The geometry of vectors for Eq. 2.5.

$$\eta\left(E, t, r\right) = 2\sin 2\theta_{\mathrm{B}} \left(\frac{\Delta E}{E_0}\right)\tan\theta_{\mathrm{B}}, \tag{2.4}$$

where $\Delta E = E - E_0$. In a more general case of variable $\vec{h}$, i.e. in case of deformed crystal, 2.3 can be written as

$$\eta\left(E, t, r\right) = 2\sin 2\theta_{\mathrm{B}} \left(\frac{\Delta E}{E_0} + \epsilon\right)\tan\theta_{\mathrm{B}}, \tag{2.5}$$

where $\epsilon = \Delta d/d$ is the relative deformation of the lattice which is elaborated on in the next section, d is the lattice spacing of the non-deformed crystal.

Let us derive dynamical diffraction equations. The following two Maxwell equations in the absence of current and in a diamagnetic medium

$$\begin{aligned}
\nabla \times \mathbf{E} &= -\frac{1}{c}\frac{\partial \mathbf{H}}{\partial t} \\
\nabla \times \mathbf{H} &= -\frac{1}{c}\frac{\partial \mathbf{D}}{\partial t}
\end{aligned} \tag{2.6}$$

would describe propagation of electromagnetic wave. Here, $\mathbf{D}$, $\mathbf{E}$ and $\mathbf{H}$ are the vectors of the electric displacement, electric field and magnetic field, c is the speed of light, t is time. Vector multiplication of both equations by ∇, since $\nabla \times \nabla \times \mathbf{E} = \mathrm{grad}\,\mathrm{div}\mathbf{E} - \Delta\mathbf{E}$, would yield

$$\Delta \mathbf{E} + \frac{1}{c^2}\frac{\partial^2 \mathbf{D}}{\partial t^2} = 0. \tag{2.7}$$

Let us find the solution

$$\mathbf{E} = \exp(i\omega t)[A_0 \exp(i\vec{k_0}\vec{r}) + A_h \exp(i\vec{k_h}\vec{r})] \tag{2.8}$$

at any point of space $\vec{r}$ and two constant amplitudes $A_{0,h}$, $\vec{k_0}$ is the wave vector of incident wave and $\vec{h}$ is reciprocal lattice vector, $\vec{k_h} = \vec{k_0} + \vec{h}$, t is time and ω is the frequency. In a crystal with reciprocal lattice vector $\vec{h}$ electric susceptibility can be written as

$$\chi(\vec{r}) = 1 + \chi_0 + \chi_h \exp(i\vec{h}\vec{r}) + \chi_h \exp(-i\vec{h}\vec{r}). \tag{2.9}$$

At XFELs, bandwidth of photon energies is small enough to consider χ_h to be constant in the current model. That way, since $\mathbf{D}(\vec{r}) = (1 + \chi(\vec{r}))\mathbf{E}(\vec{r})$ Eq. 2.7 can be written as

$$k_0^2 A_0 \exp(i\vec{k_0}\vec{r}) + k_h^2 A_h \exp(i\vec{k_h}\vec{r}) - \frac{\omega^2}{c^2}\chi(\vec{r})(A_0 \exp(i\vec{k_0}\vec{r}) + A_h \exp(i\vec{k_h}\vec{r})) = 0, \tag{2.10}$$

which would give the following set of dynamical diffraction equations:

$$-\frac{\omega^2}{c^2}\chi_h A_h + (k_0^2 - \frac{\omega^2}{c^2}(1 + \chi_0))A_0 = 0$$
$$(k_h^2 - \frac{\omega^2}{c^2}(1 + \chi_0))A_h - \frac{\omega^2}{c^2}\chi_h A_0 = 0. \tag{2.11}$$

These linear equations can be solved only if the determinant of Eq. 2.11 is zero, i.e.

$$(k_h^2 - \frac{\omega^2}{c^2}(1 + \chi_0)) = \chi_h^2/(k_0^2 - \frac{\omega^2}{c^2}(1 + \chi_0)), \tag{2.12}$$

which yields the following reflection amplitude:

$$R = \frac{A_h}{A_0} = \frac{k_0^2 - \frac{\omega^2}{c^2}(1 + \chi_0)}{\frac{\omega^2}{c^2}\chi_h}. \tag{2.13}$$

Using Eq. 2.3, we can rewrite Eq. 2.12 as

$$((1 + \eta)k_0^2 - \frac{\omega^2}{c^2}(1 + \chi_0)) = \chi_h^2/(k_0^2 - \frac{\omega^2}{c^2}(1 + \chi_0)), \qquad (2.14)$$

or, using R from Eq. 2.13, we can write the following dispersion equation:

$$\chi_h R^2 - \eta R + \chi_h = 0, \qquad (2.15)$$

which yields the solution

$$R(E, t, r) = \frac{\eta(E, t, r) \pm \sqrt{\eta(E, t, r)^2 - 4\chi_h^2}}{2\chi_h}, |R| < 1, \qquad (2.16)$$

which is dictated by the physical restriction of the reflection amplitude less than unity.
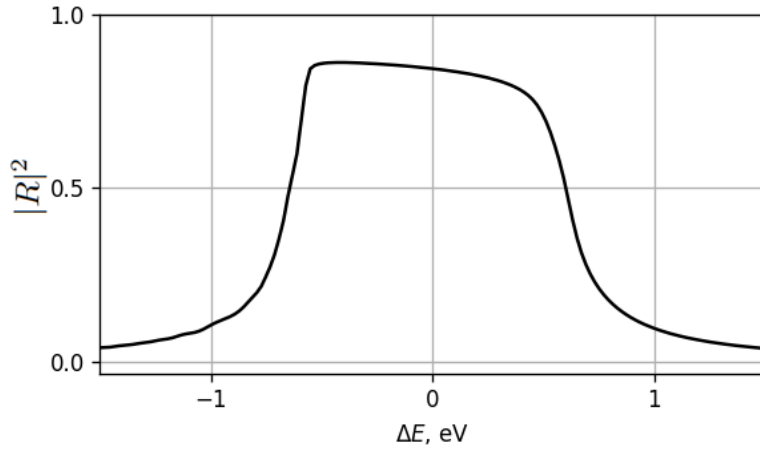
Figure 2.4: Reflection intensity $|R|^2$ calculated by Eq. 2.16 for non-deformed Si(111) crystal at 9 keV photon energy for infinitely thick crystal, $\Delta E = E - E_0$.

Fig. 2.4 shows the reflection intensity for various photon energies, which is often referred to as Darwin curve. The width of the curve, or Darwin curve, can be determined from Eq. 2.16, when the term under the square root is 0. Therefore, for non-deformed crystal, from Eq. 2.5 we can calculate the width of rocking curve:

$$\Delta E^{\text{width}} = 2|\chi_h|/\sin\theta_B. \qquad (2.17)$$

In practice, within the width in Eq. 2.17 the intensity of X-rays decays exponentially with depth due to a growing fraction of diffracted intensity. The thickness at which the intensity decays by a factor of e is called extinction length $l_{\text{ex}} = \sin\theta_B\lambda/\pi\chi_h$[27]. For silicon $l_{\text{ex}}^{\text{Si}} = 1.5$ µm at 9 keV,

such that the limit of an infinite crystal in Eq. 2.16 is reached at a thickness of a few µm.

2.3 Evolution of crystal temperature under pulsed heat load and its effect on the X-ray diffraction in monochromators

At European XFEL, strong heat load on X-ray optics and crystals in particular was foreseen during the conceptual design of the facility [30] and remains an important topic. Simulation of pulses absorption in crystal, heat flow and diffraction is required for the design of crystal optics. Monochromators are widely used at XFELs, and their thermal stability under intense pulses needs to be studied. One of the straightforward ways to simulate the heating and deformation of crystals under XFEL pulses is to use Finite-Element Analysis (FEA) software, such as COMSOL or ANSYS. FEA has been used in combination with a simple diffraction model [28, 29] for simulation of crystal optics performance under intense XFEL pulses. However, since FEA packages are commercial products, their source code is unavailable. That way, one cannot verify all steps of the calculations, which might lead to failures in the design of optical devices. Moreover, the complexity of FEA software requires an expertise in order to do simulations, and simulations are time-consuming. Here, a transparent one-dimensional heat flow model is introduced, whose implementation in Python is available to the public [31]. A theoretical justification of the model applicability under the given conditions is presented, and the simulation results are compared to experimental data. The code also contains a diffraction module, which allows to simulate the diffraction of X-rays in a deformed crystal. The code is designed specifically for silicon monochromators under high-repetition XFEL radiation and can be used by a broad community.

For the simulation of heat absorption and transfer, the crystal is divided into n cylindrical shells with inner radii of $r_i = (i - 1) \cdot dr$. i varies from 1 to n and the outer radii of the ith shell is $r_i + dr$ where dr is the thickness of each cylindrical shell [32]. Along the surface normal direction cylinders are divided into m layers of dz thickness and the position of the jth layer in the depth coordinate is $z_j = j \cdot dz$, where j varies from 1 to m.

Let us consider a Gaussian pulse whose depth-radial intensity profile reads

$$I(r_i, z_j) = I_0 S(r_i) \frac{\exp(-r_i^2/2\sigma^2)\exp(-z_j/a)}{2\pi\sigma^2 a} dz, \tag{2.18}$$
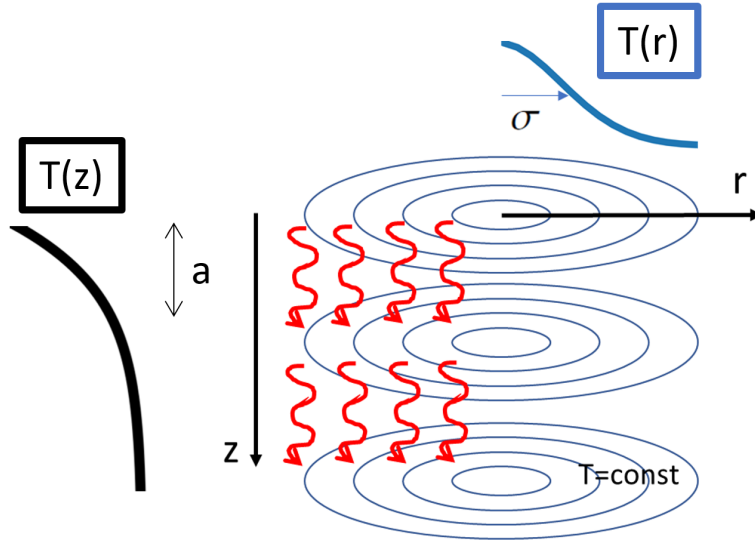
Figure 2.5: The schematics of the heat flow simulation model. Black and blue curve denote the exponential profile of heat deposition along depth and Gaussian profile along surface, red wave arrows denote the heat flow calculations using Eq.2.22. The temperature of the bottom layer is constant as per boundary conditions in Eq.2.23.

where I_0 is the total pulse energy, $S(r_{i>1}) = 2\pi r_i dr$, $S(r_1) = \pi \cdot dr^2$, $\sigma = w_{\mathrm{equiv}}/2\sqrt{2\ln 2}$ where w_{equiv} is the full-width at half maximum (FWHM) of the beam size at the crystal surface and a is the depth at which the intensity of the beam decreases by a factor of e. Since the X-rays impinge the crystal at an angle θ_0, the pulse size $w_{\mathrm{equiv}} = w/\sqrt{\sin\theta_0}$ is used for the simulations, where w is the FWHM size of the pulse incident at an angle θ_0. By using w_{equiv}, we account for the elliptical footprint of the beam in the circularly-symmetric model, such that the average heat density is the same, such that in the cylindrical model average heat load surface is the same as for the pulse with size w incident at an angle θ_0. $a = l_{\mathrm{abs}} \sin\theta_0$, where l_{abs} is the absorption length of X-rays at a given photon energy. We consider that all of the pulse energy absorbs, such that we neglect the fact that a part of X-rays diffract and they do not contribute to the heating. This can be justified since the diffraction takes place in a narrow bandwidth and in a heated crystal X-rays are absorbed stronger since the diffracting regions of the crystal are located deeper in the crystal.

The temperature of each cylinder layer with inner radius r_i at depth z_j is defined by the heat absorbed per unit of mass. The absorption of an incident pulse and resulting heating are considered to be instantaneous in comparison with the characteristic time for the redistribution of temperature (see below for the estimations of the timescales using Eq. 2.25). The temperature
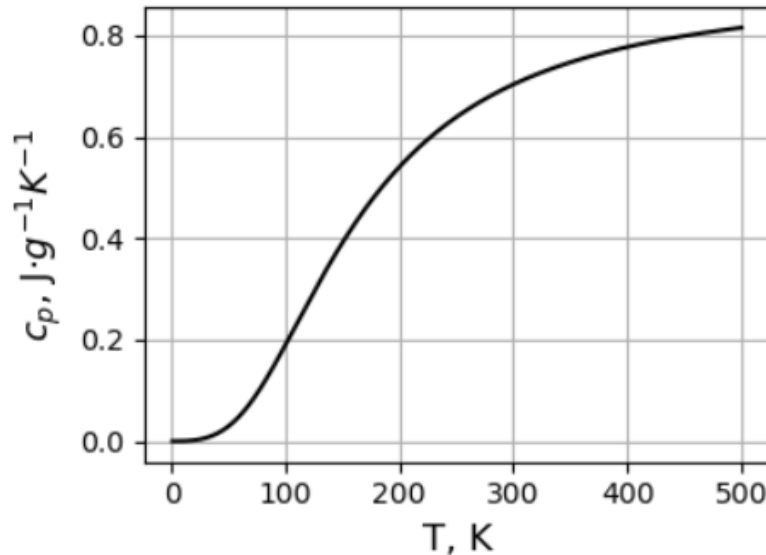
22

Figure 2.6: Theoretical specific heat of silicon calculated by Debye model.

$T_0(r, z)$ at each radius r and depth z (indices of r_i and z_j are omitted) after the absorption of a pulse is determined by the absorbed heat per unit of mass in the corresponding cylindrical shell given by

$$\int_{T_{init}}^{T_0(r,z)} c_p(T)dT = \frac{I(r, z)}{dz \cdot \rho S(r)},$$

(2.19)

where $c_p(T)$ is the temperature-dependent specific heat of silicon that has been calculated as per Debye's model[33], ρ is the density of silicon (whose temperature dependence is neglected due to small linear expansion, see Fig. 2.10) and T_{init} is the initial temperature of the crystal.

Debye's model considers that a cubic volume with a side L_d contains N molecules which comprise a solid body. The oscillations of atoms in a solid body are defined by the temperature and can be decomposed into group oscillations of atoms, i.e. phonons. Since the minimal scale of the atomic oscillation wavelength is defined by the separation between atoms, the maximum phonon number is $n_{max}^p = \sqrt[3]{N}$. Phonon energy $E^p = h^p c_s n^p / 2L$ is defined for each phonon number n^p, where h^p is the Planck constant and c_s is the speed of sound. The Bose-Einstein distribution dictates that the fraction of phonons with energy E in the three-dimensional volume $\bar{N}(E) = 3/(\exp(E/kT) - 1)$. Calculating the sum of energies of all phonons and taking a derivative over time, we get the molar specific heat

$$c_v^D = 9R \left(\frac{T_D}{T}\right)^3 \int_0^{T_D/T} \frac{x^4 e^x}{(e^x - 1)^2} dx, \tag{2.20}$$

where $R = 8.31 \text{J/g} \cdot \text{K}$ is the gas constant and T_D is the Debye temperature of a given material. Specific heat c_p can be calculated from Eq. 2.20 using

$$c_p = c_v^D / M, \tag{2.21}$$

where M is the molar mass of an element of interest. For instance, for silicon $M_{\text{Si}} = 28$ g/mol, such that according to Eq. 2.20 $c_p(T \to \infty) = 3 \cdot R/28$ g/mol $= 0.89$ J/g $\cdot$ K. Fig. 2.6 shows the specific heat of silicon calculated using Eq. 2.20 and 2.21. Since for silicon $T_D = 648$ K, one can see that the temperature reaches a limit.

The temperature evolution with time $T(t, r, z)$ is defined by the heat transfer equation which in the depth direction is written as

$$\frac{\partial T(t, r, z)}{\partial t} = D(T) \cdot \frac{\partial^2 T(t, r, z)}{\partial z^2}, \tag{2.22}$$

where $D(T) = K(T)/\rho c_p(T)$ is the temperature-dependent thermal diffusivity and $K(T)$ is the temperature-dependent thermal conductivity [34]. Let us analyze how the heat transport properties of silicon change during the heating. Below, the heating of silicon from 100 K up to 300-500 K will be studied, therefore let us analyze the thermal conductivity properties of silicon in that range of temperatures.

A linear rise of specific heat in Fig. 2.6 and a logarithmic decrease of heat conductivity in Fig. 2.7 lead to a rapid decrease of heat diffusivity in Fig. 2.8 with increasing temperature. Therefore cryogenic temperatures of 100 K and lower are preferred in terms of effective heat dissipation.

The boundary conditions for (2.22) are

$$T(0, r, z) = T_0(r, z), \ \left.\frac{\partial T}{\partial z}\right|_{z=0} = 0, T(t, r, z = z_m) = T_{\text{init}}, \tag{2.23}$$

which correspond to the absence of heat exchange at the crystal surface and a constant temperature T_{init} at depth z_m. The geometry of the calculation mesh, heating and heat flow is shown in Fig. 2.5. This is demonstrated in Sec. 3.3.

When a second pulse arrives at an instant t_1, the temperature profile $T'(t_1, r, z)$ is defined
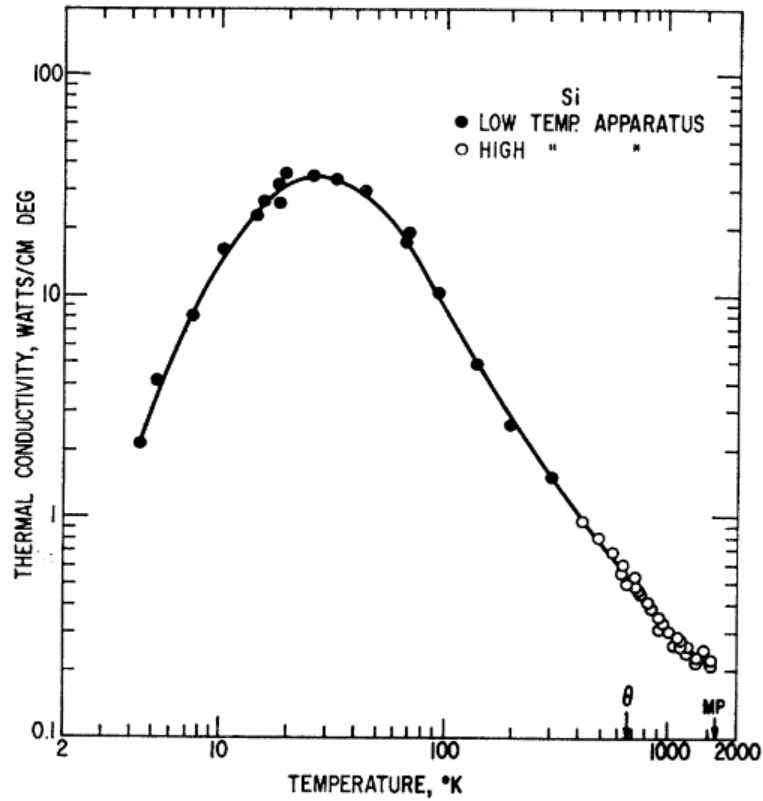
Figure 2.7: Heat conductivity $K(T)$ of silicon [34].

analogous to Eq. (2.19):

$$\int_{T(t_1,r,z)}^{T'(t_1,r,z)} c_p(T)dT = \frac{I(r,z)}{\rho \cdot dz \cdot S(r)}. \tag{2.24}$$

Let us analyze Eq. (2.22) in order to estimate the characteristic timescale of heat transfer in the radial and depth directions. The pulse and crystal parameters for the estimations would be as follows: $T_{\text{init}} = 100$ K, FWHM beam size around 500 µm, $a = 21$ µm corresponding to $l_{\text{abs}} = 97$ µm and $\theta_0 = 12.7°$, which is the Bragg angle for Si(111) reflection at 9 keV photon energy. For silicon, $D(100$ $K) \approx 28$ cm^{2}s^{-1}. Considering the heat flow equation (2.22), the characteristic time for the disappearance of temperature gradient over a distance L can be estimated as

$$t_{\text{char}}(L) \sim \frac{L^2}{D}. \tag{2.25}$$

Let us consider the estimate of the distance in Eq. (2.25) in radial direction $L_r = 1173$ µm,

25
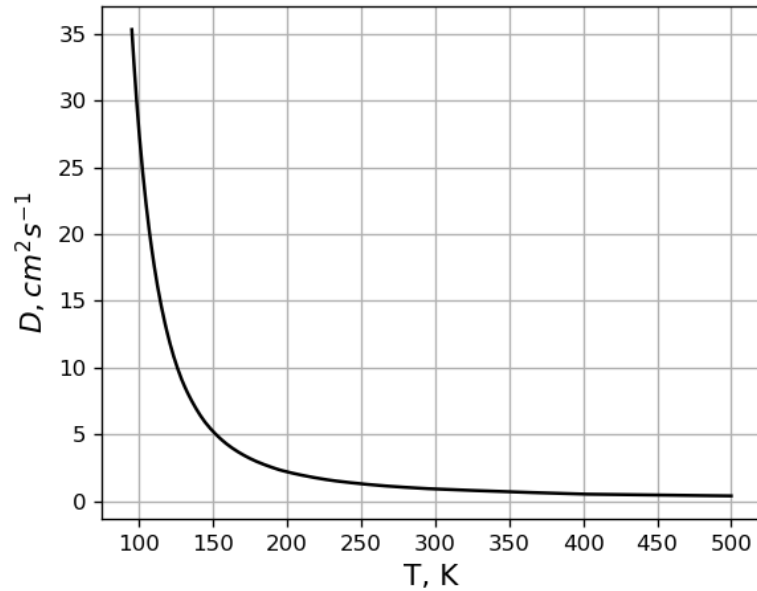
Figure 2.8: Heat diffusivity $D(T)$ of silicon calculated using heat conductivity [34], Debye model specific heat and silicon density.

which is equal to the beam footprint, and in depth direction $L_z = a = 21$ µm. For the heat redistribution in the radial direction, $t_{\text{char,r}} = t_{\text{char}}(L_r) = 498$ µs, whereas in the depth direction $t_{\text{char,z}} = t_{\text{char}}(L_z) = 160$ ns. Hence $t_{\text{char,r}} \gg t_{\text{char,z}}$.
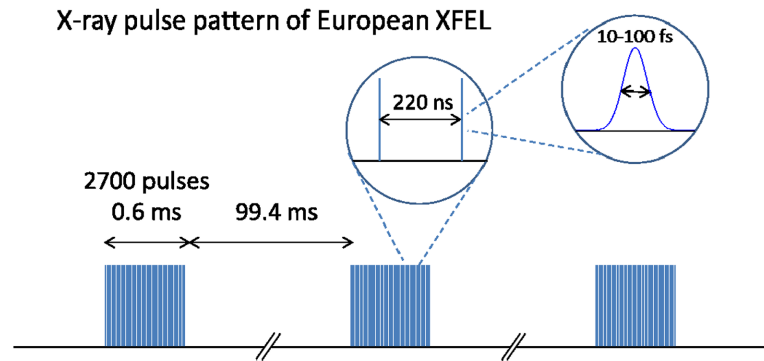
Figure 2.9: The distribution of pulses at European XFEL in time.

The structure of pulses in time is shown in Fig. 2.9. Individual pulses are delivered with a separation of at least 220 ns which arrive in so-called "trains" of several hundreds of pulses. Trains arrive with an interval of 0.1 s. The duration of pulses at European XFEL is estimated to be ~10-100 fs, which is many orders of magnitude shorter than the characteristic heat redistribution time, see Eq. (2.25). Therefore the assumption of instantaneous heating of the crystal by a pulse

is justified. Moreover, the delay time between individual pulses at European XFEL is typically between 220 and 880 ns which is about two orders of magnitude smaller than $t_{\text{char,r}}$. Thus neglecting heat flow in the radial direction is justified from one pulse to the next one inside the pulse train. However, $t_{\text{char,z}}$ is of the same the order as the time delay between pulses and therefore heat flow in the depth direction during a train must be accounted for in the simulations. On the other hand, the 0.1 s interval between pulse trains is much larger than both $t_{\text{char,r}}$ and $t_{\text{char,z}}$ and therefore, by the time the next pulse train arrives, the crystal has fully recovered to the initial temperature.

In the experiment, the crystal is 2.5 cm thick and is kept at a constant cryogenic temperature. Therefore, the last of boundary conditions in Eq. (2.23) defining a constant temperature at depth z_m is applicable.

The beam induced heating of the crystal described in the previous section causes a deformation of the lattice, which is different in each point of the crystal. Considering dynamical diffraction, only the component of the deformation normal to the crystal surface is relevant in the case of symmetrical Bragg diffraction, since this affects the lattice spacing used in Eq. (2.2). In order to estimate the effect of crystal deformation on the diffraction, we consider the heating of the crystal on the surface, i.e. at $z = 0$. The lattice deformation $\epsilon(t, r)$ in the direction normal to the crystal surface caused by heating from T_{init} to $T(t, r, z)$ is defined by the accumulated expansion and

$$\epsilon(t, r) \equiv \frac{\Delta d(t, r)}{d_{\text{init}}} = \int_{T_{\text{init}}}^{T(t, r, z=0)} \alpha_T (T) \, dT, \tag{2.26}$$

where $\alpha_T(T)$ is the temperature-dependent linear expansion coefficient of silicon which is close to zero near 100 K [35], d_{init} is the lattice spacing at temperature T_{init}, $d_{\text{init}}^{\text{Si}} = 3.1415$ Å for silicon, and $\Delta d(t, r)$ is the lattice spacing change after heating from T_{init}.

Fig. 2.10 shows the temperature dependence of silicon linear expansion. When the temperature rises from 100 K, the linear expansion crosses the zero value, which means that even when the crystal gets heated, its deformation is small and thus diffraction is not strongly affected.

We consider that Eq. (2.16) defines the reflection amplitude at each point of the crystal surface. At a given photon energy E the total reflection intensity from the crystal is defined as an integral of Eq. (2.16) over the crystal surface
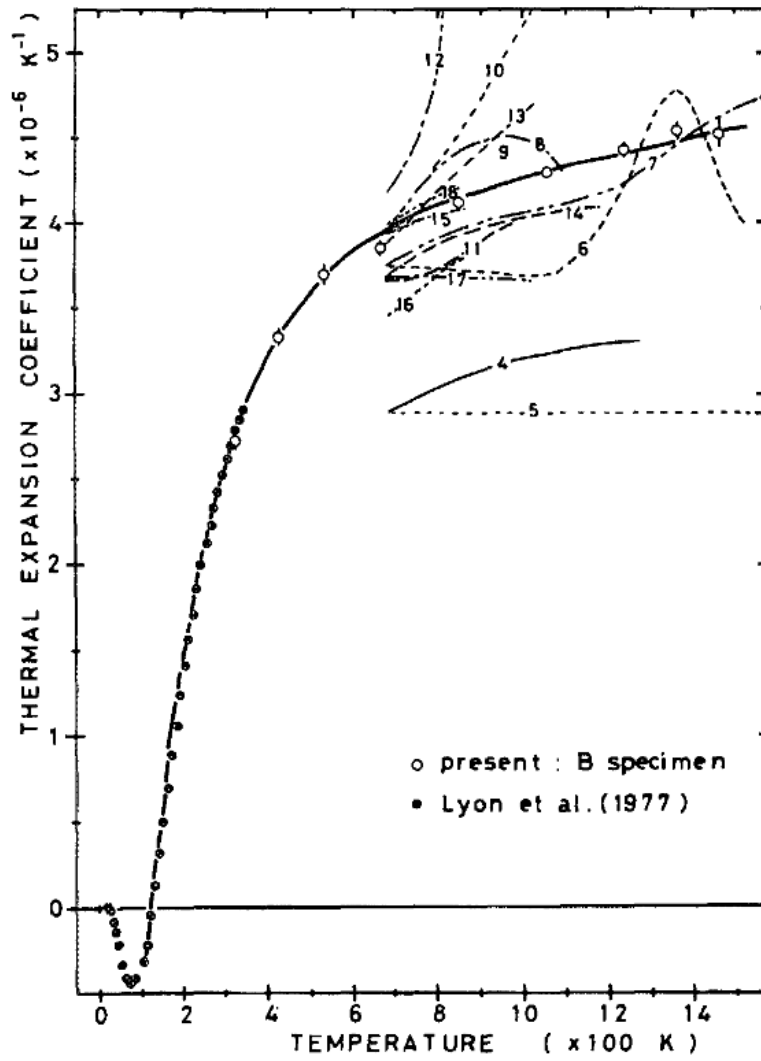
Figure 2.10: Linear expansion α_T of silicon [35]. Since linear expansion is on the order of 10^{-6}, even when heated by several hunderds of K, the volume increases by a factor of around 10^{-4}, such that the constant density is justified in the heating simulations.

$$I_E\left(E,t\right) \sim \int_0^{r_n} \left|R\left(E,t,r\right)\right|^2 \cdot \exp\left(-\frac{r^2}{2\sigma^2}\right) \frac{r}{\sigma^2} dr. \tag{2.27}$$

In Chapter 3, the studies of hard X-ray double-bounce monochromators are presented. In such devices X-ray pulses undergo two consecutive reflections from two crystals that are kept at cryogenic temperatures. The spectral width of the Bragg reflection of Si(111) at 9 keV, as shown in Fig. 2.4, is ∼1 eV, whereas the spectral width of the XFEL pulses is ∼20 eV according to the simulations of SASE pulses [36]. Therefore, since only a narrow fraction of X-rays is reflected

by the first crystal of the monochromator, we assume that the second crystal remains unheated
and thus non-deformed and oriented parallel to the first crystal. Therefore, for a given photon
energy the reflection intensity from two crystals can be calculated as

$$I_E(E,t) \sim \int_0^{r_n} |R_0(E,t,r)|^2 \cdot |R(E,t,r)|^2 \cdot \exp\left(-\frac{r^2}{2\sigma^2}\right) \frac{r}{\sigma^2} dr, \qquad (2.28)$$

where $|R_0(E,t,r)|^2$ is the reflection amplitude (2.16) for the non-deformed crystal, i.e. $\epsilon(E,t,r) \equiv 0$.

The reflectivity from two crystals $I_R(t)$ case can be calculated as an integral of the reflection
amplitude (2.28) over the photon energies as follows:

$$I_R(t) \sim \int_{\Delta E_0} I_E(E,t)dE, \qquad (2.29)$$

where ΔE_0 is the range of photon energies.

2.3.1 Python implementation of the heat deposition and propagation model

The integrals in Eqs. 2.19, 2.24 and 2.26 are calculated using interpolation.

```
T_arr = np.linspace(T_min,T_max,T_points)

cp_arr = np.interp(T_arr,cp_T,cp_raw)
heat_int = np.cumsum(cp_arr)*(T_arr[1]-T_arr[0])
heat_0 = heat_int[np.argmin(np.abs(T_arr[:]-T_init))]
T_pulse = np.interp(heat_pulse_ip,heat_int-heat_0,T_arr)

alpha_exp_arr = np.interp(T_arr,alpha_exp_T,alpha_exp_raw)
deform_int = np.cumsum(alpha_exp_arr)*(T_arr[1]-T_arr[0])
deform_init = np.interp(T_init,T_arr,deform_int)
deform_x = np.interp(T_pulse,T_arr,deform_int)-deform_init
```

Figure 2.11: The code for definition of the temperature in Eq. 2.19 and deformation in Eq. 2.26.

Fig. 2.11 shows the pieces of code which implement the integrals in Eq. 2.19 and Eq. 2.26.
T_arr is the array of temperatures with 0.1 K step, cp_arr interpolates the loaded specific heat
array to T_arr, heat_int calculates the amount of energy per unit of mass required to heat

up the sample from the minimal temperature to all temperatures `T_arr`. That way, having an
amount of deposited heat calculated with Eq. 2.18, which is `heat_pulse_ip` in Fig. 2.11, we can
calculate the two-dimensional temperature distribution `T_pulse`. The deformation `deform_x`
is calculated the same way, where `deform_init` is the relative deformation that would be
accumulated during heating from T_{init} to temperatures `T_pulse`.

```python
jiter=0
while (jiter<iter_num):
    lambda_pulse = np.interp(T_pulse_z,T_arr,lambda_arr)
    cp_pulse = np.interp(T_pulse_z,T_arr,cp_arr)
    T_pulse_z[-1]=T_init
    T_pulse_m1 = np.roll(T_pulse_z,1)
    j_up=(T_pulse_m1-T_pulse_z)*lambda_pulse/dz
    j_up=j_up#*x_area
    j_down=np.roll(j_up,-1)
    j_up[0]=0
    j_down[-1]=0
    dT_dt =(j_up-j_down)/(cp_pulse*rho*dz)#*x_area)
    T_pulse_z+=dT_dt*dt*1e2

    jiter+=1
```

Figure 2.12: The code for heat flow defined by Eq. 2.22.

Fig. 2.12 shows how heat flow is implemented in code. The number of steps `iter_num` is
selected such that the time step of the heat flow calculation is sufficiently small for the calcula-
tion not to have numerical errors. The heat flow is calculated for the temperature distribution
`T_pulse_z` along depth for each radius. The thermal conductivity `lambda_pulse` and spe-
cific heat `cp_pulse` are calculated for each temperature. `T_pulse_z[-1]=T_init` the third of
boundary conditions in Eq. 2.23. `T_pulse_m1` is needed to calculate the gradient of temperature
which is then used to calculate the heat flow `j_ip` defined by the temperature gradient. For a
given layer, the temperature change is defined by the difference of incoming and outcoming heat,
as defined in `dT_dt`.

The step along depth `dz` needs to be sufficiently small for the calculation to have no errors.
The maximum depth is by the intensity of pulses and duration of train. Practically, for the
given parameters a user needs to gradually increase the maximum depth to an extent when
further increase of depth does not affect the temperature distribution, i.e. such that temperature

distribution converges.

2.3.2   Takagi-Taupin approach to diffraction in deformed crystals

In Sec. 2.3, diffraction is considered as in a semi-infinite crystal with deformation Eq. 2.26, which does not account for diffraction in the crystal volume. Takagi-Taupin equations allow to calculate diffraction of X-rays in a two-dimensional mesh with a given deformation in each point, such that diffraction can be simulated for the two-dimensional temperature profile.

Having two-dimensional deformation distribution, it is feasible to calculate the diffracted intensity at crystal surface taking into account the diffraction in the crystal volume. The method of numerical implementation of Takagi-Taupin equations is presented in [37]. Below, the theory is briefly introduced and simulations of diffraction for sample two-dimensional temperature distributions are presented.

We can analyse the effect the deformation gradient has on the formation of diffracted wave using Fig. 2.13. The deformation field from COMSOL calculated in radial symmetry is mirrored along $R = 0$ line to provide the mesh for Takagi-Taupin equations. The deformation has a strong gradient near $R = 0$ and $z = 0$, which leads to weak diffraction near $z = 0$ and $x = 0$. Further from the center, the deformation gradient is weaker, and diffraction is stronger.

In Sec. 2.2, the wave equation Eq. 2.7 is solved using Eq. 2.8, where the amplitudes of incident and diffracted waves $A_{0,h}$ are constant and the resulting electric field is defined by the periodic susceptibility. In non-uniform crystals, e.g. deformed, the absence of periodicity makes it impossible to use Eq. 2.8 that considers a uniform crystal. Instead, incident and diffracted electric fields $E_{0,h}$ need to be calculated for each point of the crystals in order to account for the varying deformation. At each point of crystal volume, the increment of the diffracted wave along the diffracted wave direction can be calculated according to Takagi-Taupin equations [37] by

$$\frac{\partial E_h(\bar{r})}{\partial s_h} \sim \left[\chi_0 E_h(\bar{r}) + \chi_h \exp\{-ihu_z(\bar{r})\} E_0(\bar{r}) \right], \qquad (2.30)$$

where E_h is the amplitude of diffracted field, s_h is the step along diffracted wave direction, χ_0, χ_h are susceptibility Fourier components, $h = 2\pi/d$ is the reciprocal lattice vector, d is lattice spacing, $u_z(\bar{r})$ is the lattice deformation at each point, E_0 is the amplitude of incident field. The term $\exp\{-ihu_z(\bar{r})\}$ oscillates along diffraction direction when $u_z(\bar{r})$ changes by d. The increment of the electric field along the transmitted wave direction can be calculated using
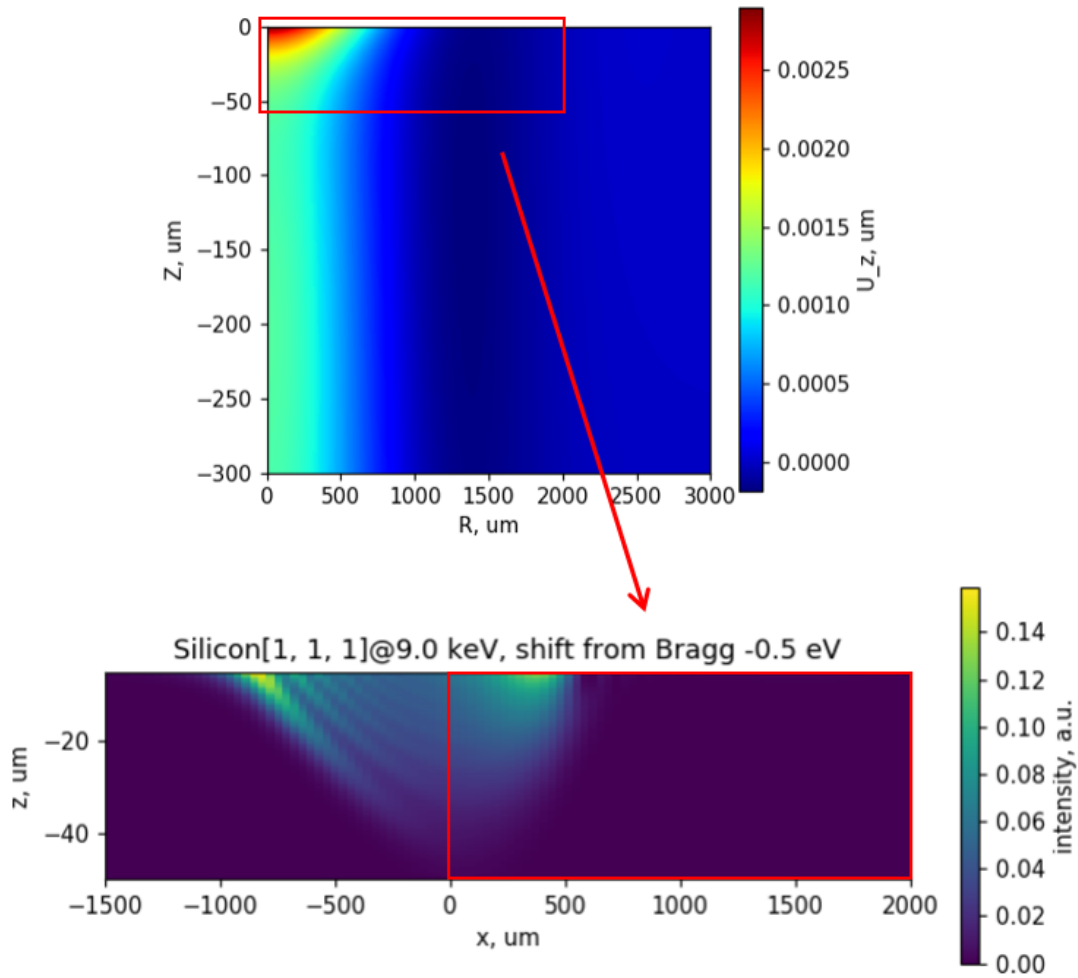
Figure 2.13: Two-dimensional deformation calculated with COMSOL (top) and the intensity of diffracted wave calculated using Takagi-Taupin equations (bottom).

$$\frac{\partial E_0(\bar{r})}{\partial s_0} \sim \left[\chi_0 E_0(\bar{r}) + \chi_h \exp\{-ihu_z(\bar{r})\}E_h(\bar{r}) \right], \qquad (2.31)$$

where s_0 is the step along incidence direction.

We can observe an increasing temperature gradient when we approach the hottest point of the crystal. This explains the characteristic oscillations in the intensity plot in Fig. 2.13 whose period gets smaller the closer one look to the point $x = z = 0$.

An example of Takagi-Taupin equations solution for non-deformed crystal and slightly deformed crystal is shown in Fig. 2.14. With no deformation, for the first pulse, the reflection amplitude is the same for all points of crystal surface, therefore the reflected pulse is Gaussian. For the deformed crystal, diffraction is defined by the deformation gradient. When deformation

gradient is non-zero, the diffracted intensity reduces along the direction of X-rays incidence due
to the rapidly changing lattice spacing. This, in turn, violates the constant lattice spacing con-
dition required by Bragg law and the diffracted intensity is reduced. When deformation gradient
reaches values close to zero, the diffracted intensity increases. Therefore, one can see the correla-
tion between the reflection amplitude and the gradient of deformation. Due to diffraction effects,
however, there're oscillations which originate from the X-rays that undergo diffraction deeper in
the crystal. Using Takagi-Taupin equations one can account for diffraction of X-rays at various
depths, absorption during propagation in crystal volume of diffracted X-rays and their effect on
the electric field at crystal surface.

For stronger deformation in Fig. 2.15, the deformation gradient reaches such high values in
some areas that there's no reflection.

In all, the solution of Takagi-Taupin equations enables to calculate the diffraction in a crystal
with an arbitrary deformation in each point of the crystal. This can be required to take into
account the temperature gradient in the crystal volume or the elastic deformations in the crystal.
For instance, the account of temperature gradient in the volume can introduce new diffraction
effects compared to Sec. 2.3.

Figure 2.14: The intensity of the incident Gaussian pulse (blue) at crystal surface, diffracted
intensity at crystal surface (red) and the relative deformation gradient at crystal surface (green)
for the first and third pulse in a train. For the 1st pulse, there's no deformation. Simulations
are done for Si(111) reflection 9.005 keV photon energy when the X-rays are incident at an angle
where the exact Bragg condition is satisfied for 9 keV. Two-dimensional deformation distribution
is calculated using COMSOL. The vertical axis on the left denotes the intensities, on the right -
deformation gradient along diffraction direction, the units of the gradient are in arbitrary units
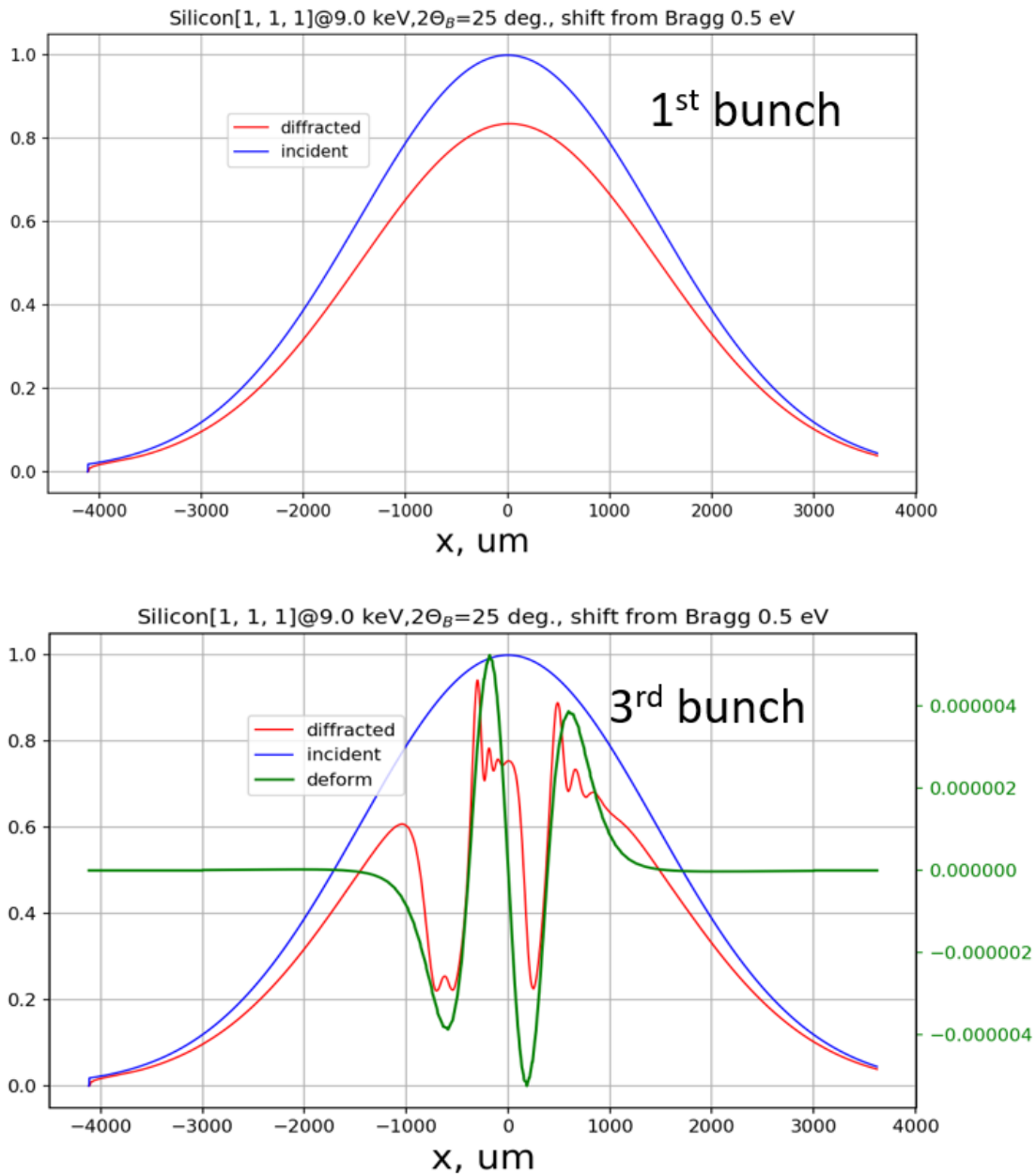and the scale of gradient is the same as in Fig. 2.15.
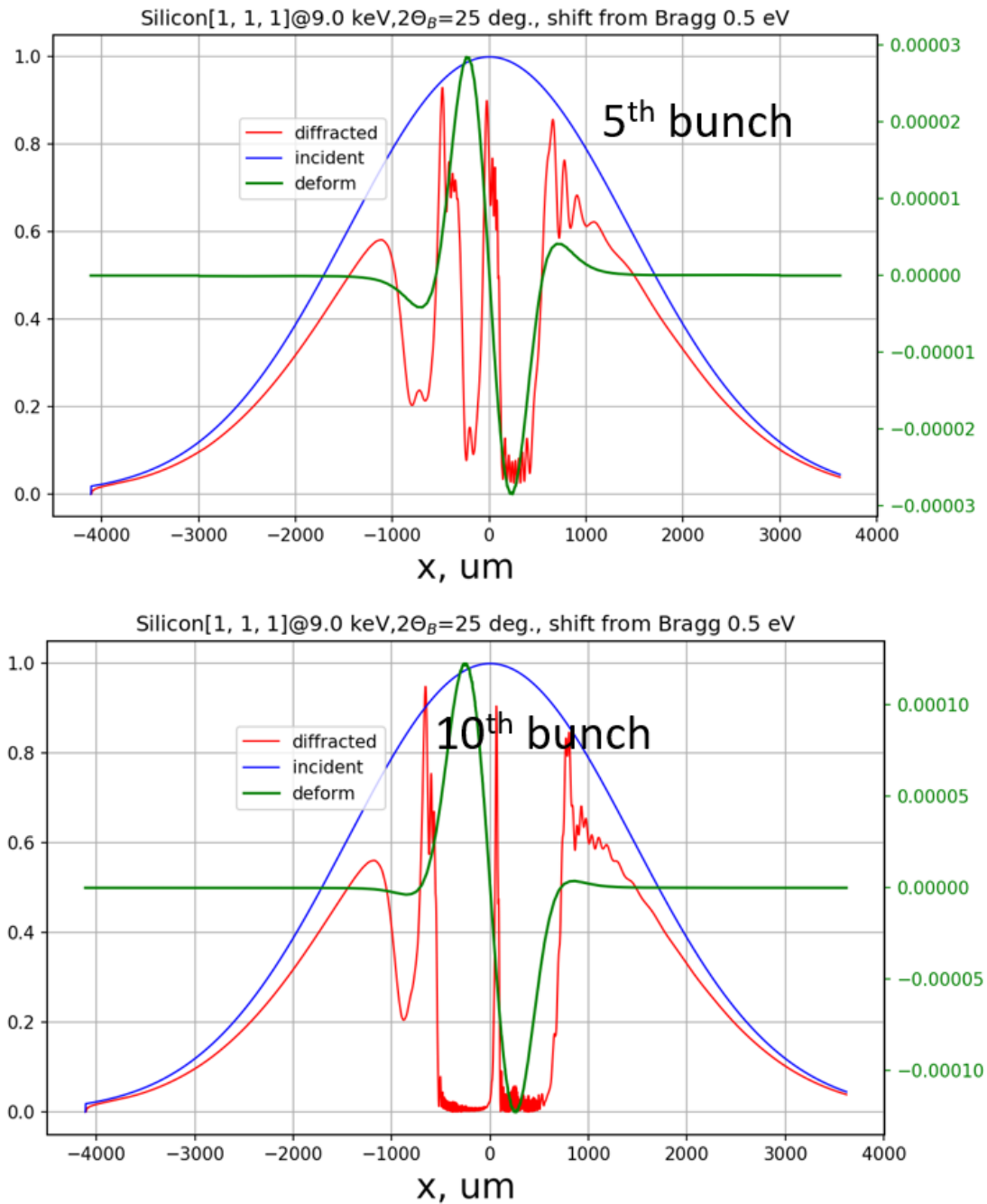
Figure 2.15: The intensity of the incident Gaussian pulse (blue) at crystal surface, diffracted
intensity at crystal surface (red) and the deformation gradient at crystal surface (green) for fifth
and tenth pulse in a train. Simulations are done for Si(111) reflection 9.0005 keV (corresponding
to 0.5 eV shift from the central photon energy 9 keV, as shown in plots titles) photon energy
when the X-rays are incident at an angle where the exact Bragg condition is satisfied for 9 keV.
Two-dimensional deformation distribution is calculated using COMSOL.

2.4 Effect of asymmetric diffraction on spatial properties of x-ray pulses and its applications at experiment

Prior to the discussion of the wavefront propagation results, we analyse the effect of asymmetric diffraction using geometrical considerations. In Fig. 2.16 a sketch of asymmetric Bragg reflection is shown. The angle of incidence $\vartheta_0 = \vartheta_B + \psi$ and the reflection angle $\vartheta_h = \vartheta_B - \psi$, where ψ is the asymmetry angle and ϑ_B is the Bragg angle for a given reflection and photon energy. The reflected pulse slippage (shown in yellow) is defined by the difference between the projections of the footprint on the incidence direction (dotted green line) and on the reflected pulse propagation direction (magenta line). The ratio of the "slippage" and the reflected wavefront size in the propagation direction (shown in red) defines the skew angle φ for the asymmetric Bragg case:

$$\tan \varphi = \frac{\cos \vartheta_h - \cos \vartheta_0}{\sin \vartheta_h}. \tag{2.32}$$
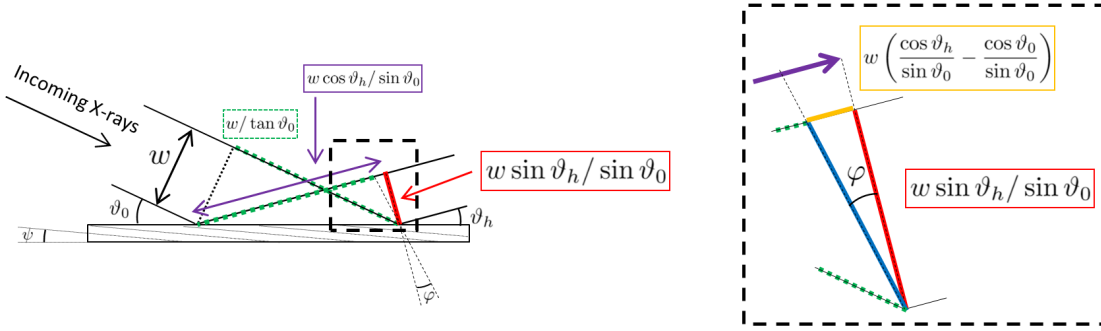
Figure 2.16: Geometry of the asymmetric Bragg case. Due to identical optical paths for the incident and reflected pulses (shown in dashed green lines), the reflected wavefront (shown in blue) is not perpendicular to the propagation direction after diffraction. The yellow line represents the optical path difference of the edges of the wavefront relative to the propagation direction. Dotted lines inside the crystal represent the diffraction planes for an asymmetry angle of $\psi = 5°$.

For Laue diffraction, the skewness is present in case of any angle between the diffraction planes and the surface. For the sake of simplicity, let us consider the symmetric Laue case. Fig. 2.17 shows the geometry of the reflection. In comparison to the asymmetric Bragg case, the slippage is represented by the sum of the projections of the footprint (dotted green line and magenta line). Due to the symmetry of the reflection, the wavefront size in the propagation direction does not change after diffraction. Therefore, the skew angle φ can be calculated from the following condition for the symmetric Laue case:

Figure 2.17: Geometry of the symmetric Laue case. The line colors denote the same as in Fig. 2.16.

$$\tan \varphi = 2 \tan \vartheta_B. \tag{2.33}$$

Let us demonstrate the effect of asymmetric diffraction on wavefront. Simulations are done using WavePropaGator (WPG) package [38] which is described in detail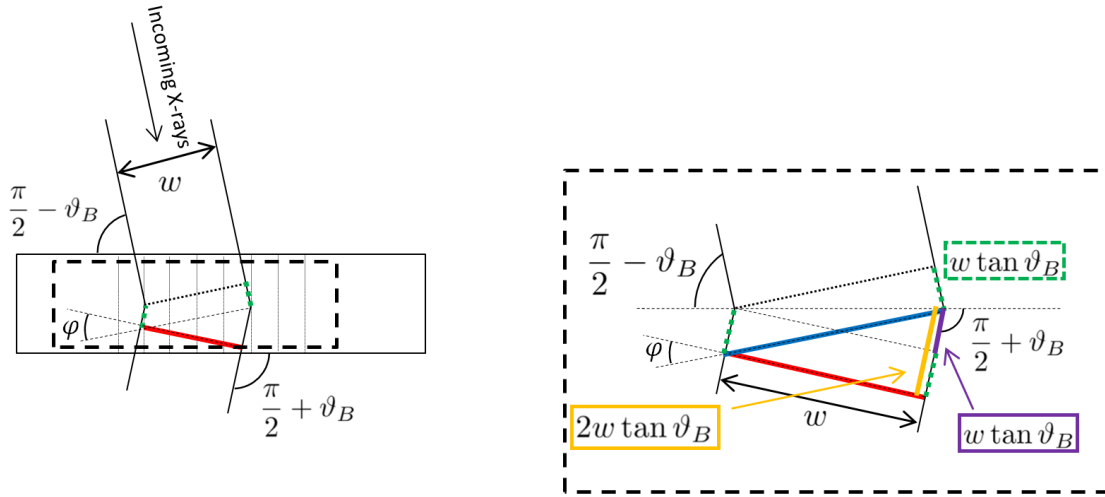 in Sec. 2.5. Diffraction of a self-amplified spontaneous emission (SASE) pulse with mean photon energy of 12.4 keV and duration of several tens of fs has been simulated. The electron bunch for the generation of such a pulse has a nominal charge of 100 pC with an electron energy of 17.5 GeV. The electric field of the pulse is generated using the code based on FAST algorithm [39] that is available online in the form of a database of pre-calculated photon fields for various configurations of the undulator and electron beam at European XFEL[36, 40]. In order to reduce the complexity, the pulse characteristics at the exit of the undulator is used in the simulations. The diffraction is considered in a Laue Si(111) 150 μm thick crystal oriented to have a maximum diffraction amplitude at 12.4 keV. In this case the lattice spacing is $d = 3.14$ Å and $\vartheta_B = 9°$, which results in a skew angle of $\varphi = 18°$ according to (2.33). Fig. 2.18 shows the on-axis time structure and photon energy spectrum of a pulse and a narrow ~ 8 eV region of the spectrum where the diffraction takes place.

The intrinsic asymmetry of Laue diffraction leads to a rapid change of the pulse structure after diffraction. Moreover, the pulse consists of two intense parts which merge during propagation. In Fig. 2.19 the intensity profile is shown at various distances from the crystal. At distances
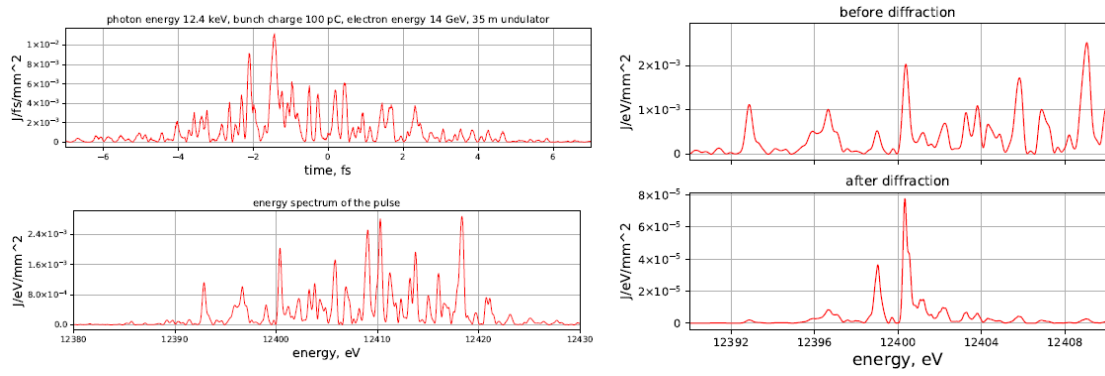
Figure 2.18: Left: simulated time structure (top) and spectrum (bottom) of a pulse at European XFEL, nominal bunch charge 100 pC; right: the portion of the spectrum where diffraction takes place before (top) and after (bottom) the crystal.

as short as several tens of centimeters the intensity profile in the scattering plane changes from having two intense areas into one pulse. Such an effect has previously been demonstrated for the diffraction of a sub-fs Gaussian pulse in two dimensions of the scattering plane [41]. In Fig. 2.20 it is explicitly demonstrated that at different y positions (across the beam) the pulse arrives at different times due to the skewness. At 2 cm from the crystal, the intensity profile has two intense areas with a tilt defined by the geometry of the reflection. For the given photon energy and reflection, from (2.33) the estimated skew angle agrees with the simulated profile.
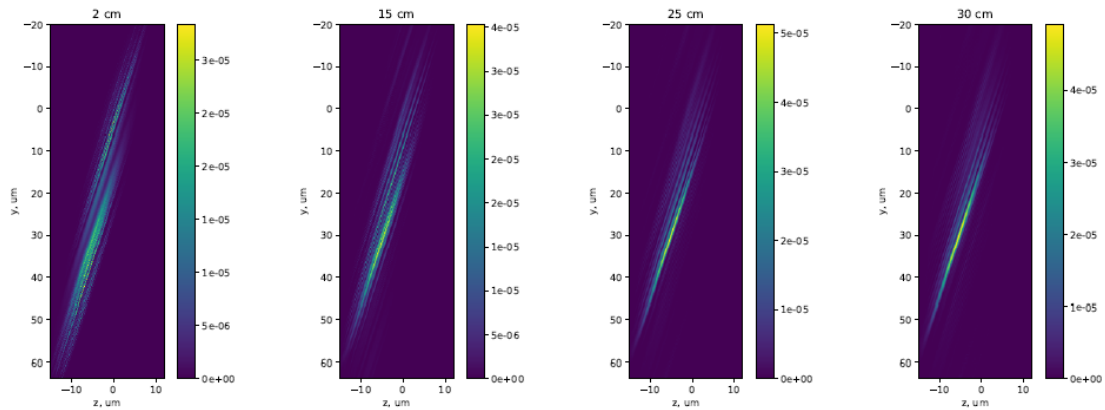
Figure 2.19: Simulated intensity profile of the diffracted pulse in the diffraction plane at various distances from the crystal. The y-coordinate is across the beam and z is along the beam propagation direction.

In a recent experiment asymmetric Bragg reflections have been used for a variable split-and-delay line[42] at Linac Coherent Light Source (LCLS). In such a system one part of the pulse undergoes a series of symmetric reflections, the other undergoes 2 symmetric and 2 asymmetric

Figure 2.20: Simulated intensity profile of a diffracted SASE pulse in the scattering plane 2 cm after the crystal with the theoretical estimation of the skew angle (left) and its cuts in time at various y coordinates (right).
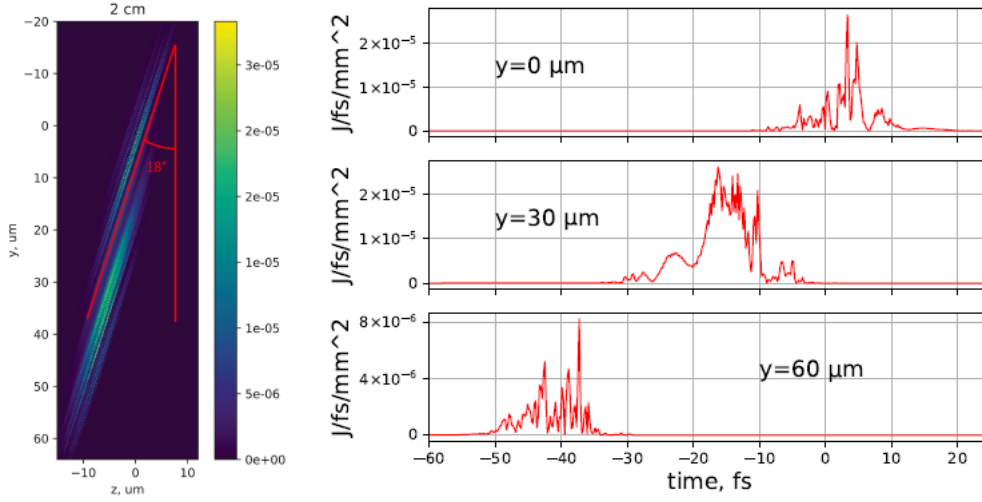
reflections. When the two pulses were temporally overlapped, an interference pattern was observed. In Fig. 2.21, simulations for the same scheme are presented. A 0.2 fs Gaussian pulse with amplitude waist 20 μm is considered at 100 meters from the waist. Such spatial parameters for the definition of the pulse provide the beamsize similar to the one used at experiment. The mean photon energy is 9.5 keV, the crystals are Si(220) and for the asymmetric crystals the miscut is 5°. The lattice spacing for the given reflection is $d = 1.92$ Å and $\vartheta_B = 20°$. Hence, the angle of incidence is $\vartheta_0 = 25°$ and $\vartheta_h = 15°$ is the direction of the reflected pulse. At the experiment with the variable split-delay line, 2 consequent asymmetric reflections were used. Applying the same procedure twice that led to Eq. (2.32) the resulting skew angle φ_2 after two asymmetric Bragg reflections can be calculated from

$$\tan \varphi_2 = \frac{\cos \vartheta_h - \cos \vartheta_0}{\sin \vartheta_h} \left(1 + \frac{\sin \vartheta_0}{\sin \vartheta_h} \right) = \tan \varphi \left(1 + \frac{\sin \vartheta_0}{\sin \vartheta_h} \right). \tag{2.34}$$

For the given reflection and photon energy one finds $\varphi_2 = 31°$. This estimation is in agreement with the simulated skew angle shown in Fig. 2.21. Possibly, the skew wavefront leads to the almost twofold decrease of speckle contrast observed in the experiment. Similar deteriorating effects in imaging experiments have previously been demonstrated with synchrotron radiation [43]. However, in optical experiments tilting of the wavefront has been used to the benefit of
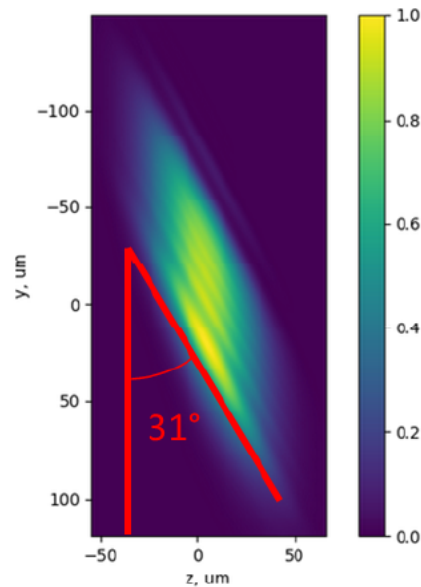
Figure 2.21: Simulation of the pulse propagation through a variable-channel cut split-delay system[42]: profile of the diffracted 0.2 fs Gaussian pulse in the scattering plane after 2 asymmetric and 2 symmetric reflections, the pulse propagates in the direction of negative z.

certain experiments [44] and it is demonstrated below how this could be transferred to the X-ray domain. In general, all optical elements from the undulator exit to the sample, such as mirrors and compound refractive lenses (CRLs), inevitably will distort the wavefront and change the angular divergence of the beam.

2.4.1 Laue diffraction case

In Fig. 2.19, propagation of a SASE pulse was studied at short distances which are feasible at experiment. It is however of physical interest to investigate the effect long distance propagation would have on the wavefront. For that, let us analyse how the wavefront of a Gaussian pulse evolves after Laue reflection, with and without lens inserted before crystal. The focal length of the lens in simulations was 0.475 m, such that the experimentally feasible distances of several meters would have a strong effect on the wavefront shape.

Fig. 2.22 shows the spectrum of a pulse before and after Laue diffraction. After diffraction, the spectrum has oscillations characteristic of Laue diffraction. This leads to the characteristic temporal structure shown in previous section. For the evolution of wavefront in free space, however, it is of greater interest how the pulse looks like in the reciprocal space. The angular spectrum, which is the wavefront in reciprocal space, is shown in Fig. 2.23. Without lens, the

Incident spectrum
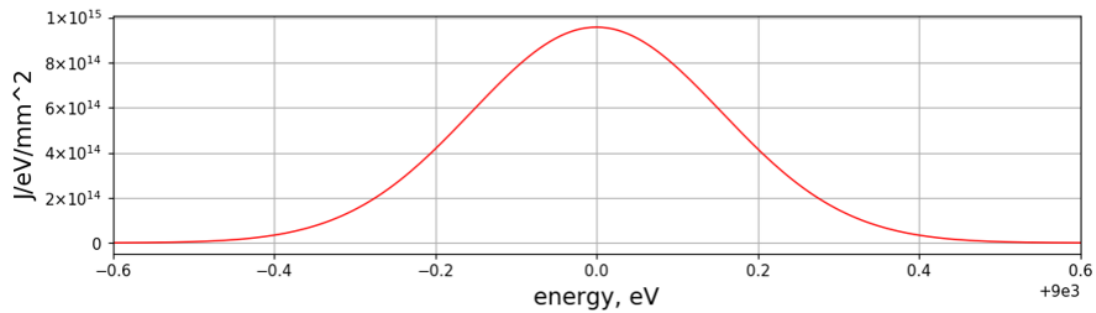
Diffracted spectrum
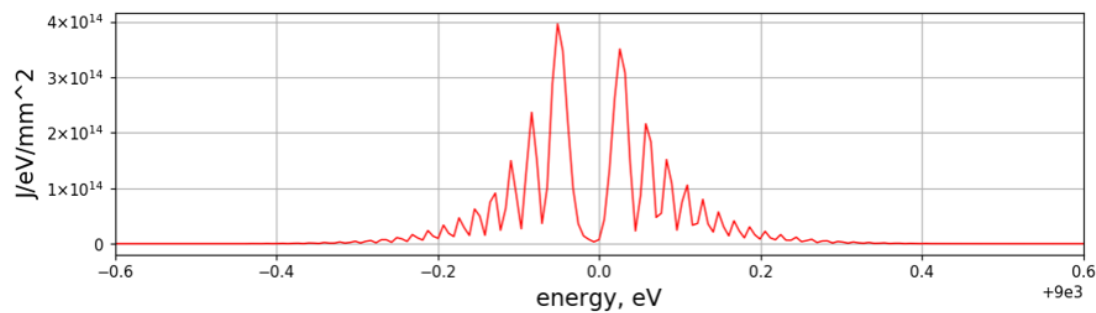
Figure 2.22: Photon energy spectrum of a Gaussain pulse whose bandwidth is 0.4 eV FWHM
(top) and the spectrum after diffraction in a C(220) Laue crystal, central photon energy 9 keV.

angular spectrum has two distinct peaks which lead to the redistribution of intensity in the
scattering plane seen in Fig. 2.19. At longer distances, as shown in Fig. 2.24, this leads to the
spatial disintegration of the pulse and appearance of oscillations.

In case of lens inserted before crystal, only the pulse divergence in horizontal direction can
be observed, as shown in Fig. 2.25. Due to the strongly defocussing lens the angular spectrum
of the diffracted pulse does not have two peaks, and therefore no redistribution in the scattering
plane takes place. Since the angular spectrum in horizontal direction, where no diffraction takes
place, is much wider, as seen in Fig. 2.23, one can only observe strong divergence in horizontal
direction.
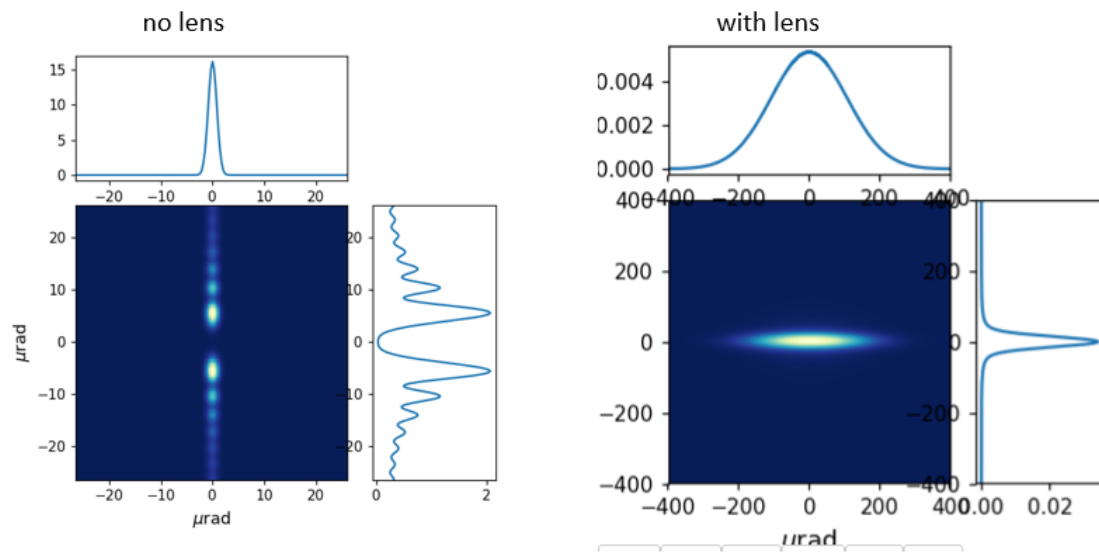
Figure 2.23: The wavefront in reciprocal space (angular spectrum) of a pulse after diffraction in
Laue crystal without lens (left) and with lens (right) before crystal.
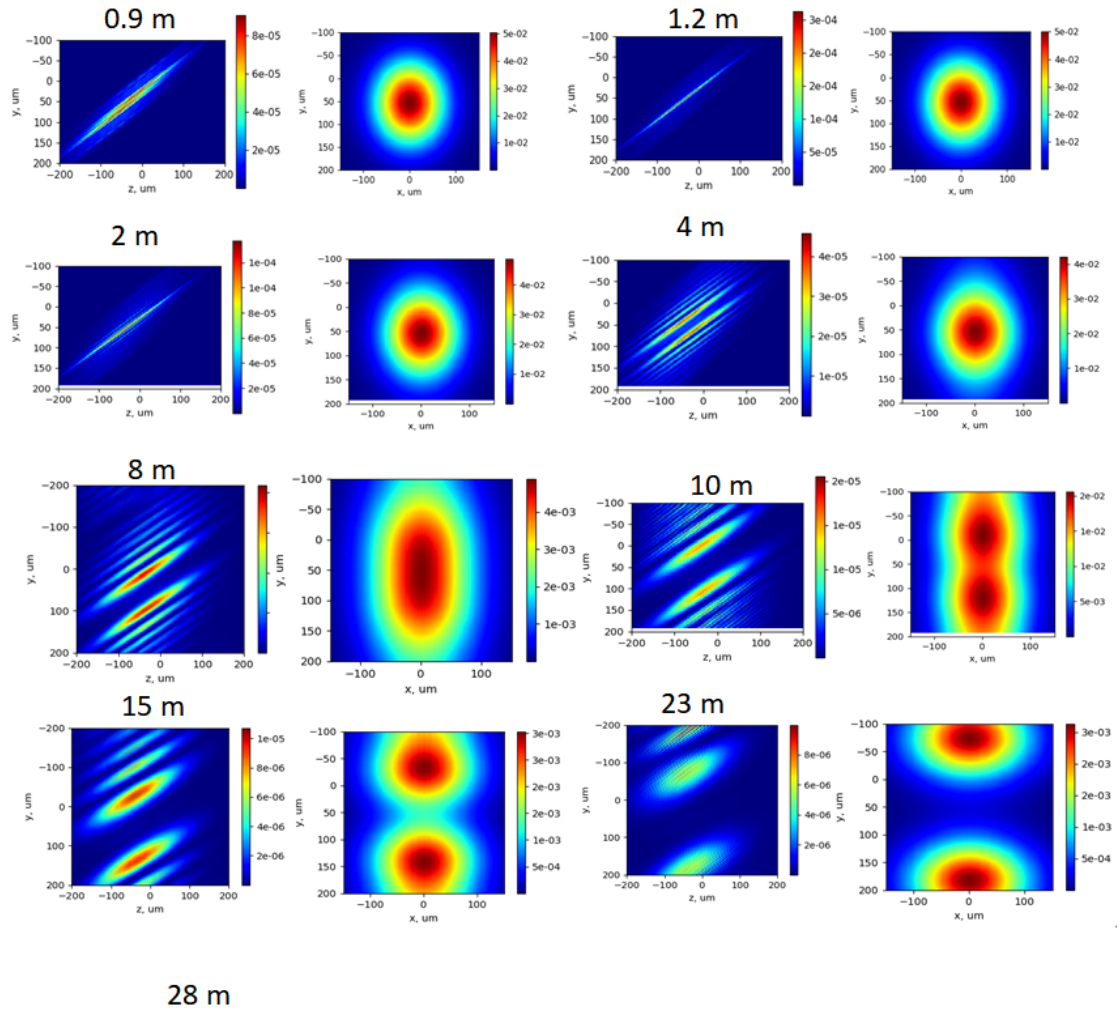
Figure 2.24: Wavefront in scattering plane (left) and the plane normal to propagation direction
(right) of the pulse after Laue diffraction at various distances.
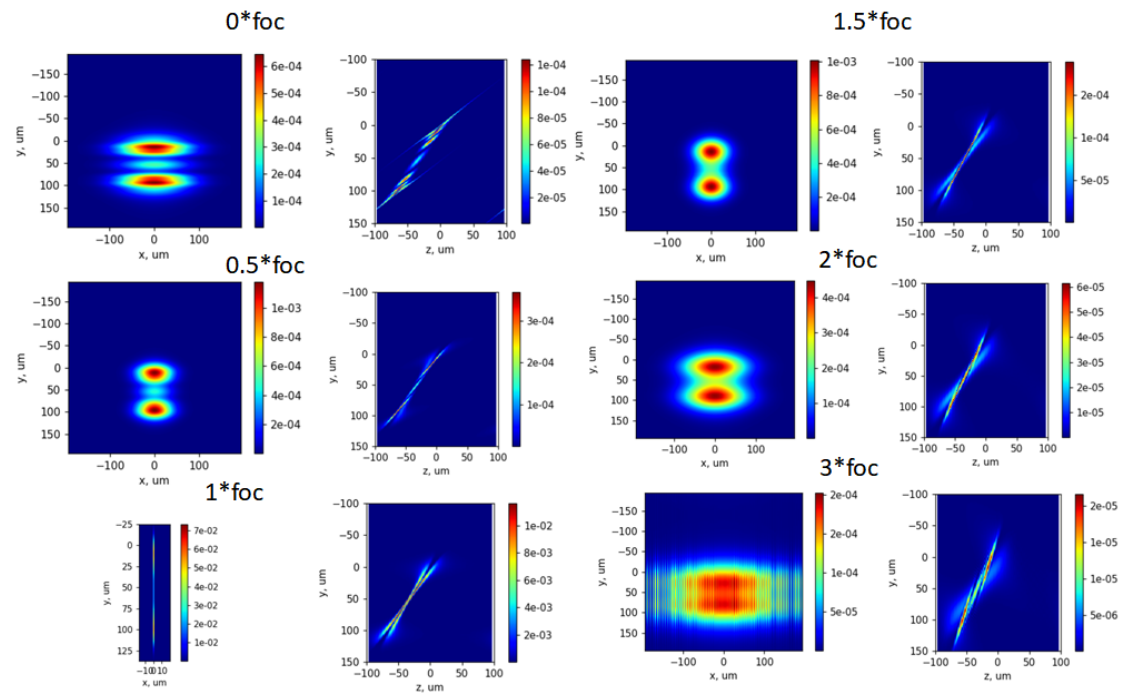
Figure 2.25: Wavefront in scattering plane (left) and the plane normal to propagation direction (right) of the pulse after Laue diffraction at various distances with lens inserted before crystal.

2.5 Asymmetric diffraction implementation in SRW software

WavePropaGator (WPG) framework [38], which is based on Synchrotron Radiation Workshop (SRW) [45], provides a user-friendly environment for propagation of XFEL wavefront through various optical elements.

In this section, upgrades to SRW towards Laue diffraction are reported. The theoretical framework for describing Laue diffraction is reviewed, followed by the introduction of various upgrades to the code. Due to the asymmetry of diffraction, the wavefront is not perpendicular to the propagation direction after diffraction, *i.e.* the wavefront is skewed. This effect is discussed within the framework of geometrical optics. The wavefront is simulated for a typical XFEL pulse after Laue diffraction and in asymmetric Bragg reflection the wavefront of a Gaussian pulse is simulated and compared with a recent experimental observations. Control of the wavefront skewness has the potential of improving certain X-ray scattering measurements.

The current version of SRW only provides the option of Bragg diffraction in crystals. The difference between the Laue and Bragg cases is illustrated in Fig. 2.26. In the symmetric Laue case, the diffraction planes are normal to the surface, thus the reciprocal lattice vector **H** is parallel to the surface, whereas in the symmetric Bragg case **H** is normal to the surface.
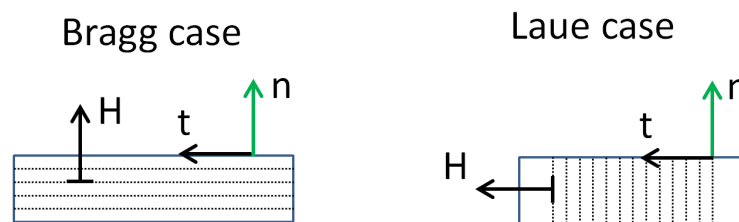
Figure 2.26: Geometry of the normal **n** and tangent **t** to the crystal surface, and the reciprocal lattice vector **H** for the symmetric Bragg and Laue cases.

Given that `alphrd` in the piece of code (Fig. 2.27) is the angle between the diffraction planes and the surface, the notation is valid for both Laue and Bragg case. That is, in the symmetric Laue case, `alphrd` $= \pi/2$. The diffracted and transmitted amplitudes (Fig. 2.28) are calculated using the formulae for the theory of dynamical diffraction of X-rays[27]. The suggested upgrades to the fraction of the code have been done in a local copy of SRW repository.

```
// From Input #5: reciprocal lattice vector coordinates
m_HXAi[0] = 0.;
m_HXAi[1] = cos(alphrd) / m_dA;
m_HXAi[2] = -sin(alphrd) / m_dA;
```

Figure 2.27: Definition of the components of the reciprocal lattice vector m_HXAi in SRW. Component [1] corresponds to the direction along the normal to the crystal surface, [2] - along the tangent to the surface, [0] is perpendicular to [1] and [2]. m_dA is the lattice spacing of a given reflection.

```
if(m_ug == 1)
{
    // Bragg Reflection
    DHsgC = x1C * x2C * (Cph2C - Cph1C)/(Cph2C * x2C - Cph1C * x1C);
    if(m_itrans == 1)
    {
        // Bragg Transmission
        D0trsC = Cph1C * Cph2C * (x2C - x1C)/(Cph2C * x2C - Cph1C * x1C);
    }
}
else if(m_ug == 2)
{
    //Laue Reflection
    DHsgC = x1C * x2C * (Cph1C - Cph2C)/(x2C - x1C);
    if(m_itrans == 1)
    {
        // Laue Transmission
        D0trsC = (Cph1C * x2C - Cph2C * x1C)/(x2C - x1C);
    }
}
```

Figure 2.28: Definition of transmission and reflection amplitudes for Laue and Bragg cases.

2.6 Conclusion

The presented theoretical models and simulations allow to simulate various effects of dynamical diffraction of XFEL pulses in crystals. The model for effect of heating on diffraction can be used to simulate the performance of crystal optics devices under high heat load. It was shown that a significant widening of the crystal throughput bandwidth is caused by heating, which hinders monochromator performance. The Python code is publicly available, transparent to the user and can be easily modified. The results using Takagi-Taupin approach are a first step towards wavefront propagation simulations of pulses after diffraction in deformed crystals. Asymmetric diffraction was studied using wavefront propagation. It was demonstrated that there's wavefront inclination which might benefit coherent scattering experiments. An upgrade to WPG software towards Laue diffraction was presented, which enables wavefront simulations of diffraction in Laue case.

Chapter 3

Performance of cryo-cooled monochromator under MHz repetition rate XFEL pulses

Firstly, this chapter provides an overview of the monochromators application at modern X-ray sources and how coherence scattering experiments benefit from them. By selecting a narrow fraction of the incident pulse spectrum, the monochromator improves temporal coherence of the pulses. With a longer coherence time, a larger volume of the scattering sample contributes to the coherent scattering and thus the signal gets improved. The pules at XFELs have such a high energy that monochromator crystals can be significantly heated and thus deformed to such an extent that the lattice deformations have a noticeable impact on the diffraction. The last section of this chapter addresses the heating of the cryo-cooled monochromator under intense X-ray pulses. The fundamental principles and framework of heating simulations are presented, followed by an overview of measurements of monochromator performance and their comparison with simulations.

3.1   Crystal monochromators at modern X-ray sources

To achieve the maximum transmission an avoid scattering from air X-rays are typically transported in vacuum at synchrotrons and XFELs. For instance, ID17 of European Synchrotron

Radiation Facility (ESRF) a pressure of 10^{-7} torr is used[46], whereas at EuXFEL a lower
pressure of 10^{-10} mbar ($= 0.75 \cdot 10^{-10}$ torr) is the design goal [23, 30].
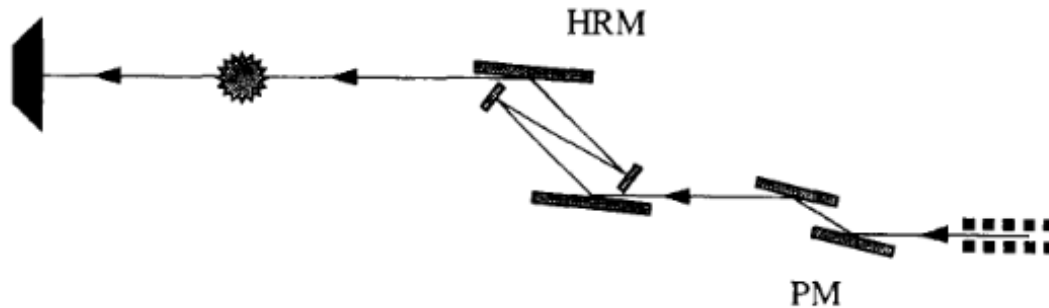
Figure 3.1: Sketch of monochromator at ID17 beamline of ESRF [46]. The high-heat load pre-
monochromator (PM) has Si(111) water-cooled crystals and X-rays are further monochromatized
by high-resolution monochromator (HRM).

One of the issues of X-ray monochromators at modern sources is the heat load. At ID17 at
ESRF, the first monochromator [46] operating with Si(111) reflections is designed to reflect at
a small angle and thus receive a lower density of X-rays at surface, which allows to monochro-
matize the beam without significant deformations to the lattice. The bandwidth of the white
beam radiation at ESRF is several percent of the central photon energy [47]. The monochro-
mator enables to reduce the bandwidth by two orders of magnitude down to around 10^{-4}. This
high heat load monochromator is constantly cooled by water. That way, the second high-order
reflection monochromator that receives X-rays at almost 90 degrees incidence angle and reduces
the bandwidth even further, down to 10^{-5} and less, does not receive as high heat load as the
first monochromator.

At EuXFEL, an artificial channel-cut monochromator is used whose sketch is shown in
Fig. 3.2. Such design allows to maintain the parallel orientation of crystals during rotation.
A piezo device attached to the top crystal allows for a finer alignment of the second crystal
relative to the first crystal.

The exceptional heat load produced by pulses with mJ energy arriving at MHz repetition
rates at EuXFEL pose challenges on X-ray optics. The silicon crystal monochromators operate
at cryogenic temperatures at EuXFEL since the linear expansion coefficient of silicon is close to
zero at such conditions, which leads to minimal lattice deformations due to heating by incident
pulses. Moreover, the heat conductivity of silicon is higher at low temperatures, such that the
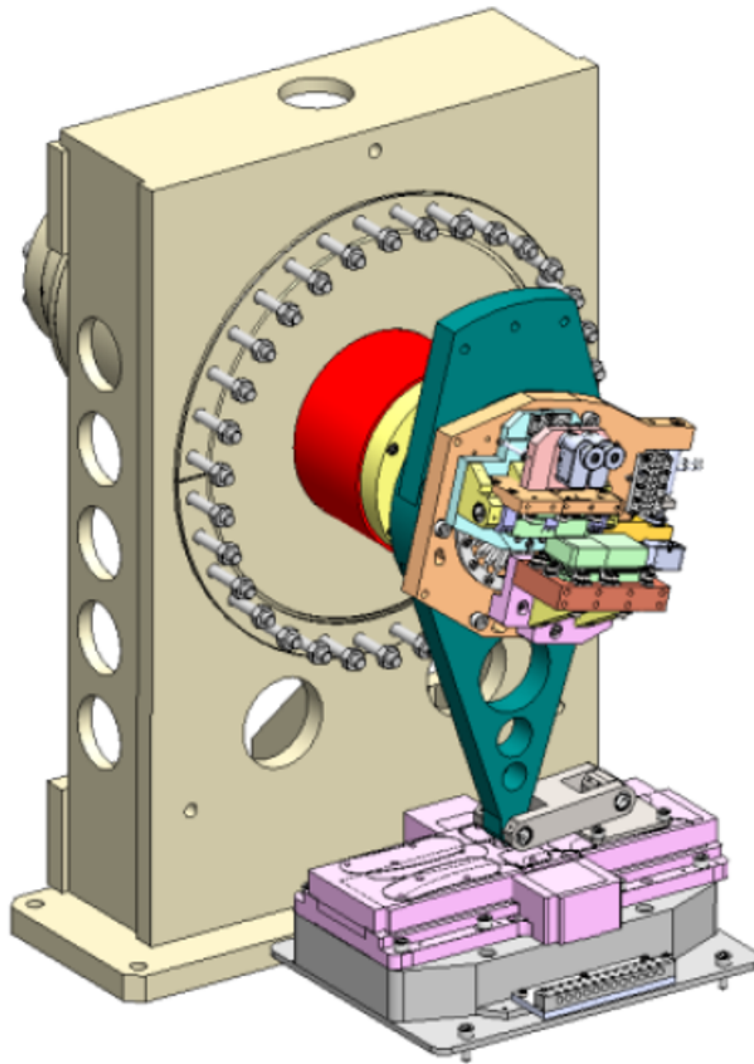
Figure 3.2: Scheme of artificial channel cut monochromator (ACCM). Linear translation at the bottom allows for simultaneous rotation of crystals.

heating induced by impinging pulses is effectively dissipated into the bulk. At EuXFEL, helium gas is used to enable the effective cooling of the silicon crystals down to cryogenic temperatures of around 100 K [23]. Compared to another widely used cooling agent nitrogen, helium has heat capacity of $5 \cdot 10^3$ J$\cdot$g/K in gaseous state, which is 5 times higher than heat capacity of nitrogen [48].

Despite the cryogenic conditions, at MHz repetition rates and mJ pulse energy the impinging power is so large that even at cryogenic conditions the heating affects monochromator performance. Sec. 3.3 uses the theory developed in Sec. 2.3 to analyze the effect sub-mJ pulses arriving

at MHz repetition rate have on the performance of a cryo-cooled silicon monochromator.

3.2 Benefits of using monochromatic XFEL pulses at coherent scattering experiments
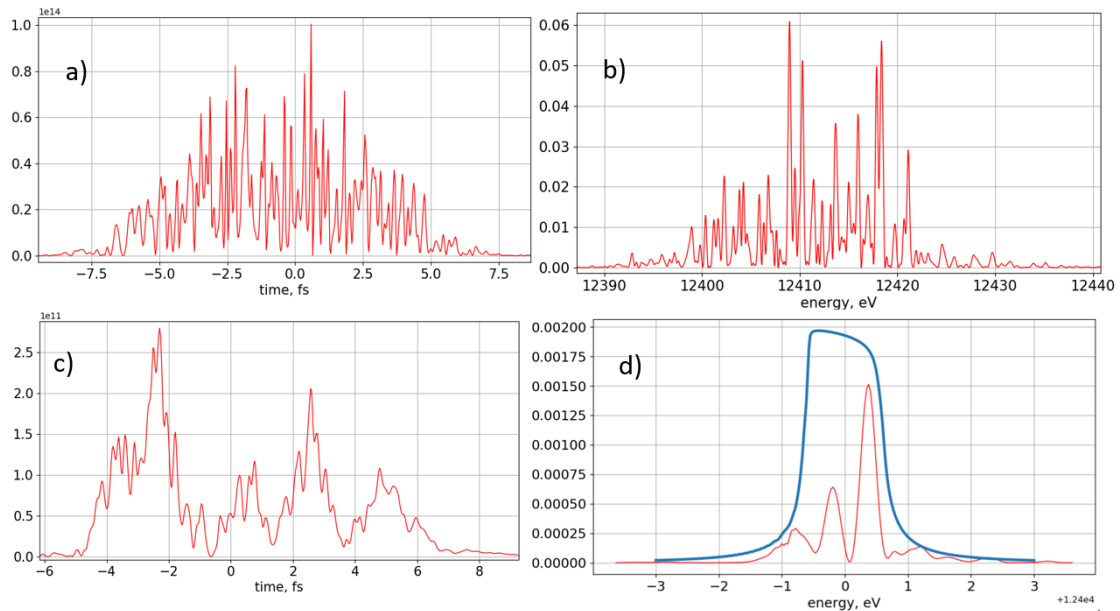
Figure 3.3: Time structure and spectrum of SASE pulse before and after Si(111) reflection. Time structure (a) and spectrum of a SASE pulse (b) produced from 100 pC electron bunch at 12.4 keV simulated with a package based on [49]. c) shows the the time structure of the pulse after reflection and d) is the spectrum after the reflection, the blue curve shows the Darwin curve of Si(111). The crystal cuts out a narrow portion of the incident spectrum corresponding to the Darwin width, see b) and d).

As described in Sec. 1.1, SASE pulses have a chaotic temporal structure. Fig. 3.3a) shows a typical temporal structure of a SASE pulse. It has short peaks with ~0.2 fs duration, which is the coherence time of SASE pulses at EuXFEL [50], see Fig. 3.3a). The duration of such spikes is defined by the SASE process, while the duration of the whole pulse is affected by the charge of the electron bunch and compression during acceleration and propagation through undulators.

Different spectral components of a pulse diffract differently, therefore, in order to simulate the diffraction of the pulse, one needs to first perform Fourier transform of the temporal structure of the electric field to calculate the spectrum. Fig. 3.3b) shows the frequency spectrum of the sample SASE pulse. The width of the spectrum is, according to Fourier transform principles, inversely proportional to the width of spikes in time structure, and the width of peaks in spectrum

is inversely proportional to the duration of the pulse. For SASE pulses at EuXFEL [40, 49] the relation holds $\Delta E \cdot \tau \simeq 2\text{eV} \cdot \text{fs}$, where ΔE is the FWHM of spectra and τ is the pulse duration at FWHM. This relation satisfies Heisenberg's uncertainty principle $\Delta E \cdot \tau \geq \hbar/2 \sim 0.3 \text{ eV} \cdot \text{fs}$ which defines the relation between the spectrum width and duration of a Gaussian pulse.

After diffraction in a crystal only a narrow portion of spectrum remains which is around 1 eV wide, compare Fig. 3.3b) and d). That way, the spectrum consists of a fewer number of modes, which increases the temporal coherence. This leads to the temporal structure of the pulse after diffraction having wider peaks with duration of several fs, see Fig. 3.3a) and c). Due to a huge portion of the spectrum being cut out, the pulse loses around three orders of magnitude in intensity, compare Fig. 3.3a) and c). However, at coherent scattering experiments such as X-ray Photon Correlation Spectroscopy (XPCS) in Wide-Angle X-ray Scattering (WAXS) the speckle contrast depends on the so-called coherence volume, which is defined by the coherence in both time and space [17, 18]. Since the spatial coherence is not affected by the diffraction (the angular divergence of pulses at EuXFEL is well below the rocking curve width of Si(111) at 12.4 keV), the increased temporal coherence after reflection from crystal results in a larger coherence volume, which, in turn, increases the speckle contrast. At such experiments, one should estimate, based on a signal-to-noise calculation, whether the increased contrast is justified compared to the several orders of lost intensity. In case of significant heat-induced deformation, however, the diffraction can disturb the wavefront thus affecting the spatial coherence of the pulse. The effect of diffraction in deformed crystals is simulated in Secs. 2.3.2 and 3.3.

Studying of material properties at small length scales requires tight focussing of X-rays on the sample. Monochromatization eliminates chromatic aberrations that lead to various photon energies being focused at various distances thus increasing the beamsize at a single selected distance. Nanofocusing by chromatic optical elements like CRLs was simulated to benefit from monochromatization [51].

3.3 Effect of heating on the monochromator throughput at cryogenic conditions and CW mode considerations

This section uses the formulas developed in Chapter 2. Let us analyze the effect of the heating on the monochromator performance using the following parameters: pulse size $w = 549$ µm, repetition rate 2.25 MHz, $T_{\text{init}} = 100$ K, pulse energy 1 mJ. The temperature reaches values in
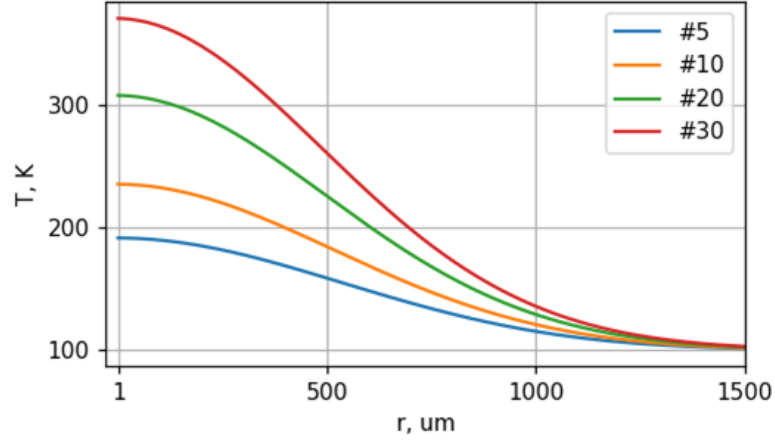
Figure 3.4: Simulations of the effect of heating on the cryo-cooled Si monochromator performance
[24]: simulated temperature profile at the surface for various pulses in a train, the legend provides
the number of pulse. Pulse size $w = 549$ µm, repetition rate 2.25 MHz, $T_{\text{init}} = 100$ K, pulse
energy 1 mJ.
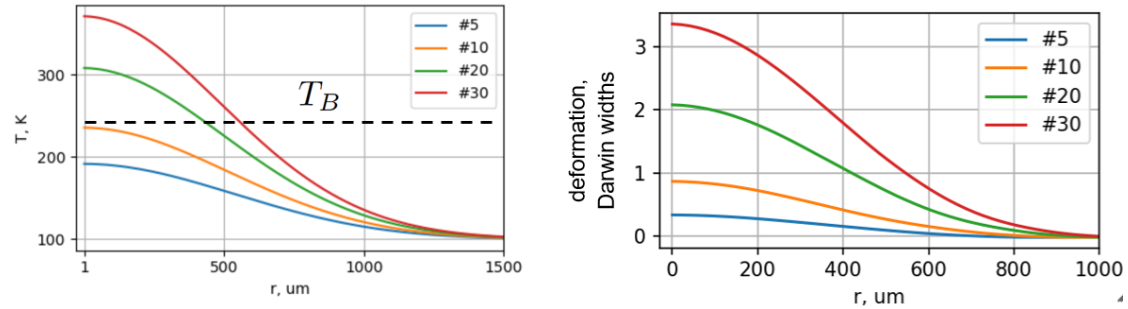
Figure 3.5: a) - simulated temperature profile at surface for various pulses in a train, the legend
provides the number of pulses, the dashed line defines the temperature at which the lattice
spacing is so large that the Bragg's condition is one Darwin width away from the initial one, b)
- deformation at different radii for the temperature distributions in a). Parameters are the same
as in Fig. 3.4.

excess of 300 K after 20 pulses, see Fig. 3.4). In order to study the effect of heating on diffraction

we define the temperature at which the deformation is so large that the Bragg condition is a

Darwin width away from the initial situation, i.e. the T_B that satisfies

$$\int_{T_{\text{init}}}^{T_B} \alpha_T (T) \, dT = 2|\chi_h|/ \sin \theta_B. \tag{3.1}$$

Fig. 3.5a) shows the temperature at each radius with T_B, and Fig. 3.5b) shows

52
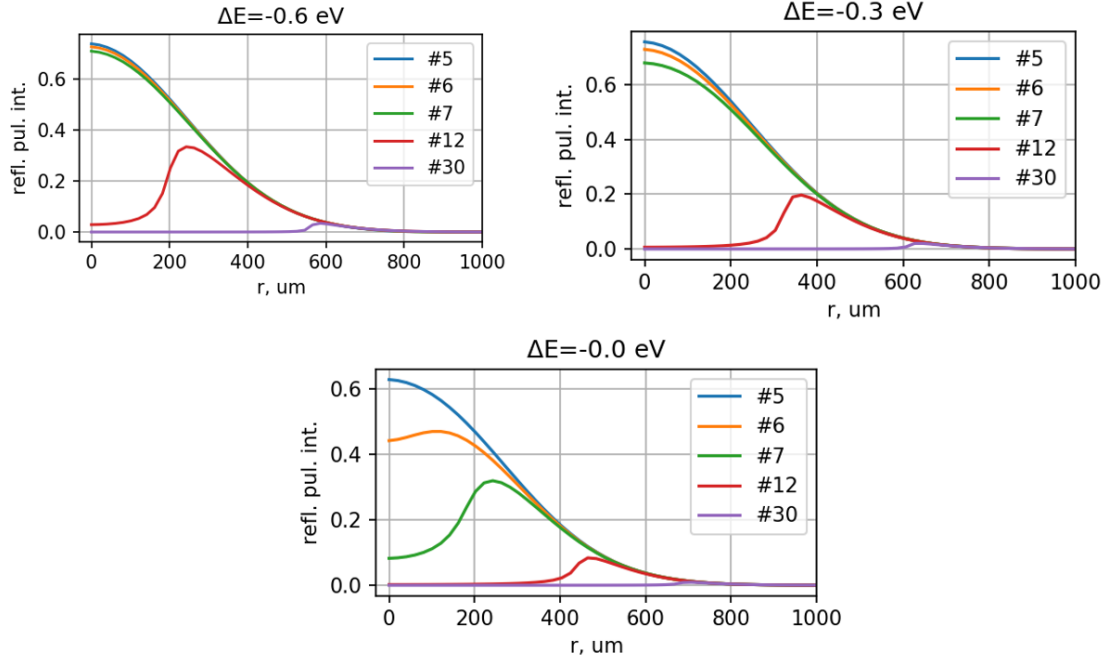
Figure 3.6: Reflection intensity along radius for different pulses in a train at three photon energies
(in figures titles) within Darwin width which is 1.2 eV, the intensity is in arbitrary units.
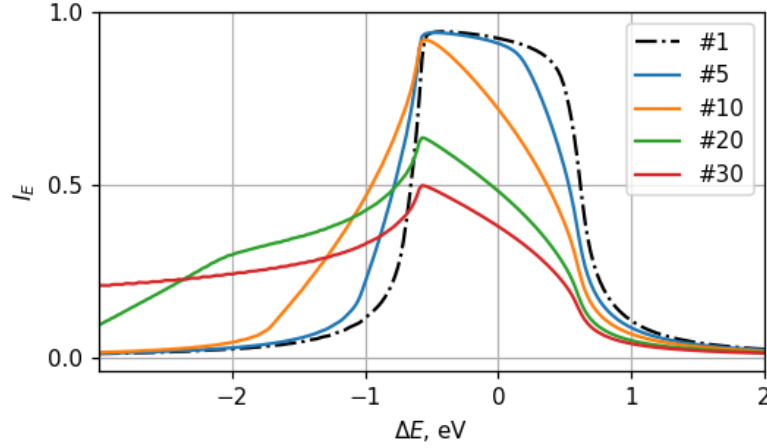
Figure 3.7: Darwin width (2.28) for the temperature distributions in Fig. 3.4, $\Delta E = 0$, 0.3 eV
and 0.6 eV correspond to the center of the dashed black line, which is the Darwin curve for the
cold crystal, at a half and a full Darwin width. At the left edge of Darwin width, reflection
intensity decreases slower, which agrees with Fig. 3.4.

$$\epsilon(r) = \frac{\int_{T_{\text{init}}}^{T(t,r,z=0)} \alpha_T(T)\, dT}{\int_{T_{\text{init}}}^{T_B} \alpha_T(T)\, dT} \tag{3.2}$$

using the deformation at T_B calculated in Eq. 3.1. One can see, for example, that heating from
100 K to around 250 K (after 10 pulses) leads to the deformation of a single Darwin width,
whereas further heating by around 100 K leads to additional more than two Darwin widths
deformation in the beam center due to the rapidly rising linear expansion coefficient shown in
Fig. 2.10. By applying Eq. 2.16 to the deformation in Fig. 3.5 at various photon energies, we can
calculate how reflection intensity at each radius reduces during heating, as shown in Fig. 3.6. At
the central photon energy, for instance, where the Bragg's condition is satisfied for non-deformed
crystal, deformation that corresponds to one Darwin width leads to a rapid decrease in reflected
intensity at $r = 0$. At lower photon energies, the exact Bragg condition is not satisfied initially
for the non-deformed crystal, and a stronger deformation is required for the reflection to reduce.
The radial profile of the diffracted field at surface allows to simulate wavefront propagation using
a Fourier optics approach. Moreover, by applying the two-dimensional temperature profile to
Takagi-Taupin equations presented in Sec. 2.3.2, one can account for the in-depth and radial
profiles of heating. This would require complex calculations and increased computational load.

Integrating the reflected intensity over the crystal surface for each photon energy, we can
calculate reflection curves for each pulse in a train, as shown in Fig. 3.7. In double-crystal
monochromators, reflection from two parallel crystals is used to keep the pulses propagating
in the same direction, therefore the transmission through the monochromator at each photon
energy is calculated as product of reflection of a heated crystal and cold crystal in Fig. 3.7, as in
Eq. 2.28. Due to the varying lattice spacing caused by deformation, the Bragg condition will be
fulfilled in a wider range of photon energies, but at each photon energy X-rays are only reflected
from a fraction of the crystal surface, such that the transmitted intensity is smaller than for a
cold crystal. This leads to rocking curves getting wider and less intense due to the heating. After
reflection from the second cold crystal, photon energies in its narrow bandwidth are transmitted,
such that the transmitted intensity for each photon energy is defined as the product of Darwin
curves for the cold and heated crystal. That is, for the example shown in Fig. 3.7, after 30 pulses
the integral of the product of the red and black dashed curves amounts to around 30% of the
initial transmission, i.e. black dashed curve, which is the integral of the Darwin curve for the
cold crystal.

Let us analyze how various pulse energies would affect the monochromator performance during
a train. At the bottom of the crystal the temperature is constant, according to boundary
conditions in Eq. 2.23, an any heat reaching that point will disappear, so we will further refer
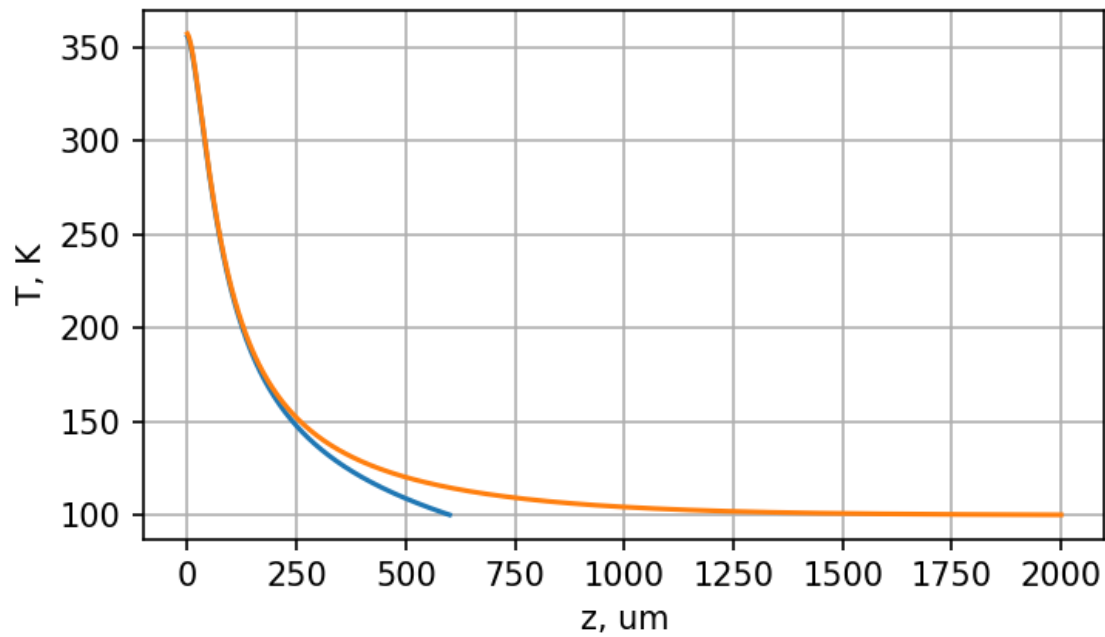
Figure 3.8: The temperature profile along depth direction after 180 pulses for heat sink located
at 600 and 2000 µm, where the curves reach $T = 100$ K. Pulse energy 0.3 mJ, beam size 550 µm,
repetition rate 2.25 MHz. At this pulse energy, the 600 µm depth of heat sink is sufficient to
simulate provide the same temperature at surface as for 2 mm thick crystal, and a smaller depth
reduces the computational load.

to the crystal bottom as heat sink. If we compare the heat profile along depth for different heat
sink locations in Fig. 3.8, we can notice that the temperature at the crystal surface is the same.
Moreover, when the heat sink is at 2 mm, there's significant heating only within the depth of
1 mm. In order to simulate heating at lower pulse energies, we would use heat sink located at
2 mm depth, since at lower pulse energies the same surface temperature would be achieved after
a larger number of pulses, such that a larger volume of crystal will be heated. In other words,
lower power will lead to the slower heating and heating profile along depth will be less abrupt,
such that the whole crystal depth will be heated.

Fig. 3.9 shows the transmission during a train, such that the same horizontal coordinate
corresponds to the number of pulses at which the impinged energy is the same. If we compare
2 mJ and 1 mJ energy, we see that the 1 mJ pulses cause weaker heating and the same time
interval between pulses leads to stronger heat dissipation, such that when 60 mJ have impinged
the monochromator, the transmission difference for 1 mJ pulses and 2 mJ pulses is 5% of the
initial transmission. With the decreasing pulse energy the tendency continues, such that at
0.1 mJ, for instance, the transmission after 600 such pulses is around 80% of the transmission of
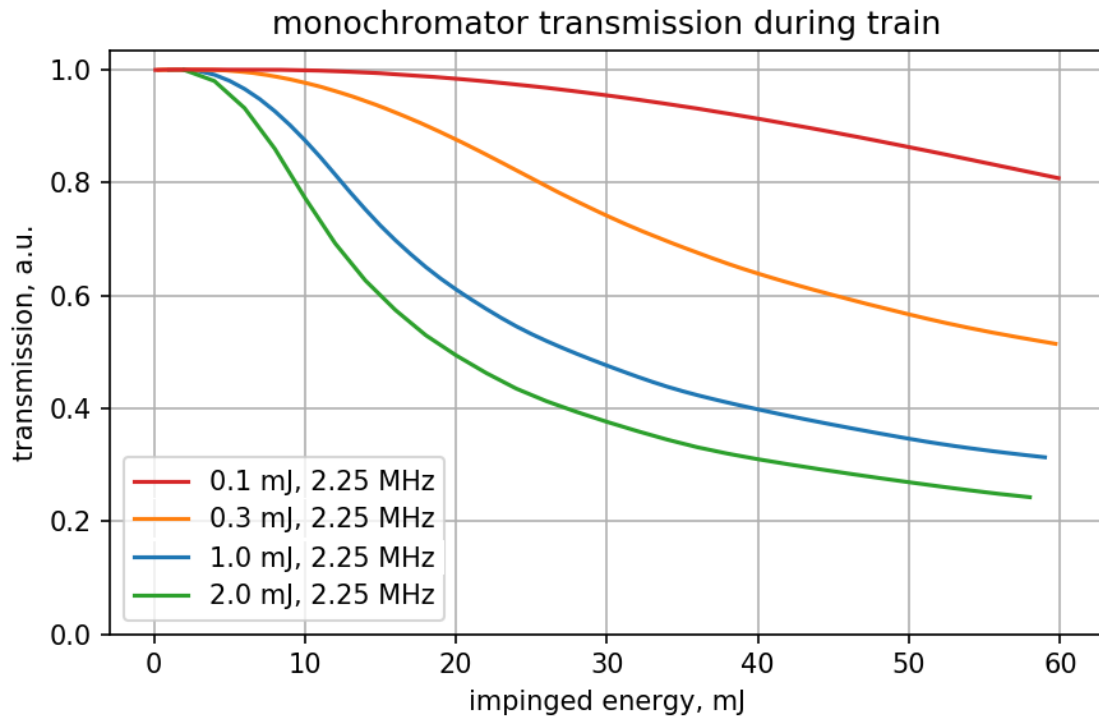
Figure 3.9: Monochromator transmission during a train for various pulse energies. Photon energy 9 keV, Si(111) reflection, heat sink has temperature 100 K located at 2 mm depth, size of incident beam 550 μm. The plot shows the transmission for the total energy that has impinged to crystal shown in the horizontal axis. 2 mm heat sink location is used in simulations for to compare the heating of the same crystal under different conditions.

cold monochromator.

If we consider the same power delivered at different repetition rates (e.g. 450 W for 0.1 mJ pulses at 4.50 MHz and 0.2 mJ pulses at 2.25 MHz, as shown in Fig. 3.10), the transmission is the same. This means that the difference between repetition rates is not sufficient for the heat flow to be significantly different, such that the heating is the same. At lower repetition rates the longer time separation between pulses will lead to the deeper penetration of the heat, and a deeper heat sink will be required in simulations.

SASE pulses have a random structure with a Gaussian envelope, such that on average the pulses have a certain width defined by the coherence time. For instance, in Fig. 3.3 the spectrum has a width of around 10 eV. In practice, the spectrum can be drifting in photon energy during a train, which leads to the changing incident intensity within the transmission bandwidth. For instance, if in the non-deformed state the monochromator is aligned to the maximum of a SASE spectrum with 10 eV bandwidth FWHM, a 2 eV photon energy shift will lead to 10% decrease of intensity within the bandwidth for the same alignment of monochromator.
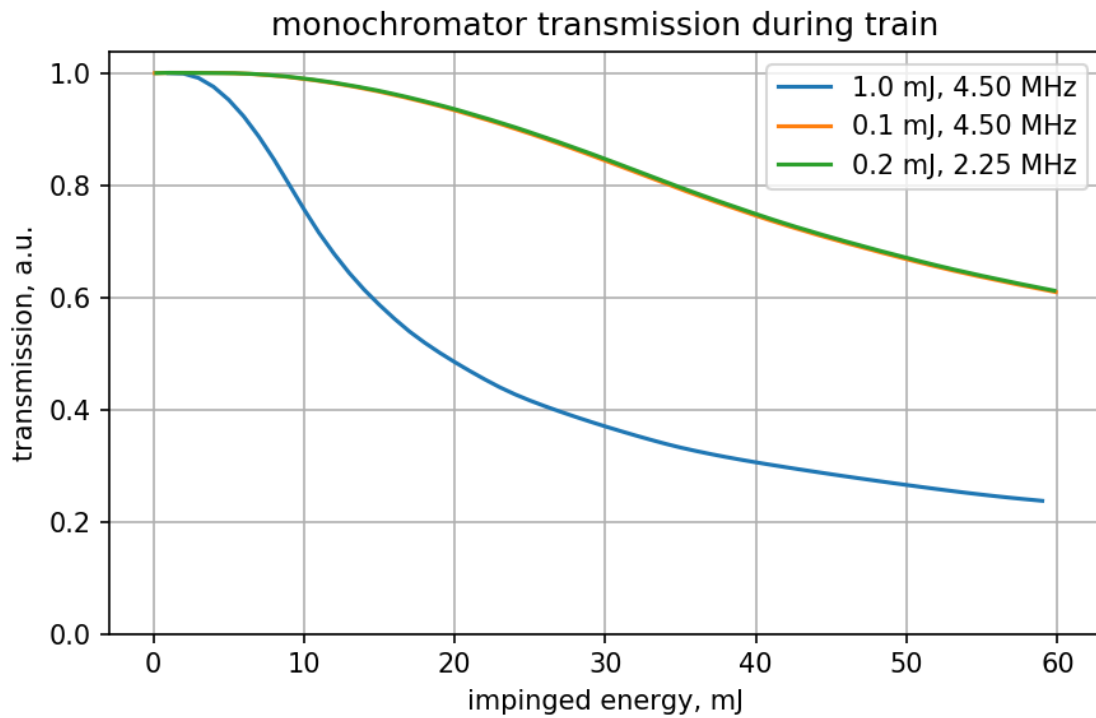
Figure 3.10: Monochromator transmission during a train for various pulse energies and repetition rates. The heating does not depend on the incident power for the orange and green curves, such that the curves overlap.

Several new FEL facilities [7, 8] are planning to operate in the so-called continuous wave (CW) mode at repetition rates reaching the MHz regime. In this mode, the pulses are not divided into trains and arrive at constant rate. Under CW illumination of MHz repetition rate and sub-mJ pulse energy, the heat would penetrate deeper with each pulse, such that an active heat sink will play a role. Even if an equilibrium temperature can be achieved, the deformation will be so strong that the monochromator transmission would be small. Since the cooling capabilities of a given device depend on the application of cryogenic parts to the crystal, the one dimensional model with a uniform and constant temperature at the bottom introduced above is not applicable. FEA software would enable the simulation of crystal heating in a given cooling device.

We can however roughly estimate the heat transfer properties under CW conditions using the one-dimensional model. Fig. 3.11a) shows how the temperature in the center of beam footprint increases when pulse energy is 0.1 mJ and repetition rate is 1.12 MHz, which corresponds to significantly weaker heat load compared to the burst mode presented above. We see that despite the weak heat load the temperature keeps rising approximately linearly.

If we look at temperature profile along depth in the beam center in Fig. 3.11b), we see that the
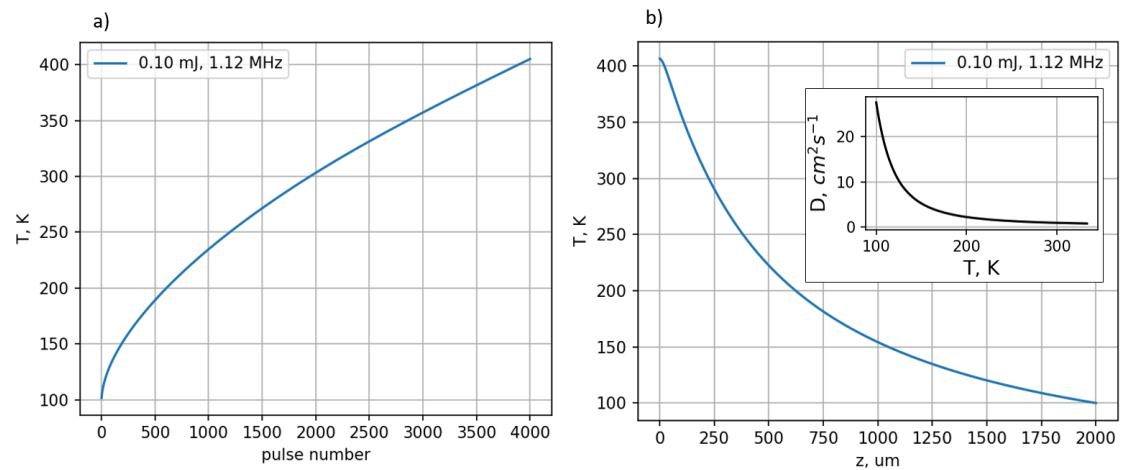
Figure 3.11: a) - temperature in the center of the beam footprint of crystal surface, b) - temperature profile along depth after 4000 pulses, the inset shows the heat diffusivity from Fig. 2.8. Each pulse has 0.1 mJ energy, repetition rate 1.12 MHz.

temperature steadily decreases when getting closer to the bottom of the crystal. If we also take into account that the heat diffusivity drops rapidly with rising temperature (inset in Fig. 3.11b)), we can note that at the crystal surface that is facing the impinging X-rays the heat diffusivity is weaker than at the bottom where the temperature is low and the heat diffusivity is larger. The next incoming pulse would increase the temperature at each depth, and the temperature change increases exponentially with depth, according to absorption in the crystal (at temperatures over 300 K specific heat in Fig. 2.6 does not change much). However, according to heat transfer equation Eq. 2.22, the temperature decrease depends on the second derivative of temperature along depth and the heat diffusivity. Over the 300 K difference along depth, the heat diffusivity changes by a factor of around 30, such that for the given parameters the temperature distribution would not reach an equilibrium. Probably, at a lower power such an equilibrium is feasible, since at lower temperatures the heat diffusivity in the beam footprint center would be higher and it would be sufficient for the heat to dissipate into the bulk for the given temperature gradient along depth. Moreover, the heat dissipation both along the crystal surface and along the depth might result in an equilibrium temperature.

At lower power, e.g. at synchrotrons with lower pulse energy and MHz repetition rates, or at XFELs with ~ 100 Hz repetition rate and sub-mJ pulses, the heating will be significantly weaker compared to mJ pulse energy and MHz repetition rates, and the model presented here cannot be applied since a larger volume of the crystal will be heated and the cooling will be defined by the design of a given device. That is, the temperature gradient will be similar in both radial and

depth directions, and the cooling mechanism of a particular device will need to be accounted for.
Moreover, due to the weak heating, the equilibrium temperature profile will likely have a weak
gradient that will not affect the diffraction and will be sufficient to dissipate the incoming heat.

3.4   Experimental studies of monochromator heat load

In order to measure the intensity of the pulses after the monochromator, a porous silica (Vycor)
sample was used to scatter X-rays in the forward direction (small-angle X-ray scattering, SAXS).
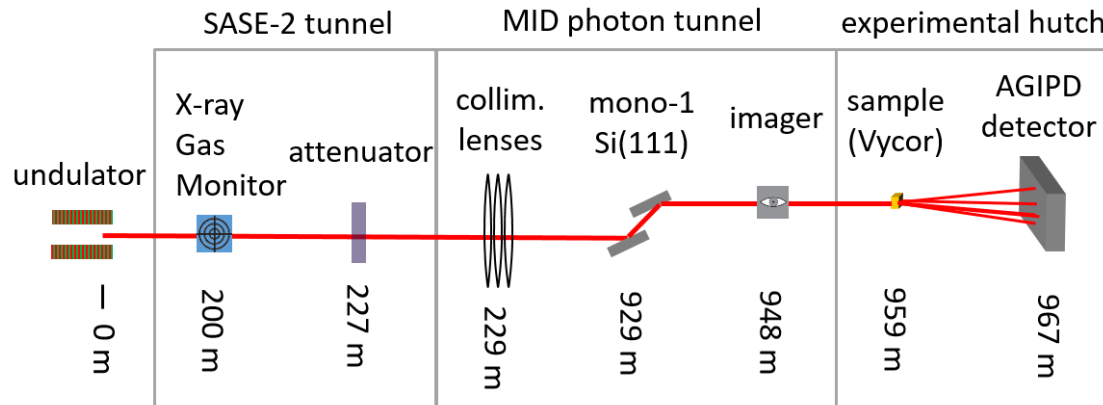
Figure 3.12: Selected components of MID station at European XFEL and their positions relative
to the source.

An overview of the beamline layout used at the experiment is shown in Fig. 3.12. The two-
dimensional intensity distribution of the beam was measured using the yttrium aluminium garnet
(YAG) screen imager device at the end of MID photon tunnel. The size of the beam was found
by applying a two-dimensional Gaussian fit to the intensity distribution, see Fig. 3.13a). The
horizontal FWHM width of the Gaussian fit $w_x = 607$ µm, the vertical - $w_y = 496$ µm; in the
simulations, $w = \sqrt{w_x w_y} = 549$ µm, such that the average density of the circular pulse that is
used in Eq. (2.18) is equivalent to the elliptical beam shown in Fig. 3.13a). The scattered SAXS
intensity was measured by the Adaptive Gain Integrating Pixel Detector (AGIPD) megapixel
detector, which is designed to acquire full-frame data at frequencies up to 4.5 MHz [52]. The
pulse intensity incident on the monochromator is measured using the X-ray gas monitor (XGM)
device[53] installed after the undulator. Attenuators installed after the XGM are used to reduce
the photon flux on the monochromator and the attenuator transmission was 30% during the
experiment. Collimating compound refractive lenses (CRLs) were used to compensate for the
divergence of the beam[54].
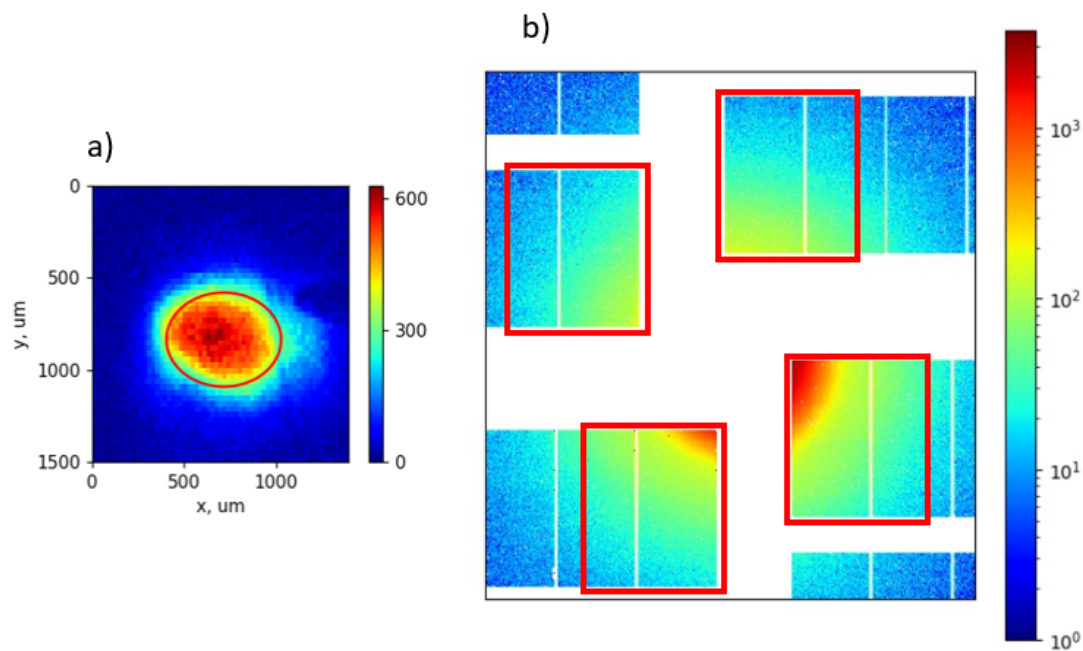
Figure 3.13: a) intensity distribution of a pulse after monochromator on the YAG imager, the
red ellipse is a contour at the FWHM of the two-dimensional Gaussian fit. b) Average over 60
images of the AGIPD area with the strongest SAXS signal. The red solid-line rectangles in b)
denote the four areas of the detector used for data analysis.

In order to measure the scattering from the Vycor sample on AGIPD, only the pixels located
closest to the center of the detector and having the strongest scattering signal were used for
analysis of the monochromator transmission (Fig. 3.13b). The ratio of the sum of the intensity
captured by the selected pixels to the XGM value provides a figure of merit for the transmission
of a given pulse in a given train. Averaging of this ratio over a large number of trains for each
pulse number provides an estimate of the monochromator transmission dependency on the energy
that has impinged on the first crystal.

The measurements show that the monochromator transmission reduces by a factor of two
after ~50 mJ of X-ray energy or around 150 pulses under the aforementioned conditions, have
impinged on the first crystal at 2.25 MHz repetition rate (Fig. 3.14). That is, the power of
~675 W (~0.3 mJ at 2.25 MHz repetition rate) incident at the cryo-cooled monochromator
decreases its transmission by a factor of two after about 60 µs. The experimental curves are
not shown with error bars, since the transmission values are averaged over many trains. That
is, for a fixed pulse number in a train, the scattering is produced by statistically independent
and intrinsically random SASE pulses [55]. Even for an ideal monochromator the transmission
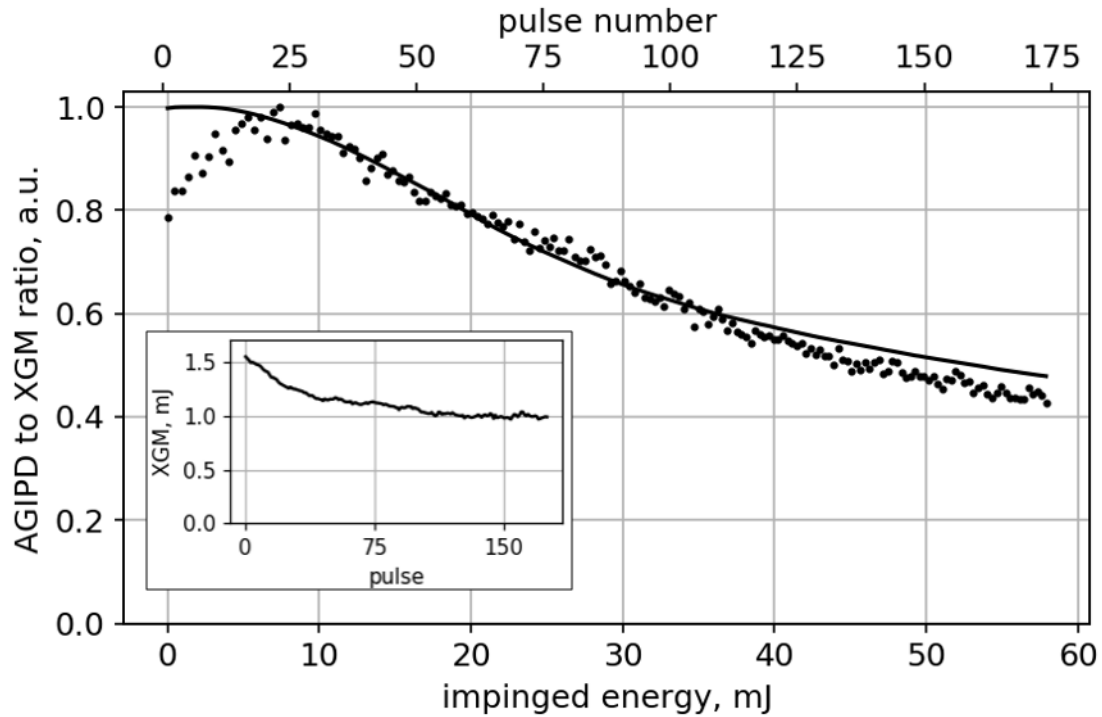
Figure 3.14: Experimental (dots) and theoretical (line) monochromator transmission during a
train of XFEL pulses [24]. The separation between pulses is 0.44 µs, which corresponds to
2.25 MHz repetition rate. A photon energy 9 keV and a Si(111) reflection was used. The
horizontal axis at the top represents the pulse number, at the bottom - the total energy that
has impinged on monochromator before the respective pulse. The inset shows the energy of each
pulse in a train measured by the XGM and averaged over the trains with 30% of the energy
impinges the monochromator. The experimental monochromator transmission is calculated as
the ratio of the sum of AGIPD pixels to the XGM signal for each pulse in a train, averaged over
498 trains and normalized to the maximum value. The experimental and theoretical transmission
values are normalized to the maximum values during the train.

is determined by the spectral intensity of the pulse in a bandwidth given by the Darwin width

of the monochromator. Due to the random nature of the spectral fine structure of SASE[55],

averaging over a large number of pulses provides an accurate estimate of the effect of heating on

the monochromator transmission. We attribute the initial rise of the measured monochromator

transmission seen in Fig. 3.14 to possible systematic drifts of photon energies and/or beam

pointing during a pulse train.

The good agreement between theoretical and experimental values in Fig. 3.14 indicates

that the simulation model presented in Sec. 2.3 provides a quantitatively correct behaviour of

monochromator transmission during heating by intense X-ray pulses. Therefore the model can

be employed as a simulation framework to aid the design of crystal optical devices when a high

heat load from intense XFEL pulses is anticipated. The implementation of the code in Python
is available to the public [31].

At previous measurements, which are presented in the next section, it was attempted to
track the monochromator performance during a train by using train-resolved measurements, i.e.
a single image for all pulses in a train. Since in Fig. 3.7 the rocking curve of the heated crystal is
simulated to get wider, it was intended to rock the second cold crystal, such that the widening
of the measured rocking curves would indicate the crystal heating.

3.4.1 Measurement with scintillator screens

Prior to using the MHz-capable detectors presented above, there were numerous attempts to
measure the monochromator performance under high heat load using imager devices that measure
the intensity distribution integrated over a train. The intention was to measure the total intensity
after the monochromator for different rocking angles of the second crystal of the monochromator
thus measuring the convolution of the heated and cold crystals rocking curves shown in Fig. 3.7.
Since the rocking curve widens during the heating of the first crystal, the measured rocking
curve would be wider for higher number of pulses. Simulations presented in this section use a
radial flow model instead of depth-flow model presented in Sec. 2.3 which allowed for simpler
simulations that did not contradict with the measurements in this subsection.
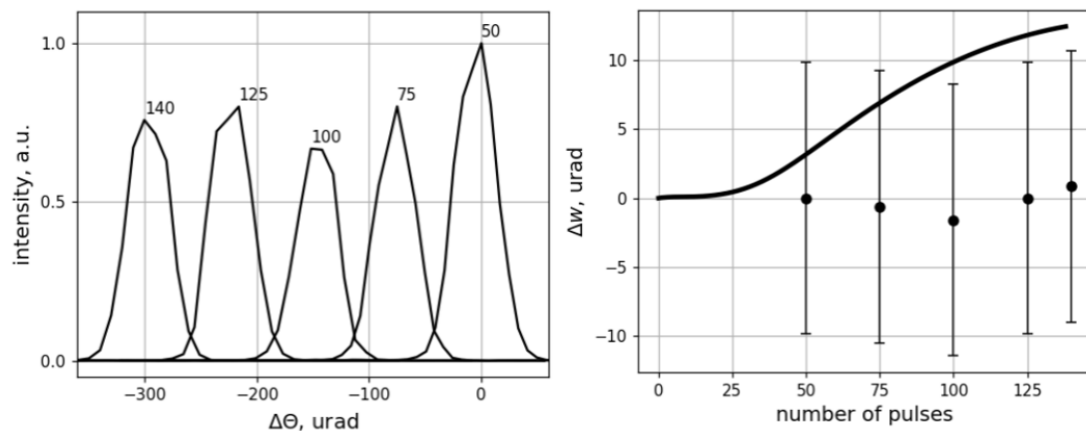
Figure 3.15: Left - rocking curves for various number of pulses in a train, right - the change of
width of the rocking curves at experiment (dots) and in the simulations (line) [56]. The error bars
denote the step of the second crystal rocking. Photon energy was 9 keV, pulse energy around
0.25 mJ, pulse size around 0.5 mm.

The first measurements shown in Fig. 3.15 did not indicate any widening of the rocking curve
[56]. This may have been due to low signal at imager, losses in beamline components between

monochromator and imager, as well as the large steps of the second crystal rocking which was
larger than the expected rocking curve widening.
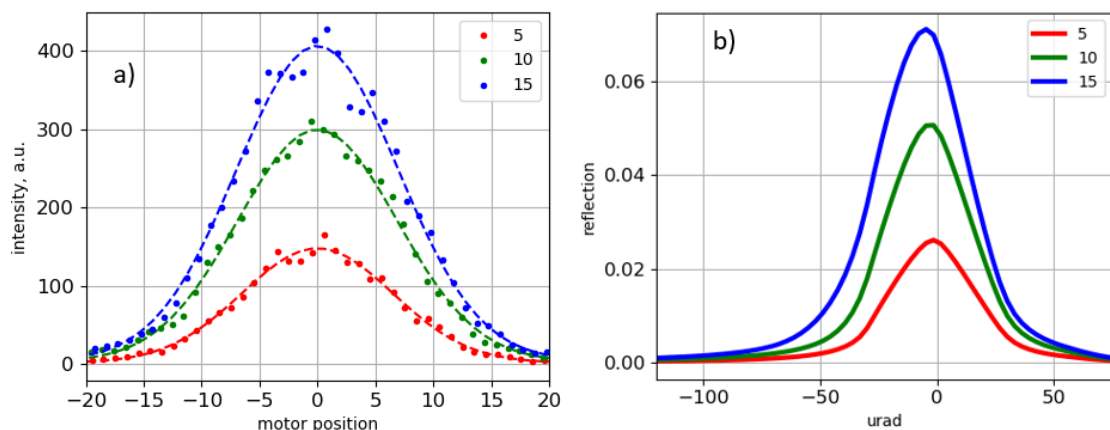
Figure 3.16: Measured (a) and simulated rocking curves (b) for various numbers of pulses in a
train, dashed lines in a) are Gaussian fits of the experimental result. Photon energy was 9 keV,
pulse energy around 0.9 mJ, pulse size around 0.5 mm.

At a later set of measurements, using a more precise piezo-based motor for rocking the second
crystal, one could analyse the measured rocking curve width with a sufficient precision. The
rocking curve measurements and simulations are shown in Fig. 3.16. A several percent rocking
curve widening between 5 and 15 pulses was observed using Gaussian fits, as well as the increase
of rocking curve height between 10 and 15 pulses in train is apparently smaller than the increase
of rocking curve height between 5 and 10 pulses in train. Despite the both tendencies indicative of
first crystal heating, the set of three measurements was not sufficient to make justified statements
on the monochromator performance under intense radiation of MHz-repetition-rate XFEL.

3.5 Future developments of XFEL monochromators

Perfect silicon crystals are widely produced and are therefore easily available. Moreover, the
technology for growing large monocrystallines of silicon with high purity is well developed, which
makes silicon a good material to use as optical elements at XFELs. However, as shown in previous
sections, silicon is prone to significant deformations due to heating under intense high-repetition
rate XFEL radiation. Various techniques to control the temperature of silicon can be used to
stabilize silicon monochromator performance. As presented in previous sections, at EuXFEL the
silicon crystals in monochromator are kept at stable temperatures using combination of liquid
helium active cooling and heating. That way, the crystal that receives the most radiation is

kept at a constant temperature of around ~ 100 K, and the heat induced by impinging pulses is dissipated by cooling. Since the impinging pulses induce heating of the first monochromator crystal, manipulating the second crystal might benefit the monochromator performance. That is, cyclic heating or rotation of the second crystal might improve monochromator transmission due to the shifting of the rocking curve of second crystal, as one can see in Fig. 3.7.

Another way to effectively monochromatize XFEL pulses is to use materials with high thermal conductivity. One of the good candidates is diamond. However, despite well-developed techniques to produce polycrystalline Carbon Vapor Deposition (CVD) diamonds, growing monocrystalline diamonds poses a challenge. At Technological Institute for Superhard and Novel Carbon Materials (TISNCM), high-pressure hihg-temperature (HPHT) technology is used to produce high-purity diamond [57] with the thermal conductivity an order of magnitude higher than silicon. The size of the monocrystalline diamond can be as large as several mm, which is sufficient to operate with pulses at EuXFEL, where the transverse size of unfocused beam is around 1 mm. The exceptional thermal conductivity might enable monochromatization of focused beam. Moreover, compared to silicon, diamond has a long absorption length at hard X-ray wavelengths, which spreads the heat load over crystal volume, which further increases the diamond performance as XFEL pulses monochromator.

It is feasible to create a so-called "channel cut" from a large monocrystalline diamond, such that there will be two crystal surfaces with perfectly parallel scattering planes required for X-ray monochromatization. In all, diamond channel-cut monochromator (DCCM) has a potential to become a good monochromator for intense XFEL pulses arriving at MHz repetition rates.

Diamond, which has longer absorption length and higher heat conductivity compared to silicon, can be used at high intensity and CW XFEL as a hard X-ray monochromator [59]. Using Eq. 2.25 and heat diffusivity in Fig. 3.17 we can estimate the characteristic heat redistribution times. For C(220) at 9 keV photon energy, for instance, $a = 625$ µm, which is on the same order with the typical beamsize of XFEL beams, such that in both depth and radius directions the heat redistribution is similar. Therefore, the one dimensional model used for the heating of silicon cannot be used for the heat flow simulations for the given case of absorption in diamond. If we assume the characteristic lengthscale $L = 500$ µm, the characteristic timescale at 100 K would be $t_{\mathrm{char,L}} = 2.5$ µs, which is on the order of the interval between pulses at MHz repetition rates, such that between pulses the heat dissipates into the volume. At 300 K, however, $t_{\mathrm{char,L}} = 0.26$ ms, which is several orders larger than the interval between pulses. Therefore, despite high heat
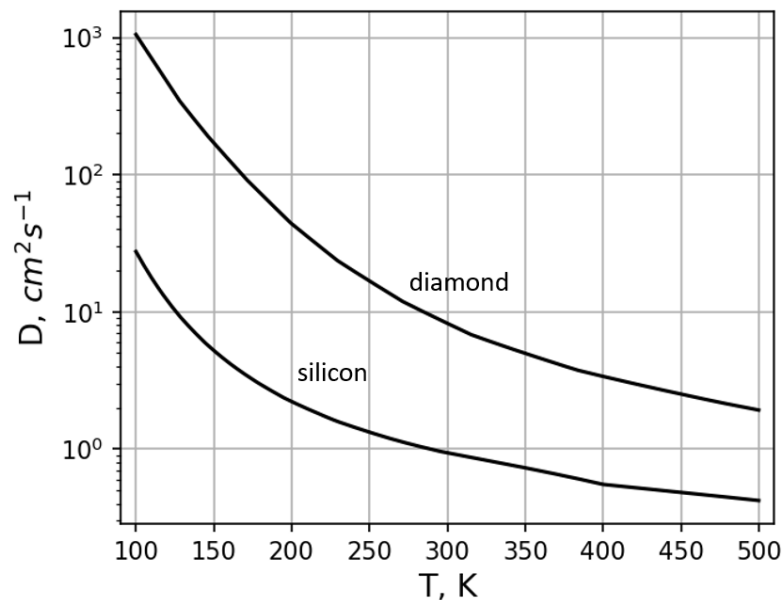
Figure 3.17: Heat diffusivity of naturally occurring diamond and silicon calculated using heat conductivities from [58] and [34], respectively, and specific heat as per Debye's law.

conductivity at room temperature, it is preferred to additionally cool down diamond crystals under intense XFEL radiation.

Diamond heat conductivity data [58] for diamond samples with various purities were collected in 1970's, shown in Fig. 3.18. One can see that the type IIa diamond transfers heat several times more efficient than diamond with nitrogen or boron contamination.

Type IIa diamonds produced by HPHT technology have exceptional purity which leads to high heat conductivity [57] shown in Fig. 3.19. At 200 K, for instance, HPHT diamonds provide the thermal conductivity of $60 \ W/cm \cdot K$, which is about 1.5 times larger than for IIa diamonds in Fig. 3.18. The constant improvement of the purity of type IIa diamonds might enable stable operation of diamond monochromators at high pulse energies and high repetition rates at room temperatures. Under cryogenic cooling, as one can see in Fig. 3.19, type IIa diamond has an order of magnitude larger thermal conductivity compared to IIb type.

In case of X-ray pulses diffraction in mm-thick crystals, heat redistribution happens in both thickness and radius directions between pulses, and one cannot apply the one dimensional model. However, in case of diffraction in thin crystals, where the temperature gradient along thickness direction is small, heat flows only in the direction along surface and one can calculate the heat flow analogous to the algorithm presented in Sec. 2.3. This can, for instance, be used to simulate the heating of diamond crystals used in hard X-ray self seeding.
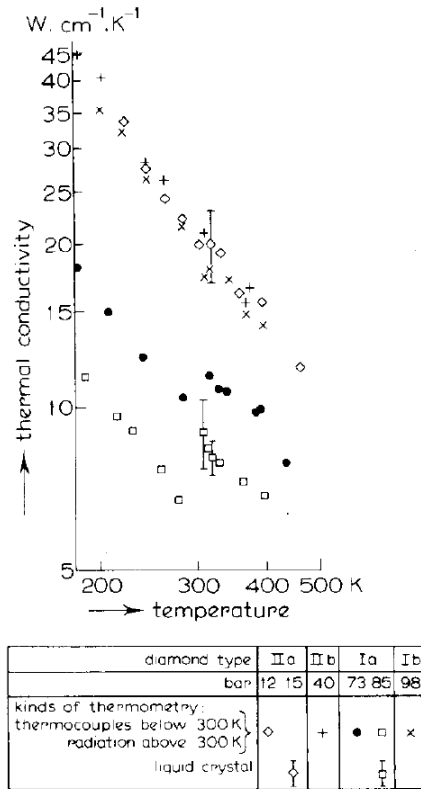
Figure 3.18: Heat conductivity of diamond with various purity [58]. IIa relates to the absence
of significant impurities, IIb diamond contains boron impurities, Ib contains isolated nitrogen
impurities and Ia contains aggregated nitrogen impurities.
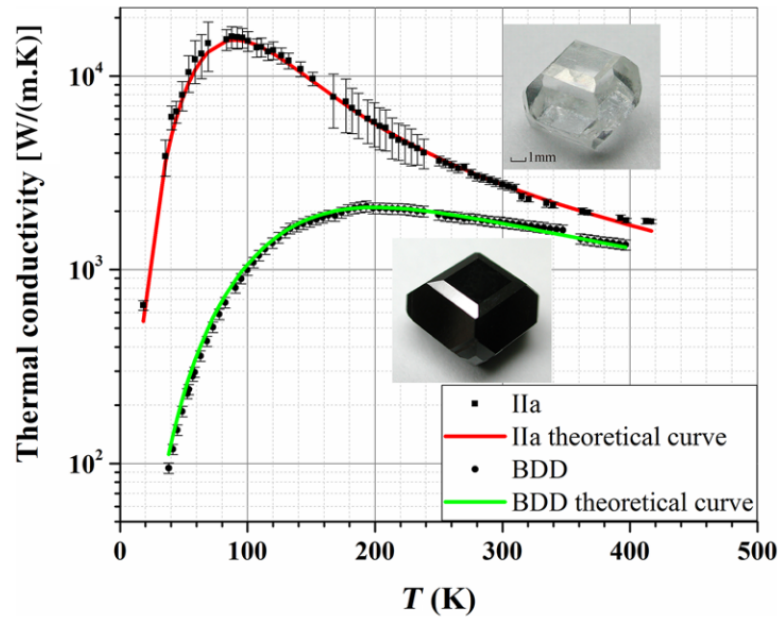
Figure 3.19: Heat conductivity of HPHT type IIa diamond (red line) and type IIb boron-doped
diamond (BDD) (green line) with 20 boron atoms per million atoms of diamond [57]. At 300 K,
for instance, thermal conductivity of IIa diamond is about two times larger than IIb, whereas at
cryogenic temperatures around 100 K the difference is around ten times.

Chapter 4

Strongly bent crystals used for pulse-to-pulse spectral characterization

As shown in Section 3.2, the stochastic nature of SASE leads to random spectra of individual XFEL pulses. Even though the average width of the spectrum and the width of narrow features is defined by the particular settings of a given XFEL, such as electron beam charge, energy and undulator settings, the exact spectrum varies from pulse to pulse. Therefore, by measuring spectra of individual pulses, one can analyze their statistical properties. Strongly bent crystals (bending radii on the order of 10 cm and less) allow to disperse various photon energies of an XFEL pulse into a range of angles that can be recorded with the available detectors at feasible distances. For a C(220) reflection at 9 keV, for instance, photon energies within 10^{-3} bandwidth are dispersed over 0.72 mm area at a distance of 1 m. This dispersion lengthscale is sufficient to capture the SASE bandwidth with detectors that have a spatial resolution of around 10 μm.

Firstly, this section provides an overview of the bent crystal spectrometer implementations and presents the spectrometer at the MID instrument of European XFEL. Previously, diffraction in the finite volume of strongly bent crystals was not considered to affect the recorded spectrum, and the resolution estimations considered the strongly bent crystals as a perfectly reflecting surface. Below, the theory of diffraction in strongly bent crystals is developed, which allows to estimate the intrinsic resolution of bent crystal spectrometer defined by the diffraction in the

crystal volume. The theory is used to estimate the bent crystal spectrometer performance for the typical spectra and crystal parameters used at EuXFEL. At the end, a method to compare the duration of pulses using their spectra is presented.

4.1   Overview of XFEL spectrometer implementations

When inserted directly into the XFEL beam, strongly bent crystals can effectively resolve photon energies of the SASE bandwidth. If a ΔE range of photon energies needs to be resolved, and the average photon energy is E_0, the incidence angles in a range of $\Delta\theta = (\Delta E/E_0)\tan\theta_0$ need to be covered, θ_0 is Bragg angle for E_0. For instance, for $E_0 = 9$ keV and C(220) reflection, $\Delta\theta = 7.2 \cdot 10^{-4}$ is needed to disperse 10 eV bandwidth. We will assume a cylindrically bent crystal, such that over the beam profile X-rays are incident at different angles to the crystal surface. For a crystal bent to the curvature radius $R = 10$ cm, 10 eV bandwidth will be reflected by 7.2 µm of crystal surface, and at detector located at 1 m from the crystal X-rays will be dispersed over 0.72 mm distance. An intensity profile with such length can be resolved by the available imaging devices. The Gotthard detector, for instance, has a pixel size of 50 µm[60], such that 14 pixels will be within the bandwidth. By using scintillator devices, which generate visible light when X-rays are incident on them, it is feasible to record the spectrum with optical devices, since the wavelength of visible light is orders of magnitude shorter than ~ 1 mm-long spot of dispersed photon energies. That way the resolution can be maximized by spreading the spectrum over the field of view of an optical camera. On the other hand, the Gotthard detector allows to measure with 0.5 MHz repetition rate [60], such that the spectra of individual pulses within a train can be measured at EuXFEL.

At EuXFEL, strongly bent monocrystalline diamonds are used [61, 62]. Due to long absorption length and high heat conductivity of diamond, these spectrometers can operate at the high pulse energies and high repetition rates of EuXFEL. Strongly bent silicon crystals that for instance are used at LCLS [63, 64] can only operate at a low power since the heat load induced by intense X-ray pulses would damage the crystals.

HPHT monocrystalline diamonds are mounted in a thick diamond polycrystalline frame with a bender mechanism (see Fig. 4.3) which allows for the heat to dissipate into the frame volume. The triangular shape of the bent crystal allows to minimize the sagittal bending of rectangular plates. In order to achieve maximum transmission through the bent crystal spectrometer, the

beam is precisely aligned within the narrow triangular window where the HPHT crystal is located. A movable slider on the frame allows to vary the bending radius.

Instead of being inserted directly into XFEL beam, strongly bent crystals can also be inserted into the first diffraction order of a grating. That way, only a small fraction of pulse energy impinges the bent crystal. This approach was implemented at SwissFEL [65, 66]. At hard X-ray photon energies, however, the first diffraction order is observed at $\lambda/d_G = 0.1$ nm$/200$ nm $= 0.5$ mrad angle, where $d_G = 200$ nm is a grating period that was used at SwissFEL [65], such that a distance of 10 m is required to have the first diffraction order at 5 mm from the original beam. This lengthscale restrict the applicability of such spectrometers at experiments, whereas a bent diamond spectrometers used at EuXFEL can be used in laboratory conditions since they can be inserted into the direct beam and require distances of around 1 m for a good resolution of XFEL spectra. That way, strongly bent diamond crystals can be installed into the beam at a preferred location, such that spectral changes during X-ray propagation can be studied, e.g. for X-ray absorption spectroscopy studies.
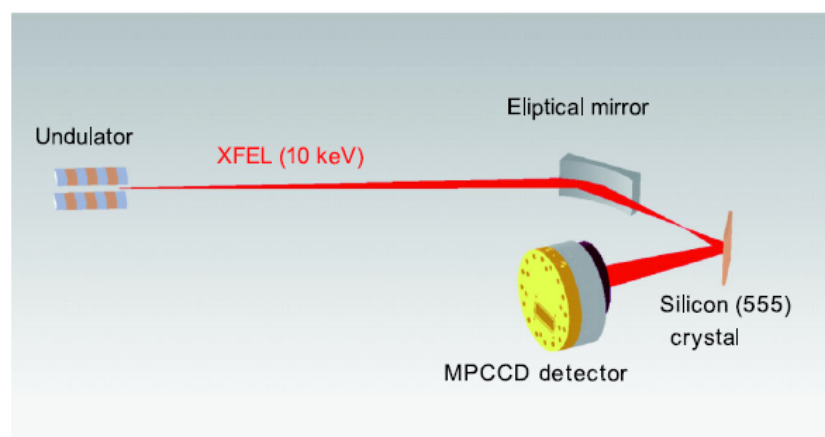
Figure 4.1: The schematics of the spectrometer based on elliptical mirror and flat analyzer crystal [67].

Given that the crystal is thin enough, the transmitted beam can be used after the spectrometers based on strongly bent crystals. In another type of XFEL spectrometer, an elliptical mirror is used to disperse photon energies over angles and a flat analyzer crystal is used to diffract various photon energies at different angles. This method is implemented at SACLA [67]. Such a spectrometer is invasive and does not transmit any X-rays, such that the beam after the spectrometer cannot be used. The schematics of elliptical mirror spectrometer is shown in Fig. 4.1.

The resolution of the spectrometer based on elliptical mirror is defined by the Darwin width of the selected reflection of a flat analyzer crystal which is determined by dynamical diffraction 2.2. The resolution of a strongly bent crystal, however, is defined by the lattice spacing of the selected reflection and the crystal thickness, as shown in Sec. 4.3.3, such that a bent crystal spectrometer potentially can provide better resolution than a flat analyzer crystal and elliptical mirror. Moreover, due to the variable and small bending radius, one can achieve dispersion of photon energies over a larger angular range.

4.2   Bent crystal spectrometer as a part of Diagnostics End Station at MID instrument of EuXFEL

At the MID instrument, a bent crystal spectrometer is a part of the Diagnostics Endstation (DES). The device is designed to be equipped with bent crystals, as shown in Fig. 4.2. The chamber where the crystals are installed is a part of the high vacuum environment of the beamline. The X-rays that are diffracted from bent crystal exit the chamber through a kapton window. To reduce scattering and absorption in air between the crystal and the detector, an evacuated flight tube of around 1 m length is installed on vertical rail system together with the Gotthard detector allowing adjustment of the scattering angle.

An yttrium aluminium garnet (YAG) imager device behind the bent crystal is used for the beam alignment

The resolution of the device is estimated for the typical experimental parameters below in Sec. 4.4.

4.3   X-ray diffraction in strongly bent crystals and applicability of kinematical theory

This section provides an overview of the method to simulate the diffraction of XFEL pulses in strongly bent crystals [68, 69]. The model of dispersion of different photon energies over different angles is developed within the framework of kinematical diffraction. The criterion for the applicability of kinematical theory is introduced. The evolution of the intensity distribution in space is simulated using Fresnel and Fraunhofer limits of diffraction at short and long distances from the crystal, respectively. It is shown that the resolution of a strongly bent crystal spectrometer at
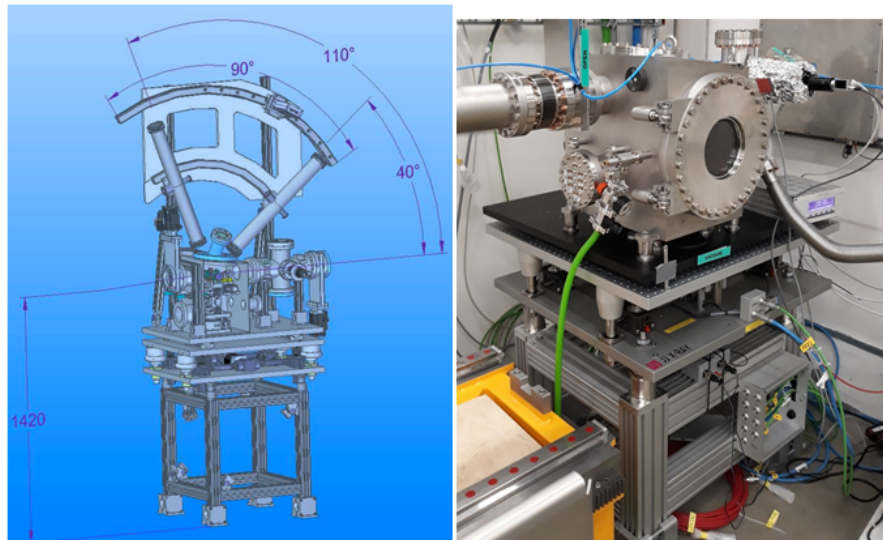
Figure 4.2: Diagnostics Endstation at MID instrument: schematics (left) [16] and current installation (right).
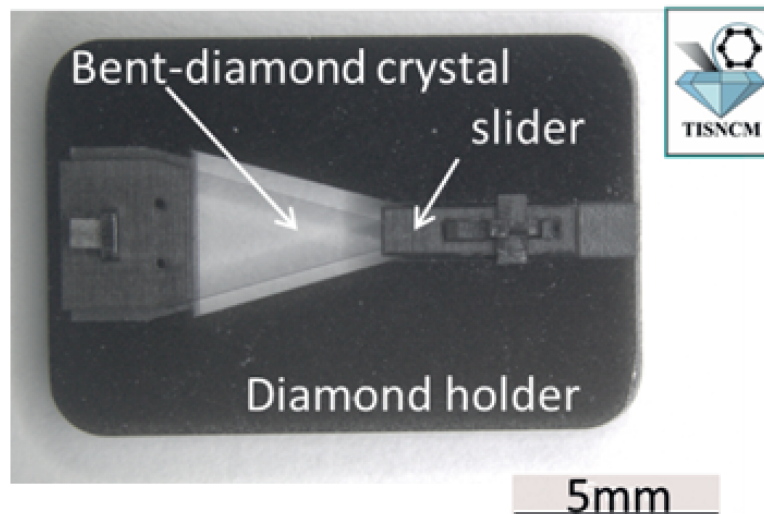
Figure 4.3: HPHT diamond device used at DES of MID instrument [62].

a given reflection is intrinsically defined by the ratio of lattice spacing and the crystal thickness.

4.3.1 Time-integrated diffraction intensity

We assume full transverse coherence of the incident XFEL pulse and take into consideration only its time structure. This assumption holds for the SASE pulses, in particular at EuXFEL where the transverse coherence can be as high as 95%[70]. The electric field of the pulse can be written

using its frequency spectrum:

$$E^{\text{in}}(\mathbf{r}, t) = \int\limits_{-\infty}^{\infty} \tilde{E}^{\text{in}}(\omega) e^{ik\mathbf{s}_0 \cdot \mathbf{r} - i\omega t} \, d\omega. \tag{4.1}$$

Here ω is the frequency of a plane-wave component, $k = \omega/c$ is its wavevector, c is the speed of light, and $\mathbf{s}_0$ is the unit vector in the direction of the wave propagation.

The wave packet (4.1) is incident on a bent-crystal spectrometer. We consider its diffraction on a bent crystal in the kinematical (first Born) approximation which is justified because of strong deformation gradient that does not allow for dynamical effects, as explained in Sec. 4.3.2. We follow the description of the first Born approximation by [71], Sec. 13.1.2, but restore the time exponent $\exp(-i\omega t)$. This is usually omitted since a monochromatic wave is considered in conventional scattering theory. In our case, a continuous spectrum is considered, hence we need to consider all frequencies separately and integrate over frequencies ω. The amplitude of the scattered wave is

$$E^{\text{out}}(\mathbf{r}, t) = \int\limits_{-\infty}^{\infty} d\omega \int_V d\mathbf{r}' \, \tilde{E}^{\text{in}}(\omega) e^{ik\mathbf{s}_0 \cdot \mathbf{r}' - i\omega t} \chi(\mathbf{r}') \frac{e^{ik|\mathbf{r} - \mathbf{r}'|}}{|\mathbf{r} - \mathbf{r}'|}, \tag{4.2}$$

where $\chi(\mathbf{r})$ is the crystal susceptibility and the spatial integration is performed over the volume V of the scattering volume.

In the Fraunhofer limit $r \gg r'$

$$|\mathbf{r} - \mathbf{r}'| \approx r - \mathbf{s} \cdot \mathbf{r}', \tag{4.3}$$

where $\mathbf{s}$ is the unit vector in the direction to the detector, $\mathbf{r} = r\mathbf{s}$. Using Eq. (4.3), the scattered wave (4.2) can be represented as

$$E^{\text{out}}(r\mathbf{s}, t) = \frac{1}{r} \int\limits_{-\infty}^{\infty} \tilde{E}^{\text{in}}(\omega) e^{ikr - i\omega t} f_1(\mathbf{s}, \mathbf{s}_0; k) \, d\omega, \tag{4.4}$$

where the scattering amplitude in the first Born approximation is

$$f_1(\mathbf{s}, \mathbf{s}_0; k) = \int_V \chi(\mathbf{r}') e^{-ik(\mathbf{s} - \mathbf{s}_0) \cdot \mathbf{r}'} \, d\mathbf{r}'. \tag{4.5}$$

Here the dependence of the scattering amplitude f_1 on the length of the wavevector k is explicitly noted. The crystal susceptibility for X-rays $\chi(\mathbf{r})$ is not averaged over the physically infinitely small volumes but possesses the crystal lattice periodicity [see, e.g., [72], §124].

In order to calculate the intensity of the electric field Eq. 4.4 at an instant t, one needs to integrate over the frequencies using complex conjugation of electric fields:

$$
\begin{aligned}
I(r\mathbf{s}, t) &= E^{\text{out}}(r\mathbf{s}, t) \cdot E^{\text{out}*}(r\mathbf{s}, t) \\
&= \frac{1}{r^2} \iint_{-\infty}^{\infty} d\omega_1 d\omega_2 \, e^{i(\omega_2 - \omega_1)t} e^{i(k_1 r - k_2 r)} \\
&\quad \times \tilde{E}^{\text{in}}(\omega_1) \tilde{E}^{\text{in}*}(\omega_2) f_1(\mathbf{s}, \mathbf{s}_0; k_1) f_1^*(\mathbf{s}, \mathbf{s}_0; k_2),
\end{aligned}
\tag{4.6}
$$

where the asterisk denotes the complex conjugate and $k_n = \omega_n/c$ are the wavevectors of waves with frequencies ω_n.

In order to calculate the intensity measured by a detector. we need to integrate Eq. 4.7 over a detector exposure period τ_{det}:

$$
\mathcal{I}^{\text{det}}(r\mathbf{s}) = \iint_{-\infty}^{\infty} d\omega_1 d\omega_2 ... \int_0^{\tau_{\text{det}}} \exp(i(\omega_2 - \omega_1)t) \, dt.
\tag{4.7}
$$

After the integration Eq. 4.7 would be

$$
\mathcal{I}^{\text{det}}(r\mathbf{s}) = \iint_{-\infty}^{\infty} d\omega_1 d\omega_2 ... \frac{2\sin(\tau_{\text{det}}(\omega_1 - \omega_2)/2)}{\tau_{\text{det}}(\omega_1 - \omega_2)}.
\tag{4.8}
$$

At XFELs, pulse duration is by design $\sim 10 - 100$ fs, whereas the detectors used for example at EuXFEL have exposure periods on the order of 100 ns. Therefore, since the detector exposure time is larger than pulse duration by many orders, we can assume infinite integration range in Eq. 4.7 and use

$$
\mathcal{I}(r\mathbf{s}) = \int_{-\infty}^{\infty} I(r\mathbf{s}, t) \, dt
\tag{4.9}
$$

to calculate the intensity at detector. Integration over a mathematically infinite range will change Eq. 4.7 to

$$
\mathcal{I}^{\text{det}}(r\mathbf{s}) = \iint_{-\infty}^{\infty} d\omega_1 d\omega_2 ... \delta(\omega_1 - \omega_2),
\tag{4.10}
$$

which means that only in case of $\omega_1 = \omega_2$ there will be contribution to the scattering intensity. The delta function under the integral means that in practice we can neglect the interference of waves with different frequencies, since for the detector integration periods much longer than pulse duration we can consider the infinite τ_{det} in Eq. 4.8.

In view of the different timescales of detector exposure and pulse duration, such that we can treat exposure time as infinite, and in view of Eq. 4.10 we can write Eq. 4.7 as

$$\mathcal{I}(r\mathbf{s}) = \frac{2\pi}{r^2} \int_{-\infty}^{\infty} |f_1(\mathbf{s}, \mathbf{s}_0; k)|^2 \left|\tilde{E}^{\mathrm{in}}(\omega)\right|^2 d\omega. \tag{4.11}$$

That is, when X-rays of different wavelengths arrive at one point, the measured intensity will be a sum of intensities of waves [73].

The squared scattering amplitude $|f_1(\mathbf{s}, \mathbf{s}_0; k)|^2$ in Eq. (4.11) denotes the scattering amplitude of the same wavelength incident at the same angle and reflecting in different directions. One can consider these different scattering angles as if they correspond to various frequencies ω' whose Bragg condition is at that reflection angle. In this way one can treat the X-rays scattered in different directions as a measured spectrum over frequencies ω'.

We can rewrite Eq. (4.11) as

$$\mathcal{J}(\omega') = \int_{-\infty}^{\infty} \mathcal{R}(\omega', \omega) \left|\tilde{E}^{\mathrm{in}}(\omega)\right|^2 d\omega, \tag{4.12}$$

where $\mathcal{J}(\omega')$ is the intensity (4.11) after the change of variables from θ to ω'. One can see that if the resolution is ideal, i.e., $\mathcal{R}(\omega', \omega)$ is $\delta(\omega - \omega')$, the measured spectrum over frequencies ω' coincides with the incident spectrum. Below we develop a theoretical framework to simulate the resolution $\mathcal{R}(\omega', \omega)$ of a bent-crystal spectrometer.

4.3.2 Applicability of kinematical theory

According to the equation of dynamical diffraction Eq.2.16, as long as the lattice deformation is within the Darwin width in Eq. 2.17, i.e. as long as $|\eta| < 1$ in Eq. 2.5, the dynamical diffraction is strong and intensity of diffracted wave is high. The Darwin width in Eq. 2.17 corresponds to the range of angles

$$\Delta\theta_B = \frac{2|\chi_h|}{\sin 2\theta_B} \tag{4.13}$$

in which dynamical diffraction takes place for the same photon energy.

If we have a cylindrically bent crystal with curvature radius R, the gradient of distortions along surface is $1/R$, as shown below in Eq. 4.20. That way, over the extinction length Λ the lattice distortion changes by $\Lambda \cdot (1/R) = \Lambda/R$. If this deformation is larger than the Darwin

width, such that $|\eta| > 1$ in Eq. 2.5, the dynamical diffraction conditions are not satisfied. This means that the deformation gradient is too steep for the re-scattering of X-rays to be significant, and the diffraction can be treated as kinematical.

For bending radii larger than

$$R_c = \frac{\Lambda \sin 2\theta_B}{2|\chi_h|} \tag{4.14}$$

the deformation changes slow enough along the surface such that over extinction length Λ the diffraction condition $|\eta| < 1$ holds.

4.3.3 Resolution of a bent-crystal spectrometer. Fraunhofer diffraction

As in any material, the susceptibility $\chi(\mathbf{r})$ is defined by the local properties. In particular, for hard X-rays the distance between atoms is on the order of wavelengths, and the susceptibility depends on the coordinate within the crystal volume. In a periodic lattice of a crystal, since atoms are located in a regular manner, one can calculate Fourier-components of the susceptibility as

$$\chi_{\mathbf{Q}} = V^{-1} \int_V \chi(\mathbf{r}) \exp(i\mathbf{Q}\mathbf{r}) d^3\mathbf{r} \tag{4.15}$$

which is non-zero for each reciprocal lattice vector $\mathbf{Q}$.

The scattering amplitude (4.5) for an ideal crystal is governed by the Fourier component $\chi_{\mathbf{Q}} \exp(i\mathbf{Q} \cdot \mathbf{r})$ of the susceptibility $\chi(\mathbf{r})$ for the actual reciprocal lattice vector $\mathbf{Q}$. The displacement field $\mathbf{u}(\mathbf{r})$ due to the bending causes a change of the susceptibility according to the change of the positions of the atoms to $\chi(\mathbf{r} - \mathbf{u}(\mathbf{r}))$ and the respective change of its Fourier component to $\chi_{\mathbf{Q}} \exp(i\mathbf{Q} \cdot \mathbf{r} - i\mathbf{Q} \cdot \mathbf{u}(\mathbf{r}))$. We consider atom displacements to be much smaller than the lattice spacing of a chosen reflections.

The kinematical diffraction amplitude (4.5) can be written as an integral over the scattering plane of the crystal

$$f_1 = \int_{-\infty}^{\infty} dx \int_{-D/2}^{D/2} dz \, \exp(iq_x x + iq_z z - i\mathbf{Q} \cdot \mathbf{u}), \tag{4.16}$$

where D is the thickness of the crystal plate and $\mathbf{q} = k\mathbf{s} - k\mathbf{s}_0 - \mathbf{Q}$. Here the scattering plane is the xz plane with the x axis tangent to the surface of the bent crystal at $x = 0$ and the z
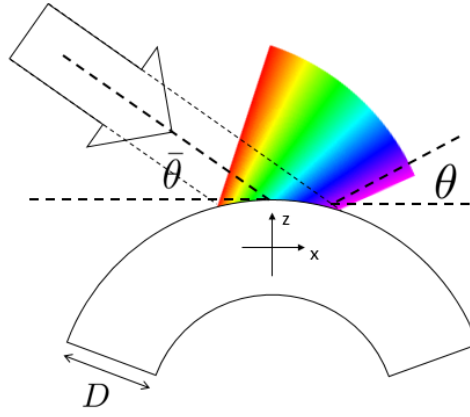
Figure 4.4: The geometry of the bent crystal calculations.

axis along the inner surface normal. The origin is in the middle plane of the crystal plate. The scheme of coordinates is shown in Fig. 4.4. X-rays of different frequencies incident at an angle $\bar{\theta}$ are scattered at different angles θ. Let us calculate the components of the scattering vector $\mathbf{q}$ in this frame.

An X-ray pulse consists of plane waves of different frequencies incident onto the crystal at the same angle $\bar{\theta}$ with respect to x axis. The angle $\bar{\theta}$ is the Bragg angle for some reference frequency $\bar{\omega}$ with the wavevector $\bar{k} = \bar{\omega}/c$. The Bragg law for this frequency reads $d\sin\bar{\theta} = \pi/\bar{k}$, where $d = 2\pi/Q$ is the lattice spacing of the chosen reflection. The x- and z-components of the reciprocal lattice vector in the chosen coordinate system are $\mathbf{Q} = \left(0, -2\bar{k}\sin\bar{\theta}\right)$.

The wavevector of the incident wave with any other frequency ω in the pulse possesses the same incidence angle $\bar{\theta}$ but another wavevector k, so that

$$k\mathbf{s}_0 = k\left(\cos\bar{\theta}, \sin\bar{\theta}\right). \qquad (4.17)$$

The diffracted intensity is measured as a function of the angle θ between the x axis and the vector $\mathbf{s}$. Hence, the wavevector of the diffracted wave is

$$k\mathbf{s} = k\left(\cos\theta, -\sin\theta\right). \qquad (4.18)$$

As mentioned in the previous section, it is convenient to consider the scattering angle $\bar{\theta}+\theta$ as twice the Bragg angle of a wave with the frequency ω' defined by this condition. The Bragg law

reads $d \sin \left[\left(\bar{\theta} + \theta \right) / 2 \right] = \pi / k'$, where $k' = \omega'/c$ is the respective wavevector. A straightforward calculation of the components of the vector $\mathbf{q} = k\mathbf{s} - k\mathbf{s}_0 - \mathbf{Q}$ gives [see also Appendix B by [68]]

$$q_x = \frac{2\pi}{d} \frac{\omega' - \bar{\omega}}{\bar{\omega}} \tan \bar{\theta}, \quad q_z = \frac{2\pi}{d} \frac{\omega' - \omega}{\bar{\omega}}. \tag{4.19}$$

For symmetric Bragg reflections considered in the present work, $\mathbf{Q} \cdot \mathbf{u} = -Qu_z$, so that only u_z component of the displacement field is of interest. For a crystal cylindrically bent to a radius R, it is [68]

$$u_z = (x^2 + \alpha z^2)/2R. \tag{4.20}$$

To achieve the cylindrical bending of a rectangular plate, the bending momenta have to be applied to the perpendicular edges of the plate. The same bending state can be approached by applying a momentum to the apex of a triangle-shaped plate [74].

The parameter α in Eq. (4.20) depends on the anisotropic elastic constants of the crystal. Particularly, for a 110 oriented diamond plate, $\alpha = 0.02$, while for a silicon plate of the same orientation $\alpha = 0.18$ [68]. For 111 oriented plates, the respective values are $\alpha = 0.047$ for diamond and $\alpha = 0.22$ for silicon [68]. In such a geometry, diamond happens to be susceptible to shear stress caused by bending. In particular, for the direction (110) of diamond, the shear component of the compliance tensor $s_{44} = 0.173 \cdot 10^{-5}$ MPa^{-1} is larger than the plane component $s_{11} = 0.01 \cdot 10^{-5}$ MPa^{-1} [75]. This combination of elastic parameters leads to the weak deformation along thickness of diamond in the selected direction.

Let us compare the deformation in Eq. 4.20 for silicon with (111) surface orientation and diamond with (110) surface orientation. Fig. 4.5 shows the displacement u_z in x-z plane for these two cases. One can see that in diamond the deformation changes in z-direction much slower than in silicon. Therefore, in diamond the depth dependence of displacement will be much smaller than in silicon.

The term $\exp(-iQx^2/2R)$ in the integral in Eq. 4.16 that results from multiplying $\mathbf{Q}$ and Eq. 4.20 due to the displacement field of a bent crystal gives rise to an x range relevant to diffraction of the order of $\sqrt{Rd}$. For instance, for $R = 10$ cm and $d = 1$ Å, the diffraction will happen over the lengthscale of ~ 10 μm. At XFELs, crystals of ~ 10 μm-thick crystals are used since they can be bent to the radii required for effective dispersion of SASE spectra. That is, if we have ~ 1 mm-wide pulse, only a tiny μm-long volume of the bent crystal will contribute to the scattering, whereas the rest of the pulse will not be affected by diffraction.
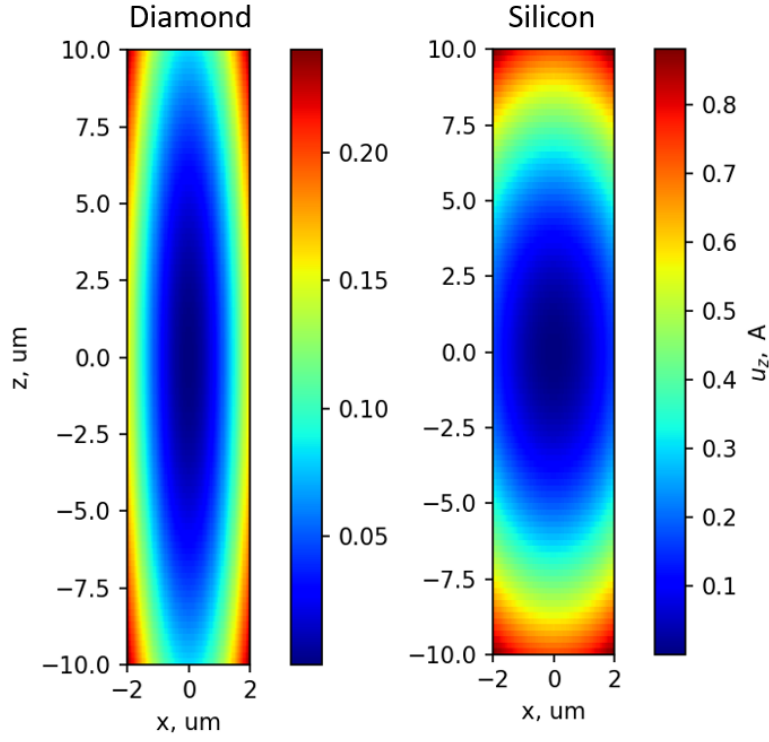
Figure 4.5: The displacement $u_z = (x^2 + \alpha z^2)/2R$ of a cylindrically bent 20 µm-thick silicon crystal with (111) surface orientation and diamond crystal with (110) surface orientation, bending radius 12.5 cm. x coordinate is shown within 4 µm range to illustrate the difference of deformation along z direction.

The integration over x in Eq. (4.16) can be performed in infinite limits. This integration results in a phase factor which drops out when calculating $|f_1|^2$. In the remaining integral over z, we proceed to a dimensionless variable $\xi = 2z/D$. Then, after reassigning $q_{x,z}$ to ω and ω' as in Eq. 4.19, the integral (4.16) gives

$$\mathcal{R}(\omega' - \omega) = \left| \int_{-1}^{1} \exp(ig\xi - ib\xi^2) \, d\xi \right|^2 , \qquad (4.21)$$

where

$$b = \frac{\pi}{4} \frac{\alpha D^2}{Rd}, \quad g = \pi \frac{D}{d} \frac{\omega' - \omega}{\bar{\omega}}. \qquad (4.22)$$

When the wave field is calculated at distances larger than the scattering volume at Bragg's angle, only the q_z component of scattering vector in Eq. (4.19) is relevant. The resolution function in Eq. (4.12) depends on the difference $\omega' - \omega$, so that we write it as $R(\omega' - \omega)$.

Before calculating the integral (4.21), let us discuss its properties qualitatively. As long as

the parameter b is smaller than g, the second term in the exponent in Eq. (4.21) can be neglected since when $\xi < 1$ we have $\xi^2 < \xi$. We write hereafter $|b|$, where this is relevant, since the radius R can be positive for a convex crystal bending or negative for a concave bending.

The resolution can be quantified by using the Rayleigh criterion, formulated for spectral lines with the shapes described by the function $\mathrm{sinc}^2 g$ (see [71], Sec. 7.6.3). Rayleigh proposed that two components of the same intensity are just resolved, when the principal intensity maximum of one coincides with the first intensity minimum of the other, i.e. $\mathrm{sinc}^2 g = 0$. Since $\sin(g) = 0$ for $g = \pi$, the resolution is

$$\Delta E/E = |\omega' - \omega|/\bar{\omega} = d/D. \tag{4.23}$$

Hence, provided $|b|$ is smaller than $|g|$, the relative resolution $\Delta E/E$ does not depend on the X-ray energy and on the bending radius and is equal to the ratio of the lattice spacing of the chosen reflection to the thickness of the bent crystal. We see that for a given lattice spacing d, with the increasing thickness D, on the one hand, the resolution in Eq. 4.23 increases, and on the other hand the quadratic term under the exponent in Eq. 4.21 depending on b in Eq. 4.22 increases, what leads to worse resolution. In Sec. 4.4 it is demonstrated how despite Eq. 4.23 an increasing thickness can worsen the resolution.

The integral (4.21) can be calculated and expressed analytically through cosine and sine Fresnel integrals $C(x)$ and $S(x)$ as

$$\mathcal{R}(\omega' - \omega) = \left| F\left(\frac{g + 2b}{\sqrt{2\pi|b|}}\right) - F\left(\frac{g - 2b}{\sqrt{2\pi|b|}}\right) \right|^2, \tag{4.24}$$

where $F(x) = C(x) + iS(x)$.

4.3.4 Effect of finite distance propagation. Fresnel diffraction

This section is devoted to evaluating the effect of a finite distance between the bent-crystal spectrometer and the detector. The finite distance to a detector is accounted by the following term in the expansion (4.3):

$$|\mathbf{r} - \mathbf{r}'| \approx r - \mathbf{s} \cdot \mathbf{r}' + \frac{[\mathbf{r}' - (\mathbf{r}' \cdot \mathbf{s})\mathbf{s}]^2}{2r}. \tag{4.25}$$

Substituting here $\mathbf{r}' = (x, z)$ and $\mathbf{s} = (\cos\theta, -\sin\theta)$ in the coordinates of Fig. 4.4, we find that Eq. (4.16) acquires an additional phase term $\exp[ik(x\sin\theta + z\cos\theta)^2/2L]$ in the integral. Hereafter the spectrometer-detector distance is denoted by L instead of r to decouple the distance to detector from the general notation of the vector of a point in space. The wavevector k and the angle θ between the x-axis in Fig. 4.4 and a scattered X-ray can be replaced in this term by the reference values $\bar{k}$ and $\bar{\theta}$, since the difference of optical path of various frequencies propagating at different angles will be negligible compared to the propagation over the distance L. We will not consider the signal at μm distances from the bent crystal since at experiment one locates the detector at around a meter to achieve sufficient dispersion over angles.

The additional phase factor $\exp[ik(x\sin\theta + z\cos\theta)^2/2L]$ that corresponds to finite distance propagation will lead to the following modification of the integral (4.16) [68]:

$$\mathcal{R}(\omega', \omega) = \left| \int_{-1}^{1} \exp(i\tilde{g}\xi - i\tilde{b}\xi^2)\, d\xi \right|^2 , \tag{4.26}$$

where

$$\tilde{R} = R\left(1 + \frac{R\sin\bar{\theta}}{2L}\right)^{-1} , \tag{4.27}$$

$$\tilde{\alpha} = \alpha + \frac{\tilde{R}\cos^2\bar{\theta}}{2L\sin\bar{\theta}} , \tag{4.28}$$

$$\tilde{b} = \frac{\pi}{4}\frac{\tilde{\alpha}D^2}{Rd} , \tag{4.29}$$

$$\tilde{g} = \pi\frac{D}{d}\left(1 + \frac{R\sin\bar{\theta}}{2L}\right)^{-1}\left[\frac{\omega' - \omega}{\bar{\omega}} - \frac{R\sin\bar{\theta}}{2L}\frac{\omega - \bar{\omega}}{\bar{\omega}}\right] . \tag{4.30}$$

Calculation of the integral (4.26) is the same as in Eq. (4.24) above,

$$\mathcal{R}(\omega', \omega) = \left| F\left(\frac{\tilde{g} + 2\tilde{b}}{\sqrt{2\pi|\tilde{b}|}}\right) - F\left(\frac{\tilde{g} - 2\tilde{b}}{\sqrt{2\pi|\tilde{b}|}}\right) \right|^2 . \tag{4.31}$$

The resolution function in Eq. (4.31) depends on ω and ω', rather than the difference $\omega - \omega'$ in Eq. (4.24), since $\tilde{g}$ depends on both $\omega' - \omega$ and $\omega - \bar{\omega}$. As a result, the detected spectrum is stretched or squeezed, depending on the sign of the bending. This is discussed below.

Similarly to the Fraunhofer diffraction case described in the previous section, a maximum resolution is reached as long as $\left|\tilde{b}\right|$ is small. If this condition is satisfied, the resolution according

to the Rayleigh criterion, that follows from Eq. (4.30), is

$$\frac{\Delta E}{E} = \frac{d}{D}\left(1 + \frac{R\sin\bar\theta}{2L}\right).$$

(4.32)

If $R > 0$, in the case of the convex bending shown in Fig. 4.4, the resolution becomes worse compared to the Fraunhofer diffraction. Oppositely, for a concave bending $R < 0$, the resolution is better than in the case of Fraunhofer diffraction. The correction can be notable when the bending radius R and the distance to a detector L are comparable, as it is in some experiments discussed in the next section. However, usually $R \ll L$, since typical bending radii of several tens of cm is usually smaller than the distances required for sufficient resolution of detectors. We take into account this correction in the numerical calculations below but do not discuss it further.

The parameter $\tilde b$ in Eq. (4.29) can be rewritten as

$$\tilde b = b + \frac{D^2\cos^2\bar\theta}{\lambda L}\left(1 + \frac{R\sin\bar\theta}{2L}\right)^{-1},$$

(4.33)

where λ is the wavelength and the Bragg law $2d\sin\bar\theta = \lambda$ is used. The Fraunhofer diffraction condition is met when $\tilde b \approx b$. This is the case when, firstly, $L \gg R\sin\bar\theta$, such that the term in brackets in Eq. 4.33 is close to unity. Secondly, $\sqrt{\lambda L}$ needs to be larger than $D\cos\bar\theta$, which physically means that the radius of the first Fresnel zone at a distance L needs to exceed the crystal thickness seen from the direction of the diffracted beam. Therefore, at distances larger than

$$L_{\mathrm{Fr}} = \frac{D^2\cos^2\bar\theta}{\lambda}$$

(4.34)

the resolution can be treated as in Fraunhofer limit and does not increase during further propagation in free space.

4.4 Theoretical resolution estimation of bent crystal spectrometers

The stochastic SASE process leads to a fluctuating spectrum which hence needs to be measured for each pulse. In particular, the bandwidth of SASE provides a figure of merit for the temporal

coherence, whereas the width of individual peaks in the spectrum provides the estimate of the pulse duration. Bent crystal allows to effectively disperse the X-rays of different energy over angles. However, since the diffraction of hard X-rays in crystals takes place in the crystal volume, the resolution is affected by the crystal properties and the deformations of the crystal lattice. In the previous section it was shown that since the X-rays undergo diffraction in the volume of a bent crystal, the resolution of the spectrometer is defined by various parameters of the crystal. In this section, the theoretical model developed in the previous chapter is used to numerically simulate the resolution of various crystals used at EuXFEL.
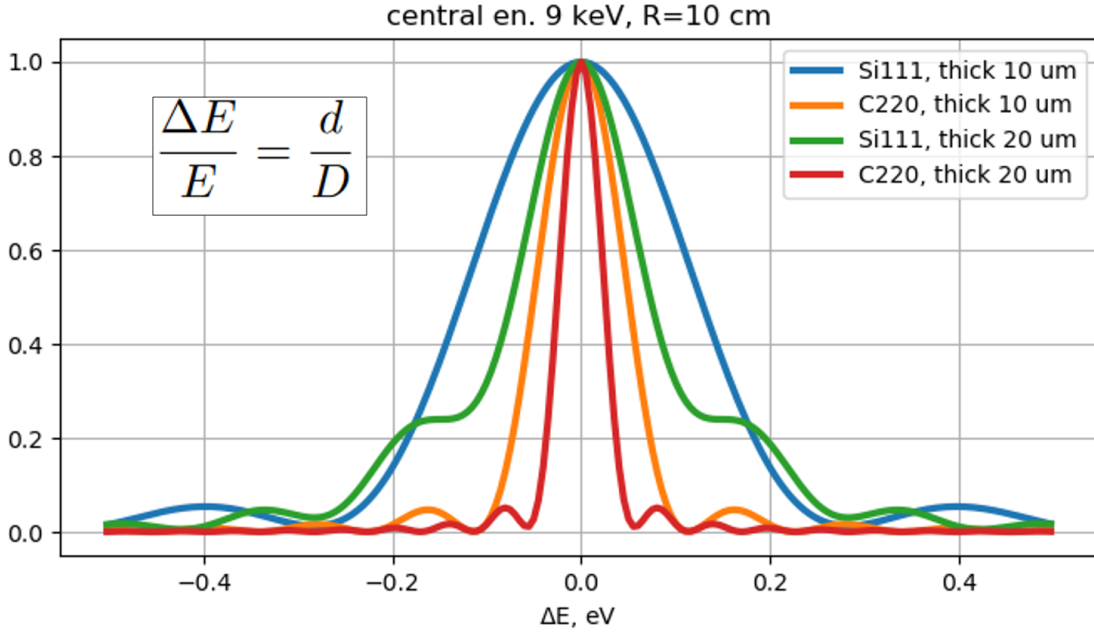
Figure 4.6: Reflection intensity $|R(\omega - \omega')|^2$ for Fraunhofer limit calculated with Eq. 4.24 normalized to the maximum value, $\Delta E = \hbar(\omega - \omega')$, $\hbar$ is Planck constant. C(220) has a lattice spacing $d_{C220} = 1.26$ Åsmaller than the lattice spacing of Si(111) $d_{Si111} = 3.14$ Å, which leads to a narrower peak for C(220) compared to the Si(111) reflection for the same thickness. Two-fold increase of crystal thickness leads to a twice better resolution, as calculated in Sec. 4.3.3. The width of the resolution peak follows the condition in Eq. 4.23 shown in the inset.

Fig. 4.6 shows the effect the thickness and lattice spacing have on the resolution. Here, the resolution of a single wavelength is demonstrated. i.e. the distribution that would be recorded by the detector if the pulse had δ-function spectrum, i.e. consisting of a single wavelength. One can see that the recorded spectrum has a certain non-zero width, i.e. the delta-function properties are not preserved. In case of a larger thickness, the resolution curve is narrower. On the other hand, an increasing thickness leads to a larger $|b|$, which leads to an increasing quadratic term in Eq. 4.21 and thus to the rising tails of Si(111) and 20 µm thickness. Below, it is shown how

83

an increasing thickness can lead to a wider reflection curve and worse resolution.
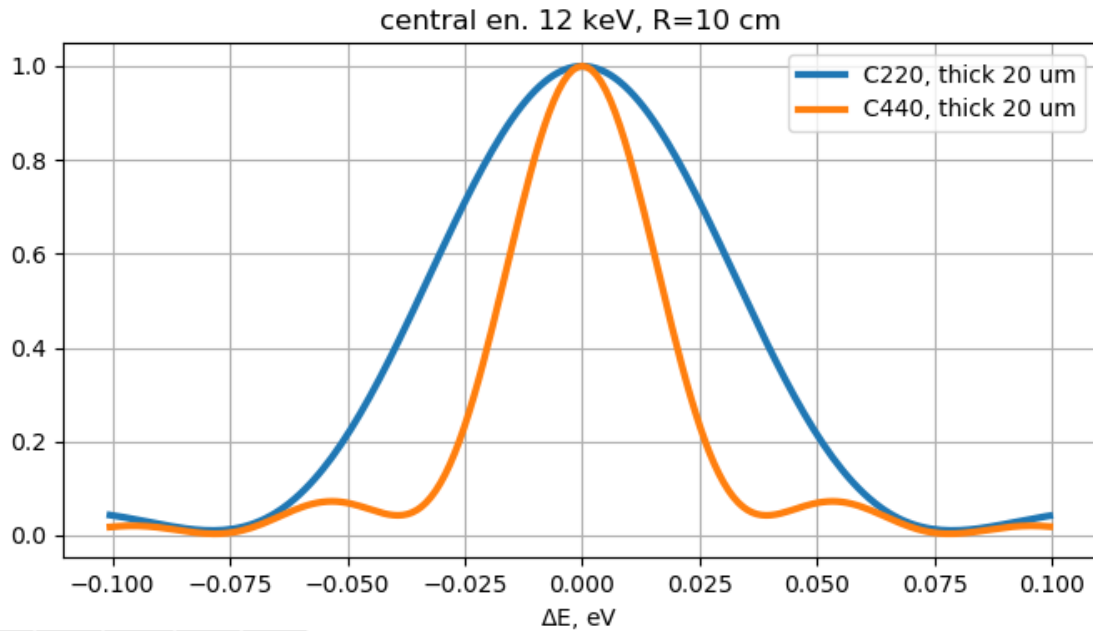
Figure 4.7: Delta-peak resolution of C(220) and C(440) at 12.4 keV. Crystal thickness 20 µm.

Let us demonstrate how the above mentioned effects influence the measured spectra of XFEL pulses. Fig. 4.7 demonstrates the resolution of a single wavelength of two reflections whose lattice spacings differ by a factor of two. Using Eq. 4.12 we can simulate the signal at the detector for a SASE spectrum.

Fig. 4.8 shows how the resolution in Fig. 4.7 affects the measured spectrum. The figure shows a portion of a sample SASE pulse generated using a database based on [49]. The simulated pulse spectrum is generated for 500 pC bunch charge, 14 GeV electron energy and linear gain regime of SASE. This results in a peak width of around 0.05 eV, which is closer to the resolution of C(440) than of C(220) in Fig. 4.7.

Therefore, due to its poorer resolution, C(220) reflection is unable to resolve the finest features of the spectrum as well as the C(440) reflection. However, even for the narrower resolution, some of fine features are not resolved properly.

In order to demonstrate the nature of the fine features in the spectrum let us look at spectra of pulses whose temporal structure consists of various numbers of peak. Even in the idealized case of Gaussian peaks shown in Fig. 4.9, when there are more than two peaks, secondary narrow spectral peaks are present. This can be explained by an increasing pulse duration which leads to the narrower spectral peaks. In reality, SASE is a stochastic process that leads to a more

Figure 4.8: Resolution of a theoretical SASE spectrum: dashed red line - original spectrum $|\tilde{E}^{\mathrm{in}}(\omega)|^2$, solid lines - resolved spectra $\mathcal{J}(\omega')$ from Eq. 4.12 using two different reflections. Spectrum is calculated using FAST algorithm [49] and acquired with the FAST-XPD database [40], $|R(\omega - \omega')|$ is calculated in the Fraunhofer limit using Eq. 4.24.
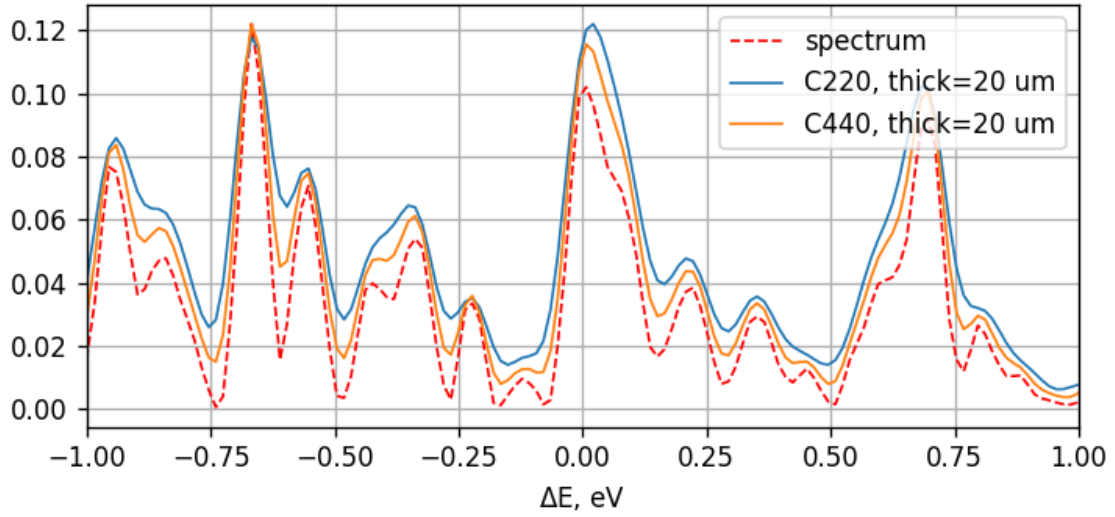
complicated time structure, e.g. as shown in Fig. 3.3. For any pulse, however, the width of the spectral peaks is inversely proportional to the duration of a pulse. Therefore the narrowest peaks in the spectrum carry information about the length of the pulse in time, and resolving such finest features is crucial for restoring the duration of a pulse, as shown below in Sec. 4.5.

In Fig. 4.6 it is shown that an increasing thickness improves the resolution of a given crystal. However, since $|b|$ increases quadratically with increasing thickness, it might worsen the resolution when thickness is large enough. For diamond with $\langle 110 \rangle$ surface, which provides the (440) reflection, 10 cm bending radius and $d = 1.2611$, for instance, $|b| = 2$ when the thickness reaches 28 µm. In Fig. 4.10 it is shown how an increasing thickness leads to a wider FWHM of a resolution peak. We see that the thickness increase by a few microns leads to a rapid growth of FWHM of resolution peaks since the tails of the resolution curve surpass the half of the highest value. However, since at each point of detector intensities from each photon energy within a continuous spectrum are integrated, one does not expect an abrupt change of the resolution of a SASE spectral peak in such a case.

A more physical approach to estimate the effect of one photon energy reflection peak on the resolution of SASE spectra would be to average the photon energy shifts over the reflection peak, or the "spread" of the reflection curve. If we have a reflection curve $|R(\Delta E)|^2$, the resolution by spread method will be calculated as

85
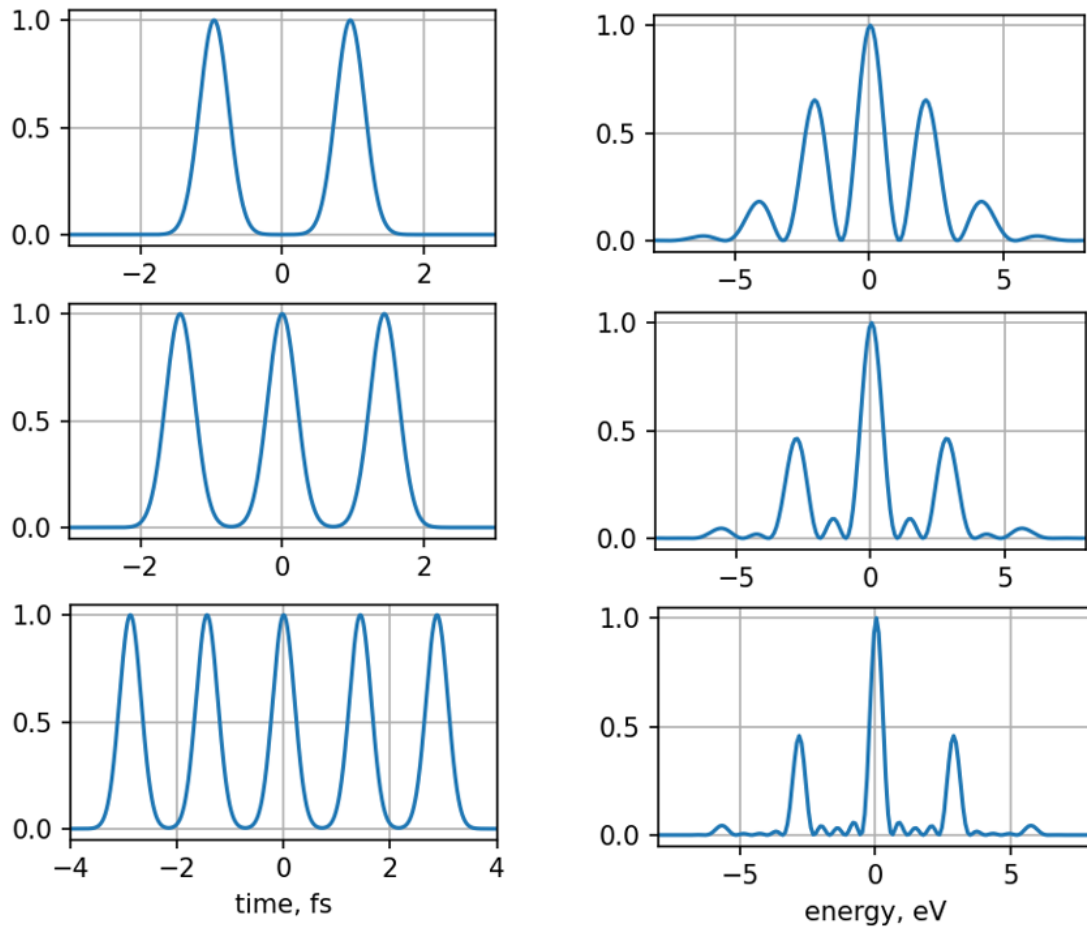
Figure 4.9: Temporal structure of pulses containing various numbers of Gaussian peaks (left) and their spectra (right), mean photon energy 9 keV. An increasing number of peaks in the time structure leads to small narrow peaks. All vertical axes are normalized to the maximum value.

$$w_R = 2 \cdot \frac{\int |R(\Delta E)|^2 |\Delta E| \cdot d\Delta E}{\int |\Delta E| \cdot d\Delta E}. \tag{4.35}$$

.

In Fig. 4.11a) the comparison of the FWHM and spread method widths is shown. The FWHM stops its decrease at around 30 µm. However, due to the rising tails in Fig. 4.10, the FWHM has a sudden rise at around 33 µm despite no sudden rise of the intensity. Since the XFEL spectra are continuous and intensities are summed, the spread width is more physical, and no sudden rise of width is observed. This is confirmed by the resolution of a fraction of SASE spectrum in Fig. 4.11b), where thickness increase from 18 to 30 µm leads to a slightly worse resolution, as one can see from spread method, instead of improvement of resolution, as follows from the decreasing FWHM width with the increasing thickness. In conclusion, there's an optimal crystal
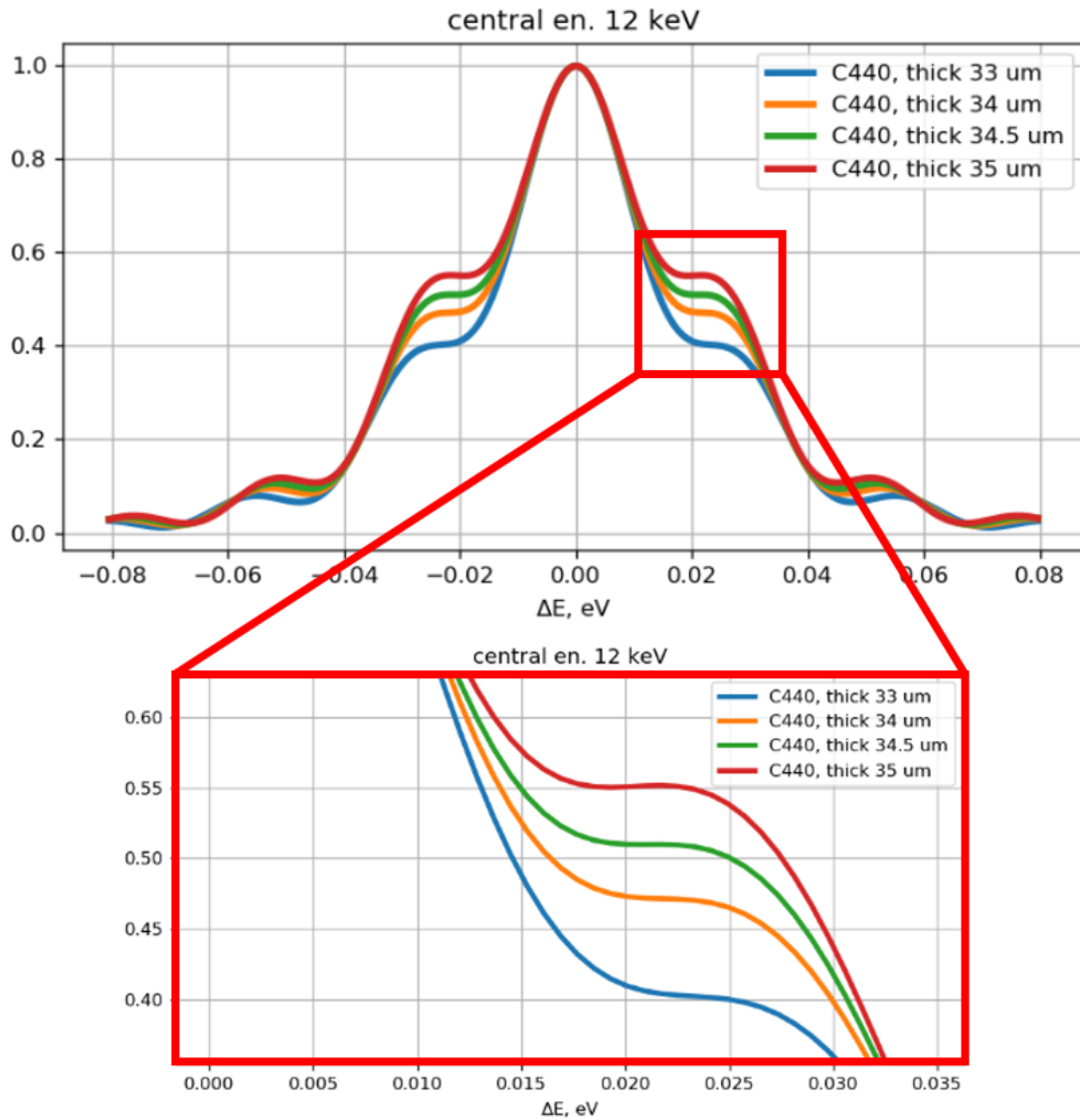
Figure 4.10: Resolution of a single wavelength for different thickness of C(440) crystal with 10 cm bending radius at 12 keV photon energy.

thickness for the best resolution of a crystal bent to given curvature radius. Diamond crystal used at MID instrument of EuXFEL has a thickness of 20 µm and is bent to 10 cm radius, which is within the range of optimal thickness 17-27 µm, as shown in Fig. 4.11.

In order to demonstrate the effect of finite distance propagation described in Sec. 4.3.4, let us simulate the measured spectrum analogous to Fig. 4.8 for C(440) reflection at short distances where the effect of finite distance propagation is expected to be strong. In Fig. 4.12, the spectrum at detector is calculated at 0.3 m, 0.6 m, 1 m, 1.5 m and 2 m. At 0.3 m the diffraction-determined resolution is far from the Fraunhofer limit and the spectral peaks are strongly smeared. Further
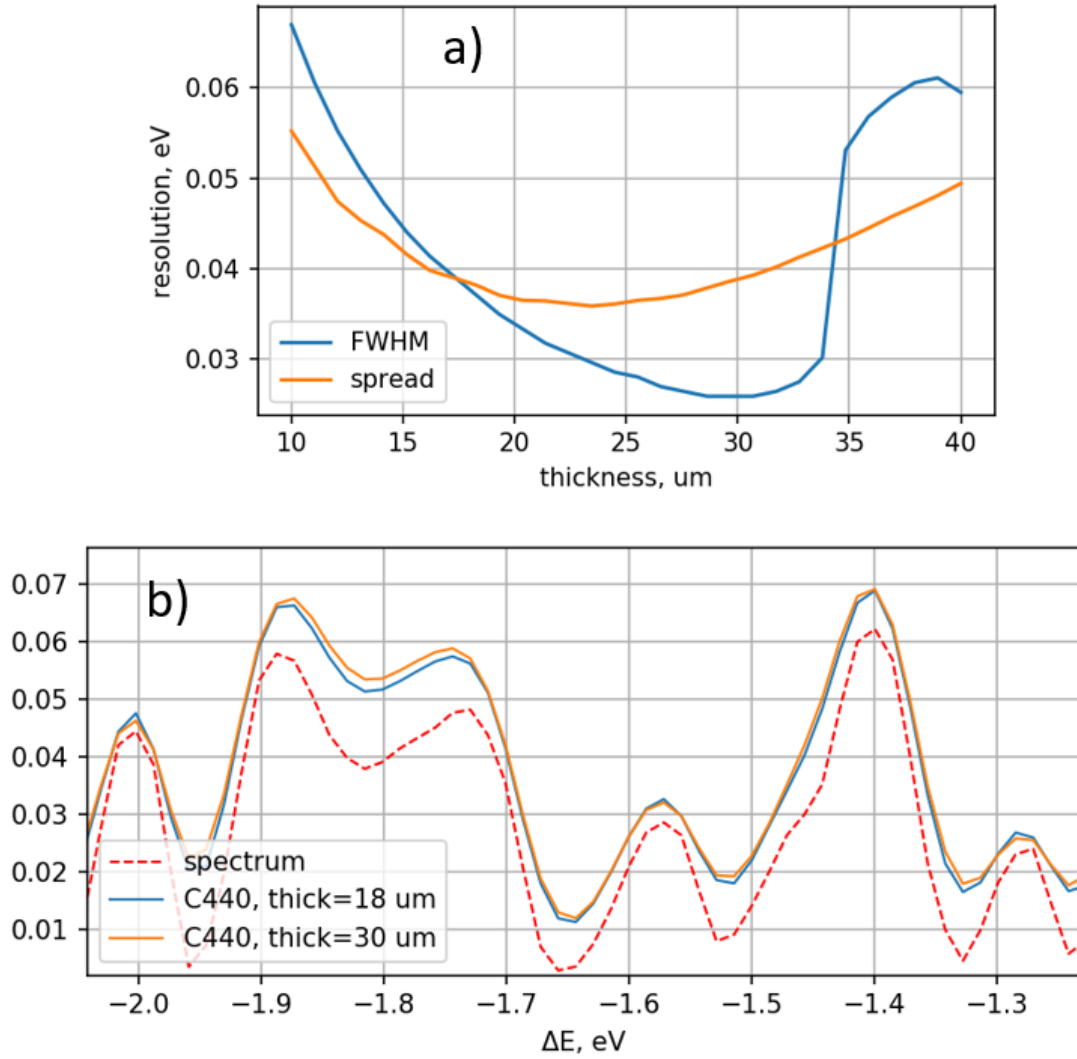
Figure 4.11: a) width of resolution curve of C(440) crystal with 10 cm bending radius for different thicknesses calculated by FWHM and second moment methods, b) resolution of a fraction of SASE spectrum by crystals with two thicknesses. Change of thickness from 18 to 30 µm leads to a slightly worse resolution in b), as one can expect from the spread method in a).

from the crystal, at 0.6 m, the peaks are more similar to the actual spectrum yet many of the fine spectral features are not properly observed. Using Eq. 4.34, the Fraunhofer limit for C(440) at 12.4 keV is reached at $L_{\mathrm{Fr}}^{\mathrm{C}(440)} = 1.44$ m. However, at 1 m most of the fine features are resolved, and further propagation to L_{Fr} and further does not change the recorded spectrum significantly. In summary, at distances of around 70% of L_{Fr} the diffraction-determined resolution reaches the optimal condition. On the other hand, a large distance from the crystal to detector favours the pixel size defined resolution. Figs. 4.8 and 4.12 illustrate the theoretically achievable resolution, i.e. ignoring the finite pixel size of the detector. The horizontal axis corresponds
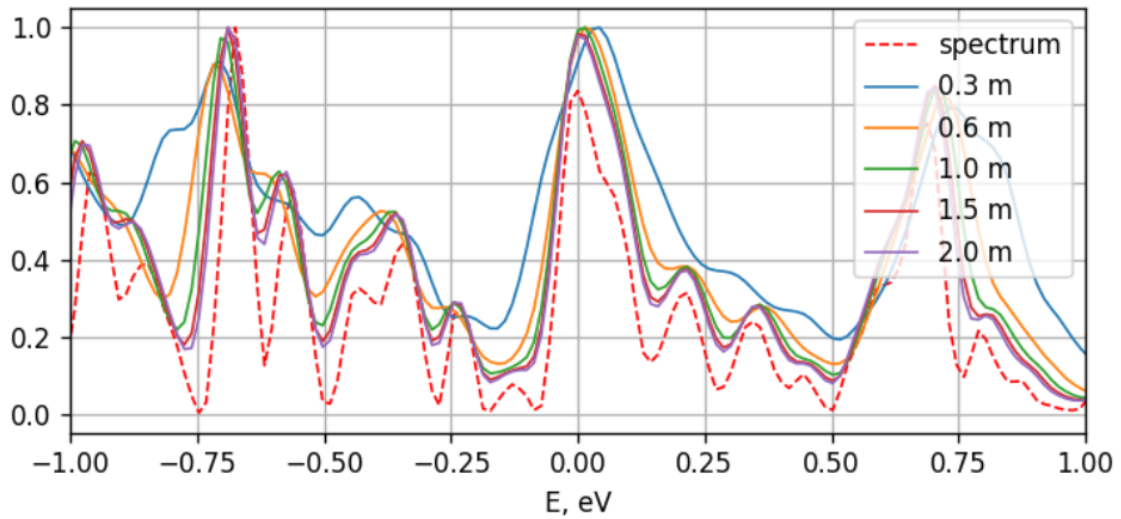
Figure 4.12: The effect of finite distance propagation effect described in Sec. 4.3.4 for C(440) 20 μm thick crystal at 12.4 keV calculated with Eq. 4.31 and Eq. 4.12. SASE spectrum is the same as in Fig. 4.8. The red dashed line is the original spectrum, the solid lines are spectra at detector at various distances, as shown in legend. At short distances, i.e. 0.6 m and 0.3 m , X-rays with different photon energies are overlapping in space more than in the Fraunhofer case in Fig. 4.8, providing a worse resolution. Resolution is similar to the Fraunhofer limit at distances larger than 1 m.

to the reflection angles whose scale is different for different reflections. That is, the resolution

at a given experiment is defined by the detector, the Bragg angle of the reflection and other

parameters.

ref.	material	h	k	l	thickness D	energy E	delta_E calculated	delta_E in paper
					μm	eV	eV	eV
Zhu, APL **101**, 034103 (2012)	Si	1	1	1	10	8330	0.3	0.5
	Si	3	3	3	10	8330	0.1	0.13
Rich, JSR **23**, 3 (2016)	Si	4	4	0	10	8330	0.09	0.15
	Si	2	2	0	20	8330	0.83	
Makita, Optica **2**, 912 (2015)	Si	3	3	3	10	8380	0.14	0.3
	Si	2	2	0	10	8380	0.57	
Boesenberg, Opt.Expr. **25**, 2852 (2017)	C	2	2	0	20	7600	0.17	0.24
	C	4	4	0	20	10500	0.04	0.32
	Si	2	2	0	10	7600	0.24	0.61
	Si	4	4	0	10	7600	0.26	0.32
Kujala, Rev.Sci.Instr. **91**,103101 (2020)	Si	2	2	0	10	9300	0.19	0.55
	Si	4	4	0	10	9300	0.1	0.15
	Si	3	3	3	10	9300	0.12	0.15
	C	2	2	0	20	9300	0.07	0.25

Figure 4.13: Overview of theoretical resolution using Eq. 4.23 for various crystals and the reported experimental resolution in various works.

In Fig. 4.13 a table comparing the experimentally achieved and theoretical resolution using

Eq. 4.23 is shown. Fig. 4.14 shows the figures from papers where resolution is defined. So far, at
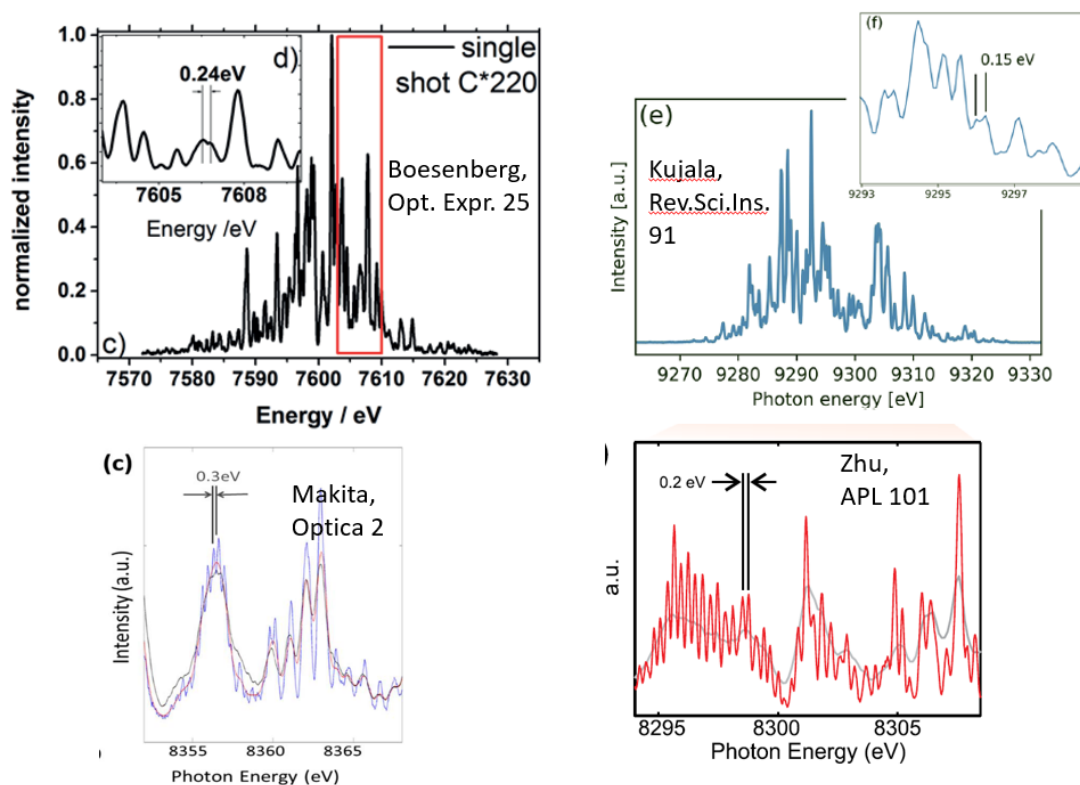
Figure 4.14: Figures from papers in Fig. 4.13 where the experimentally determined resolution is presented.

experiments the demonstrated resolution has not reached values below the theoretical limit of the diffraction-determined resolution provided by Eq. 4.23. In the works mentioned in Fig. 4.13, the resolution was determined from measured spectra using distance between the local peaks that are located the closest to each other. The fact that the separation between the peaks in recorded spectra, whose overview is shown in Fig. 4.14 was observed to be smaller than the diffraction-determined resolution indicates that either the actual peaks in the spectrum were wider than the diffraction-determined resolution or the pixel resolution was not sufficient to measure fine spectral features. Moreover, according to simulations shown in Fig. 3.3b), SASE spectra are expected to have prominent features such that the valleys between spectral peaks reach close to zero, whereas spectra in Fig. 4.14 have wide pedestals. The minimum separation between peaks in measured spectra might be an improper estimation of the device performance, since it is based on a single feature in a single measured spectrum. Statistical analysis of a set of measured spectra analogous to the method presented in Sec. 4.5 would have provided an estimate of the resolution characteristic of the overall device performance.

In order for the diffraction-determined resolution to affect the measured spectrum, the spectral peaks have to be narrower than the diffraction-determined resolution, as shown in Fig. 4.8. Moreover, the detector resolution defined by pixel size needs to be several times better than the diffraction-determined resolution. That way, however, one can neither claim that the spectrum is incorrect nor that it is the actual spectrum. The resolution of elliptical mirror spectrometer shown in Fig. 4.1 is not affected by diffraction, therefore such spectrometer can be used to verify the spectral measurement using bent crystal.

4.5   Tracking of pulse duration using the recorded SASE spectrum

As in any scattering experiment, the bent crystal spectrometer measurement lacks information on the phase of the measured field, providing only the intensity of the electromagnetic wave incident on the detector. Had the phase been feasible to measure, one could do inverse Fourier transform of the measured spectrum and restore the temporal structure of the pulse.

The recorded spectrum intensity can however help estimate the duration of pulses. Under conditions, estimation of peak widths can provide pulse duration, which is crucial for commissioning and facility development, since it provides a quantitative feedback.

One of algorithms for pulse duration estimation involves statistical analysis of a large amount of spectral measurements [76]. Here, the g_2 correlation is used to estimate the average width of peaks in the spectra for each photon energy, which is inversely proportional to the pule duration in time. This relation is dictated by the Fourier-transform relation between the electric field distribution in time and frequency spectrum, such that a longer duration of a pulse leads to narrower peaks in spectrum. If we have a distribution of intensities $I(E)$ for all photon energies E, then calculating

$$g_2(\Delta E, E_0) = \frac{\langle I(E_0)I(E_0 + \Delta E)\rangle}{\langle I(E_0)\rangle\langle I(E_0 + \Delta E)\rangle} \tag{4.36}$$

would provide a correlation of intensities at ΔE photon energy difference from E_0. Here, ΔE is the photon energy difference from E_0, angular brackets denote the average over an ensemble of spectra. That way, if for ΔE^{FWHM} $g_2(\Delta E^{\mathrm{FWHM}}, E_0) = g_2(0, E_0)/2$, it would mean that statistically the peaks of the spectrum have a FWHM of ΔE^{FWHM}. The pulse duration τ_0

is inversely proportional to the peak width: $\tau_0 \sim 1/\Delta E^{\mathrm{FWHM}}$. As discussed in Sec. 3.2, for SASE pulses at EuXFEL [40, 49] the relation $\Delta E \cdot \tau \simeq 2\mathrm{eV} \cdot \mathrm{fs}$ holds, where ΔE is the FWHM of spectra and τ is the pulse duration at FWHM, which follows the Heisenberg's uncertainty principle $\Delta E \cdot \tau \geq \hbar/2 \sim 0.3 \ \mathrm{eV} \cdot \mathrm{fs}$.
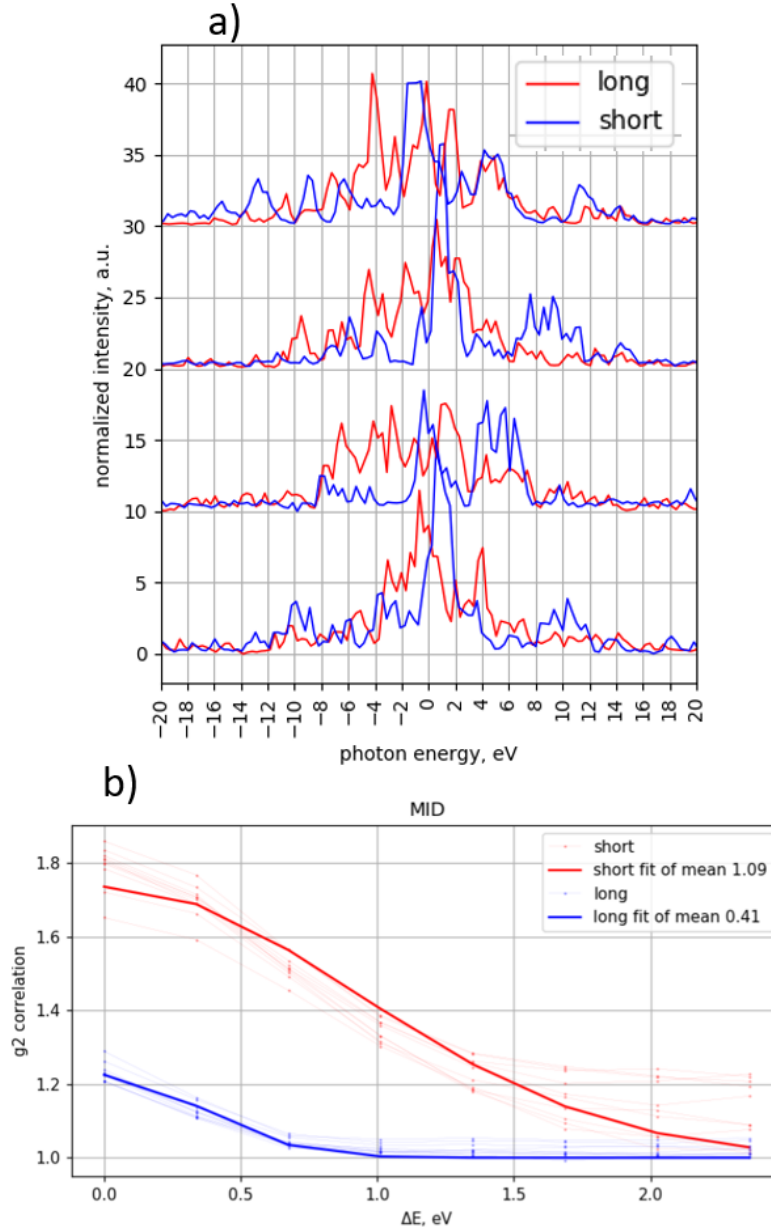
Figure 4.15: a) - sample spectra for short and long pulse modes measured at MID, b) - $g_2(\Delta E, E_0)$ for various E_0 within the measured bandwidth (thin lines) and the Gaussian fit of their mean value over all E_0 (thick lines). Gaussian fit is centered at $\Delta E = 0$. The resolution of the detector was 0.4 eV. The measurements indicate that in short pulse mode the pulse duration is at least 2.65 times shorter compared to long pulse mode.

At the MID instrument, SASE spectra were analysed for two modes of operation using Eq. 4.36. The two modes of operation used different electron bunch compression which was expected to lead to different pulse durations and hence should be visible in the spectrum according to the discussion above. Fig. 4.15 shows the spectra and the g_2 correlations. One can see that the spectra for the short pulse mode have wider peaks and fewer smaller peaks, which leads to a wider g_2 correlation curve. Fig. 4.15b) shows $g_2(\Delta E, E_0)$ curves for various E_0, such that at each photon energy one can calculate the width of g_2 correlation curve. In order to estimate pulse duration in both modes, the average of the g_2 curves over all photon energies is calculated, shown as thick lines in Fig. 4.15b). The width of their Gaussian fits provides a value which is proportional to the pulse duration given sufficient resolution of the detector. The resolution of the detector was 0.4 eV per pixel, therefore the 0.41 eV width of g_2 curve for long pulse mode can only provide the upper limit of pulse duration - the actual peaks in the spectrum could be narrower than 0.41 eV which could not be measured with the spectrometer. Therefore, one can claim that the pulse duration was at least 1.09/0.41=2.65 times bigger in the long pulse mode compared to the short pulse mode. This estimation is valid under the assumption that the pulse had no chirp, i.e. the photon energy was constant at every moment of time. If a pulse has chirp, the photon energy changes along the longitudinal coordinate of the pulse, which increases the width of peaks in the spectrum [76]. A precise estimation of the actual pulse duration would require further information on the electron bunch, e.g. chirp, electron energy distribution in bunch and others, which would probably lead to the deviations from the empirical relation $\Delta E \cdot \tau \simeq 2\,\mathrm{eV}\cdot\mathrm{fs}$ deduced using the database of simulated SASE pulses at European XFEL [49].

At experiment, e.g. during commissioning of novel accelerator and undulator modes, the users require a fast feedback on the change of pulse duration. Instead of applying g2 correlation to every photon energy over a large set of spectra as in Eq. 4.36, one can apply a similar algorithm to a single spectrum. That way, for each ΔE one would average over all photon energies of a single spectrum. Calculating

$$g_2^1(\Delta E) = \frac{\left[I^1(E)I^1(E+\Delta E)\right]}{\left[I^1(E)\right]\left[I^1(E+\Delta E)\right]} \tag{4.37}$$

would provide spectral peak width estimate based on one single spectrum. Here, square brackets denote the averaging over energies of a single spectrum, and $I^1(E)$ denotes that we calculate $g_2^1(\Delta E)$ from a single spectrum.

Let us demonstrate the use of Eq. 4.37 to a set of simulated spectra for various durations of
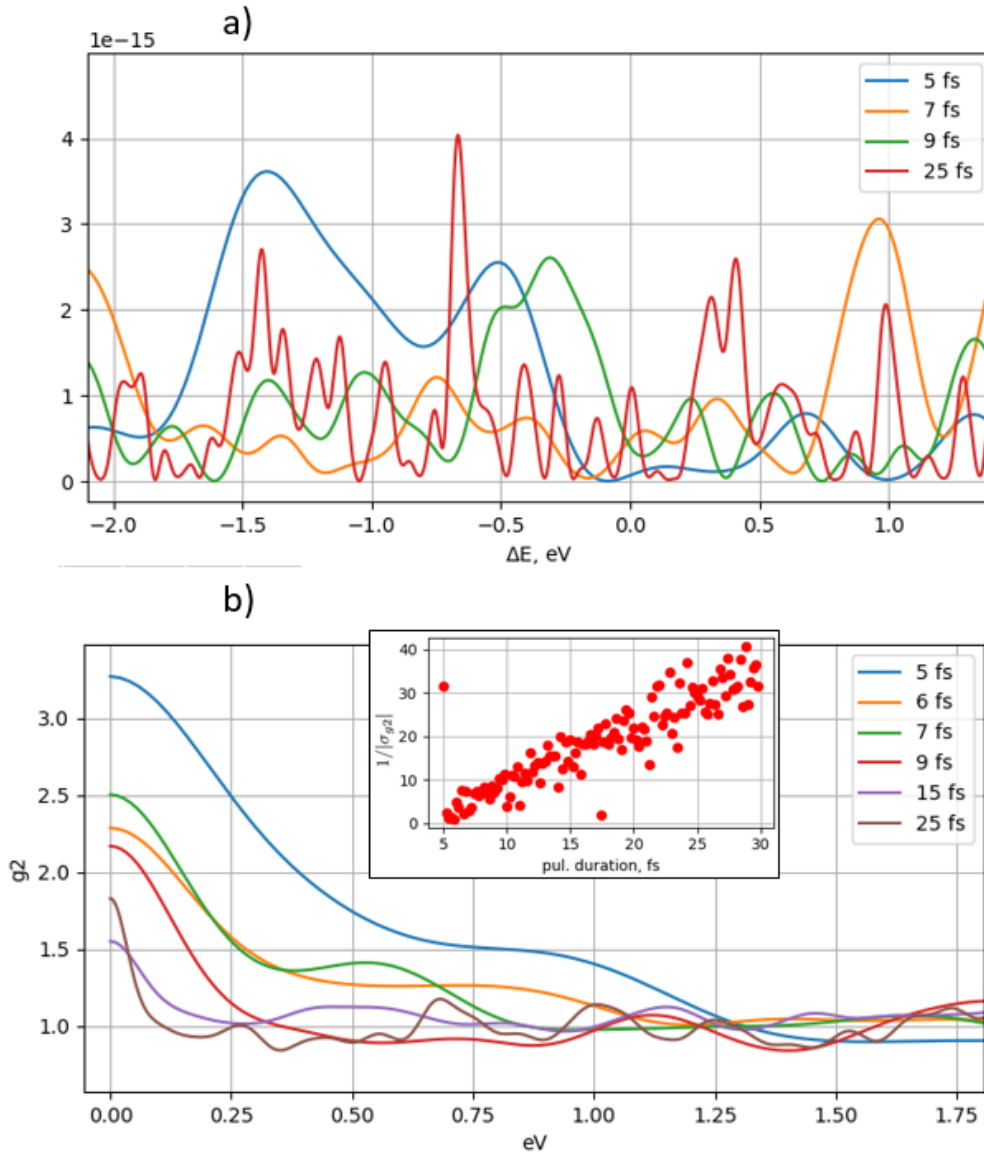
Figure 4.16: Demonstration of pulse duration estimation using a single spectrum. a) - parts of simulated spectra for various pulse durations, b) - g_2^1 calculation for spectra in a), the inset shows the correlation between the pulse duration and the inverse of g_2 peak width. The analysis is based on one spectrum for each pulse duration, as required for single-spectrum pulse duration estimation in Eq. 4.37.

a pulse, from 5 to 30 fs. The spectra in Fig. 4.16a) were simulated using *ocelot* package [77]. Fig. 4.16b) shows the g_2^1 correlations using Eq. 4.37 of spectra of pulses with various durations. The inset shows the correlation between the pulse duration and $1/|\sigma_{g2}|$, where σ_{g2} is the width of the Gaussian fit of g_2^1 curves. One can clearly see the linear correlation, therefore $1/|\sigma_{g2}|$ can be used for on-line pulse duration tracking. As noted above, such method cannot provide an

absolute pulse duration estimation, since the spectra are simulated under assumption of ideal electron beam without chirp. The method using Eq. 4.37 can be used for rough tracking of the change of spectral peaks width. For example, such method would instantly indicate the effect manipulations with the electron bunch have on the pulse duration.

The *ocelot* package used to simulate spectra in Fig. 4.16 provides spectra of pulses at low saturation and in the absence of energy chirp. The latter would, for instance, increase the width of spectral features without shortening the pulse in time. Such factors, which affect the measured spectrum, would make the above presented method invalid for the pulse duration tracking. However, the spectral peak width acquired from single spectra would provide a live feedback on how the changes in the beam and undulator parameters affect the spectrum.

4.6   Conclusions

The model presented in this chapter allows to estimate the effect of diffraction on the spectrometer resolution. Firstly, for the given reflection, crystal thickness and pulse properties, the best achievable resolution can be calculated. This is the resolution of the bent crystal in Fraunhofer limit, i.e. at a sufficiently large distance. This resolution is defined by the crystal, such that even if a given detector allows for higher resolution, the width of peaks in the measured spectrum will be limited by the diffraction-determined resolution. Therefore, if one does not account for the limitation of resolution due to diffraction, the peaks in measured spectra might be misleading in a way that they would appear wider than in the actual spectrum, even if the detector allows for a high resolution. Secondly, the model allows to simulate the effect a short distance from crystal to detector has on the measured spectrum. At sufficiently short distances, in the Fresnel limit, the peaks in the measured spectrum are much broader than in the case of Fraunhofer limit, when the detector is located far from crystal. The model allows to estimate whether for the given experimental setup the Fresnel limit affects the measured spectrum and to estimate whether it is feasible to restore the actual width of peaks from the measured ones. A set of experimental data was analyzed to compare the pulse duration in various machine settings, which indicated at least a twofold difference in pulse duration. A method for an estimation of an average peak width in a single spectrum was proposed, which can be used for a rough estimation of the changes of the spectral peak width which might be useful for a quick online feedback about the changes of the pulse duration.

Conclusions and implications

Crystal optics are widely used at modern hard X-ray sources, such as synchrotrons and XFELs. Several novel theoretical studies have been carried out, which provide pioneer insights into various problems of diffraction in crystals at XFELs. The operation of a strongly bent crystal spectrometer applied to XFEL pulses has been studied using the theory of diffraction for the first time, and an intrinsic limit of resolving power of strongly bent crystals was derived among other significant effects. These findings provide a profound physical understanding of the spectrometer device which might become crucial for evaluating experimentally measured XFEL spectra. Also, asymmetric diffraction has been shown to be potentially beneficial for coherent scattering experiments, enabling to overcome the restrictions of conventional experimental techniques. Moreover, a simulation model for the crystal heating under intense XFEL radiation has been presented, applied to the cryogenically cooled silicon monochromator at EuXFEL and tested at an experiment.

Strongly bent crystals are used as single shot spectrometers for hard X-ray FEL pulses because of their effective dispersion. Previously, resolution of strongly bent crystals was mostly considered from a geometrical point of view, without taking diffraction effects into consideration. In Chapter 4, a profound theory of diffraction in such optical devices has been presented, which gives a profound understanding of the XFEL pulses diffraction in these devices. In the Section 4.4 it was shown that for the given photon energy of X-rays and for the given crystal parameters, there exists an intrinsic resolution of a strongly bent crystal defined by diffraction effects. This intrinsic resolution is given by the ratio of the interplanar spacing of a given reflection and the crystal thickness. The intrinsic resolution means that even for a detector with a pixel size which would enable a geometrical resolution finer than the intrinsic resolution, the spectrum would be smeared due to diffraction and no improvement in resolution would be seen. This was simulated to have an effect for instance in resolving EuXFEL SASE pulses generated by 500 pC bunches at 12.4 keV whose spectra have narrow 0.05 eV features. A C(440) 20 µm thick crystal bent to

a radius of 10 cm has an intrinsic resolution of around 0.04 eV at 12.4 keV, which was shown to be insufficient to resolve fine spectral features.

In Sec. **??**, prospects of the application of asymmetric diffraction to coherent scattering experiments are explored. Since FEL pulses have a high degree of transverse coherence, sub-mm size and fs duration, an effect of wavefront inclination relative to the propagation of direction can be expected. That way, the surface of constant phase is at angle to the wavevector. When incident at a scattering sample, the optical path difference is minimal in the direction perpendicular to the phase front. This direction corresponds to a non-zero momentum transfer defined by the wavefront inclination angle, such that the lengthscale of the structural studies is shorter than in conventional scattering techniques. This has a potential of expanding the capabilities of coherent scattering experiments, such as XPCS or Coherent Diffraction Imaging (CDI), down to interatomic distances.

The high intensity and high repetition rates of pulses at EuXFEL poses challenges on crystal optics due to the exceptional heat load. In particular, silicon monochromators can undergo elastic deformations under the XFEL radiation which amounts to several hundreds of watts. In order to mitigate the heating, cryogenic cooling is used to minimize the deformation and dissipate the heat. In Section 2.3, a simple one-dimensional model of heating was developed which allows to simulate the deformation of the crystal under cryogenic conditions illuminated by intense XFEL pulses. The developed tool does not require finite-element studies, which usually require commercial software and can be complex to operate. In Section 3.3, dynamical diffraction equations that assume the temperature at crystal surface were applied to the heating model which allowed to simulate the performance of a cryogenically cooled silicon monochromator under MHz x-ray pulses with sub-mJ energy. It was shown that under 675 W heat load the monochromator transmission decreases to approximately 50% of the initial value after 60 µs. Diamond, due to its exceptional heat conductivity and low absorption, is a promising material for crystal optics at XFELs with high intensity of pulses. Considerations concerning continuous wave (CW) operation mode of XFEL were presented and challenges of crystal optics heating in such regime are discussed. Due to the decreasing heat transfer capabilities with increasing temperature and due to a Gaussian intensity profile of the pulses, a non-uniform heat distribution over the crystal will lead to unsustainable CW operation when the heat load is on the order of hundreds of watts.

Acknowledgements

I am thankful to my supervisors Liubov Samoylova and Anders Madsen for the extensive support and assistance during the PhD project. I am grateful to Harald Sinn and Maurizio Vannoni for the supervision and numerous discussions on the diffraction and heating effects. I am grateful to my colleagues from MID instrument, X-ray Optics group and other teams of European XFEL for their dedication and scientific expertise that enabled outstanding theoretical and experimental research results. I am thankful to Vladimir Kaganer, whose expertise in X-ray diffraction is behind the theory of diffraction in strongly bent crystals.

Bibliography

[1] B. McNeil and N. Thompson, "X-ray free-electron lasers", Nature Photonics **4** (2010).

[2] E. L. Saldin, E. A. Schneidmiller, and M. V. Yurkov, *The Physics of Free Electron Lasers* (Springer, Berlin, 2000).

[3] W. Decking, S. Abeghyan, P. Abramian, A. Abramsky, A. Aguirre, C. Albrecht, P. Alou, M. Altarelli, P. Altmann, K. Amyan, et al., "A MHz-repetition-rate hard X-ray free-electron laser driven by a superconducting linear accelerator", Nature Photonics **14**, 391–397 (2020).

[4] F. Brinker, "Commissioning of the European XFEL Injector", in Proc. of International Particle Accelerator Conference (IPAC'16), Busan, Korea, May 8-13, 2016, International Particle Accelerator Conference 7 (June 2016), pp. 1044–1047.

[5] P. Emma, R. Akre, J. Arthur, R. Bionta, C. Bostedt, J. Bozek, A. Brachmann, P. Bucksbaum, R. Coffee, F.-J. Decker, Y. Ding, D. Dowell, S. Edstrom, A. Fisher, J. Frisch, S. Gilevich, J. Hastings, G. Hays, P. Hering, and J. Galayda, "First lasing and operation of an Ångstrom-wavelength free-electron laser", Nature Photonics **4**, 641–647 (2010).

[6] T. Ishikawa, H. Aoyagi, T. Asaka, Y. Asano, N. Azumi, T. Bizen, H. Ego, K. Fukami, T. Fukui, Y. Furukawa, S. Goto, H. Hanaki, T. Hara, T. Hasegawa, T. Hatsui, A. Higashiya, T. Hirono, N. Hosoda, M. Ishii, and N. Kumagai, "A compact X-ray free-electron laser emitting in the sub-ångström region", Nature Photonics **6**, 540–544 (2012).

[7] P. Emma et al., "Linear Accelerator Design for the LCLS-II FEL Facility", in Proc. 36th Int. Free Electron Laser Conf. (FEL'14) (Aug. 2014), pp. 743–747.

[8] Z. Zhao, D. Wang, Z. Yang, and L. Yin, "SCLF: An 8-GeV CW SCRF Linac-Based X-Ray FEL Facility in Shanghai", in Proc. of International Free Electron Laser Conference (FEL'17), Santa Fe, NM, USA, August 20-25, 2017, International Free Electron Laser Conference 38 (Feb. 2018), pp. 182–184.

[9] M. Dunne, "X-ray free-electron lasers light up materials science", Nature Reviews Materials **3** (2018).

[10] J. Amann, W. Berg, V. Blank, F.-J. Decker, Y. Ding, P. Emma, Y. Feng, J. Frisch, D. Fritz, J. Hastings, Z. Huang, J. Krzywinski, R. Lindberg, H. Loos, A. Lutman, H.-D. Nuhn, D. Ratner, J. Rzepiela, D. Shu, and D. Zhu, "Demonstration of self-seeding in a hard-x-ray free-electron laser", Nature Photonics **6**, 693–698 (2012).

[11] G. Geloni, V. Kocharyan, and E. Saldin, "A novel self-seeding scheme for hard X-ray FELs", Journal of Modern Optics **58**, 1391–1403 (2011).

[12] I. Inoue, T. Osaka, T. Hara, T. Tanaka, T. Inagaki, T. Fukui, S. Goto, Y. Inubushi, H. Kimura, R. Kinjo, H. Ohashi, K. Togawa, K. Tono, M. Yamaga, H. Tanaka, T. Ishikawa, and M. Yabashi, "Generation of narrow-band X-ray free-electron laser via reflection self-seeding", Nature Photonics **13**, 1 (2019).

[13] J. Zemella, "Untersuchungen zu einem Freie-Elektronen-Laser-Oszillator fuer den European XFEL", University of Hamburg, Diss., 2013, Dr. (University of Hamburg, DESY, 2013).

[14] K.-J. Kim and Y. V. Shvyd'ko, "Tunable optical cavity for an x-ray free-electron-laser oscillator", Phys. Rev. ST Accel. Beams **12**, 030703 (2009).

[15] K. Li and H. Deng, "Gain cascading scheme of a free-electron-laser oscillator", Physical Review Accelerators and Beams **20** (2017).

[16] A. Madsen, J. Hallmann, G. Ansaldi, T. Roth, W. Lu, C. Kim, U. Boesenberg, A. Zozulya, J. Möller, R. Shayduk, M. Scholz, A. Bartmann, A. Schmidt, I. Lobato, K. Sukharnikov, M. Reiser, K. Kazarian, and I. Petrov, "Materials Imaging and Dynamics (MID) instrument at the European X-ray Free-Electron Laser Facility", Journal of Synchrotron Radiation **28**, 637–649 (2021).

[17] A. Madsen, A. Fluerasu, and B. Ruta, "Structural dynamics of materials probed by x-ray photon correlation spectroscopy", in *Synchrotron light sources and free-electron lasers: accelerator physics, instrumentation and science applications* (Springer International Publishing, Cham, 2016), pp. 1617–1641.

[18] F. Lehmkühler, J. Valerio, D. Sheyfer, W. Roseker, M. A. Schroer, B. Fischer, K. Tono, M. Yabashi, T. Ishikawa, and G. Grübel, "Dynamics of soft nanoparticle suspensions at hard X-ray FEL sources below the radiation-damage threshold", IUCrJ **5**, 801–807 (2018).

[19] A. H. Zewail, "Femtochemistry: atomic-scale dynamics of the chemical bond", The Journal of Physical Chemistry A **104**, 5660–5694 (2000).

[20] M. Chergui and A. H. Zewail, "Electron and X-Ray Methods of Ultrafast Structural Dynamics: Advances and Applications", ChemPhysChem **10**, 28–43 (2009).

[21] H. Chapman, P. Fromme, A. Barty, T. White, R. Kirian, A. Aquila, M. Hunter, J. Schulz, D. DePonte, U. Weierstall, R. Doak, F. Maia, A. Martin, I. Schlichting, L. Lomb, N. Coppola, R. Shoeman, S. Epp, R. Hartmann, and J. Spence, "Femtosecond X-ray protein nanocrystallography", Nature **470**, 73–7 (2011).

[22] K.-J. Kim, Y. Shvyd'ko, and S. Reiche, "A Proposal for an X-Ray Free-Electron Laser Oscillator with an Energy-Recovery Linac", Phys. Rev. Lett. **100**, 244802 (2008).

[23] X. Dong, D. Shu, and H. Sinn, "Design of a cryo-cooled artificial channel-cut crystal monochromator for the European XFEL", AIP Conference Proceedings **1741**, 040027 (2016).

[24] I. Petrov, U. Boesenberg, J. H. V. A. Bushuev, K. Kazarian, W. Lu, J. Möller, M. Reiser, A. Rodriguez-Fernandez, L. Samoylova, M. Scholz, H. Sinn, A. Zozulya, and A. Madsen, "Performance of a cryo-cooled crystal monochromator illuminated by hard X-rays with MHz repetition rate at the European X-ray Free-Electron Laser", Optics Express (2022).

[25] M. Born and E. Wolf, *Principles of optics* (Pergamon, London, 1964).

[26] A. Authier, *Dynamical Theory of X-Ray Diffraction* (Oxford, 2004).

[27] W. H. Zachariasen, *Theory of X-ray Diffraction in Crystals* (Wiley, 1945).

[28] V. A. Bushuev, "Effect of the thermal heating of a crystal on the diffraction of pulses of a free-electron X-ray laser", Bulletin of the Russian Academy of Sciences: Physics **77** (2013).

[29] V. A. Bushuev, "Influence of thermal self-action on the diffraction of high-power x-ray pulses", Journal of Surface Investigation. X-ray, Synchrotron and Neutron Techniques **10**, 1179–1186 (2016).

[30] H. Sinn, M. Dommach, X. Dong, D. La Civita, L. Samoylova, R. Villanueva, and F. Yang, "Technical Design Report: X-Ray Optics and Beam Transport", Technical Report (2012).

[31] https://github.com/ia-petrov/cryst-heat-load.

[32] H. Sinn, "Heat load estimates for XFEL beamline optics", HASYLAB Annual Report 2007 (2007).

[33] P. Debye, "Zur Theorie der spezifischen Wärmen", Annalen der Physik **344**, 789–839 (1912).

[34] C. J. Glassbrenner and G. A. Slack, "Thermal Conductivity of Silicon and Germanium from 3°K to the Melting Point", Phys. Rev. **134**, A1058–A1069 (1964).

[35] Y. Okada and Y. Tokumaru, "Precise determination of lattice parameter and thermal expansion coefficient of silicon between 300 and 1500 K", Journal of Applied Physics **56**, 314–320 (1984).

[36] *FAST-XPD: XFEL photon pulses database*, `https://in.xfel.eu/fastxpd/`, 2020.

[37] A. G. Shabalin, O. M. Yefanov, V. L. Nosik, V. A. Bushuev, and I. A. Vartanyants, "Dynamical effects in Bragg coherent x-ray diffraction imaging of finite crystals", Phys. Rev. B **96**, 064111 (2017).

[38] L. Samoylova, A. Buzmakov, O. Chubar, and H. Sinn, "*WavePropaGator*: interactive framework for X-ray free-electron laser optics design and simulations", Journal of Applied Crystallography **49**, 1347–1355 (2016).

[39] E. Saldin, E. Schneidmiller, and M. Yurkov, ""FAST: a three-dimensional time-dependent FEL simulation code"", Nucl. Instrum. Meth. A **429**, 233–237 (1999).

[40] M. Manetti, A. Buzmakov, L. Samoylova, E. Schneidmiller, H. Sinn, J. Szuba, K. Wrona, and M. Yurkov, "FAST-XPD: XFEL photon pulses database for modeling XFEL experiments", AIP Conference Proceedings **2054**, 030019 (2019).

[41] V. A. Bushuev, "Diffraction of X-ray free-electron laser femtosecond pulses on single crystals in the Bragg and Laue geometry", Journal of Synchrotron Radiation **15**, 495–505 (2008).

[42] Y. Sun, N. Wang, S. Song, P. Sun, M. Chollet, T. Sato, T. B. van Driel, S. Nelson, R. Plumley, J. Montana-Lopez, S. W. Teitelbaum, J. Haber, J. B. Hastings, A. Q. R. Baron, M. Sutton, P. H. Fuoss, A. Robert, and D. Zhu, "Compact hard x-ray split-delay system based on variable-gap channel-cut crystals", Opt. Lett. **44**, 2582–2585 (2019).

[43] A. Souvorov, M. Drakopoulos, I. Snigireva, and A. Snigirev, "Asymmetrically cut crystals as optical elements for coherent x-ray beam conditioning", Journal of Physics D: Applied Physics **32**, A184–A192 (1999).

[44] D. Salerno, D. Brogioli, F. Croccolo, R. Ziano, and F. Mantegazza, "Photon correlation spectroscopy with incoherent light", Opt. Express **19**, 26416–26422 (2011).

[45]O. Chubar, M.-E. Couprie, M. Labat, G. Lambert, F. Polack, and O. Tcherbakoff, "Time-dependent FEL wavefront propagation calculations: fourier optics approach", Nuclear Instruments and Methods in Physics Research Section A: Accelerators, Spectrometers, Detectors and Associated Equipment **593**, FEL Fronties 2007, 30–34 (2008).

[46]R. Rüffer and A. Chumakov, "Nuclear-resonance beamline at esrf", Hyperfine Interact. **97-98**, 589–604 (1996).

[47]A. Plech, R. Randler, A. Geis, and M. Wulff, "Diffuse scattering from liquid solutions with white-beam undulator radiation for photoexcitation studies", Journal of Synchrotron Radiation **9**, 287–292 (2002).

[48]P. Duthil, *Material properties at low temperature*, 2014.

[49]E. L. Saldin, E. A. Schneidmiller, and M. V. Yurkov, "FAST: a three-dimensional time-dependent FEL simulation code", Nucl. Instrum. Meth. A **429**, 233–237 (1999).

[50]E. Schneidmiller and M. Yurkov, "An Overview of the Radiation Properties of the European XFEL", in Proc. FEL2014 Conference, Basel, Switzerland, mop066 (2014).

[51]O. Chubar, G. Geloni, V. Kocharyan, A. Madsen, E. Saldin, S. Serkez, Y. Shvyd'ko, and J. Sutter, "Ultra-high-resolution inelastic X-ray scattering at high-repetition-rate self-seeded X-ray free-electron lasers", Journal of Synchrotron Radiation **23**, 410–424 (2016).

[52]"Megapixels @ Megahertz – The AGIPD high-speed cameras for the European XFEL", Nuclear Instruments and Methods in Physics Research Section A: Accelerators, Spectrometers, Detectors and Associated Equipment **942**, 162324 (2019).

[53]T. Maltezopoulos, F. Dietrich, W. Freund, U. F. Jastrow, A. Koch, J. Laksman, J. Liu, M. Planas, A. A. Sorokin, K. Tiedtke, and J. Grünert, "Operation of X-ray gas monitors at the European XFEL", Journal of Synchrotron Radiation **26**, 1045–1051 (2019).

[54]T. Roth, L. Helfen, J. Hallmann, L. Samoylova, P. Kwaśniewski, B. Lengeler, and A. Madsen, "X-ray laminography and SAXS on beryllium grades and lenses and wavefront propagation through imperfect compound refractive lenses", in Advances in x-ray/euv optics and components ix, Vol. 9207 (2014), pp. 1–12.

[55]E. Saldin, E. Schneidmiller, and M. Yurkov, "Statistical properties of radiation from VUV and X-ray free electron laser", Optics Communications **148**, 383–403 (1998).

[56]I. Petrov, J. Anton, U. Boesenberg, M. Dommach, X. Dong, J. Eidam, J. Hallmann, K. Kazarian, S. Kearney, C. Kim, W. Lu, A. Madsen, J. Möller, M. Reiser, L. Samoylova, R. Shayduk, D. Shu, H. Sinn, V. Sleziona, and A. Zozulya, "Effect of Heat Load on Cryo-Cooled Monochromators at the European X-Ray Free-Electron Laser: Simulations and First Experimental Observations", in Proc. FEL'19 (Nov. 2019), pp. 502–505.

[57]D. Prikhodko, S. Tarelkin, V. Bormashov, A. Golovanov, M. Kuznetsov, D. Teteruk, A. Volkov, and S. Buga, "Thermal conductivity of synthetic boron-doped single-crystal HPHT diamond from 20 to 400 K", MRS Communications **-1**, 1–6 (2016).

[58]E. Burgemeister, "Thermal conductivity of natural diamond between 320 and 450 K", Physica B+C **93**, 165–179 (1978).

[59]Y. Shvyd'ko, S. Terentyev, V. Blank, and T. Kolodziej, "Diamond channel-cut crystals for high-heat-load beam-multiplexing narrow-band X-ray monochromators", Journal of Synchrotron Radiation **28**, 1720–1728 (2021).

[60]A. Mozzanica, A. Bergamaschi, R. Dinapoli, H. Graafsma, D. Greiffenberg, B. Henrich, I. Johnson, M. Lohmann, R. Valeria, B. Schmitt, and S. Xintian, "The GOTTHARD charge integrating readout detector: design and characterization", Journal of Instrumentation **7**, C01019–C01019 (2012).

[61]N. Kujala, W. Freund, J. Liu, A. Koch, T. Falk, M. Planas, F. Dietrich, J. Laksman, Maltezopoulos, Th., J. Risch, F. Dall'Antonia, and J. Grünert, "Hard x-ray single-shot spectrometer at the European X-ray Free-Electron Laser", **91**, 103101 (2020).

[62]U. Boesenberg, L. Samoylova, T. Roth, D. Zhu, S. Terentyev, M. Vannoni, Y. Feng, T. B. van Driel, S. Song, V. Blank, H. Sinn, A. Robert, and A. Madsen, "X-ray spectrometer based on a bent diamond crystal for high repetition rate free-electron laser applications", Optics Express **25**, 2852–2861 (2017).

[63]D. Zhu, M. Cammarata, J. M. Feldkamp, D. M. Fritz, J. B. Hastings, S. Lee, H. T. Lemke, A. Robert, J. L. Turner, and Y. Feng, "A single-shot transmissive spectrometer for hard x-ray free electron lasers", Appl. Phys. Lett. **101**, 034103 (2012).

[64]D. Rich, D. Zhu, J. Turner, D. Zhang, B. Hill, and Y. Feng, "The LCLS variable-energy hard X-ray single-shot spectrometer", J. Synchrotron Rad. **23**, 3–9 (2016).

[65] M. Makita, P. Karvinen, D. Zhu, P. N. Juranic, J. Gruenert, S. Cartier, J. H. Jungmann-Smith, H. T. Lemke, A. Mozzanica, S. Nelson, L. Patthey, M. Sikorski, S. Song, Y. Feng, and C. David, "High-resolution single-shot spectral monitoring of hard x-ray free-electron laser radiation", Optica **2**, 912–916 (2015).

[66] C. David, G. Seniutinas, M. Makita, B. Rösner, J. Rehanek, P. Karvinen, F. Löhl, R. Abela, L. Patthey, and P. Juranić, "Spectral monitoring at SwissFEL using a high-resolution on-line hard X-ray single-shot spectrometer", Journal of Synchrotron Radiation **28**, 1978–1984 (2021).

[67] Y. Inubushi, K. Tono, T. Togashi, T. Sato, T. Hatsui, T. Kameshima, K. Togawa, T. Hara, T. Tanaka, H. Tanaka, T. Ishikawa, and M. Yabashi, "Determination of the Pulse Duration of an X-Ray Free Electron Laser Using Highly Resolved Single-Shot Spectra", Phys. Rev. Lett. **109**, 144801 (2012).

[68] V. M. Kaganer, I. Petrov, and L. Samoylova, "X-ray diffraction from strongly bent crystals and spectroscopy of X-ray free-electron laser pulses", Acta Cryst. A **76**, 55–69 (2020).

[69] V. M. Kaganer, I. Petrov, and L. Samoylova, "Resolution of a bent-crystal spectrometer for X-ray free-electron laser pulses: diamond versus silicon", Acta Crystallographica Section A **77**, 268–276 (2021).

[70] G. Geloni, E. Saldin, L. Samoylova, E. Schneidmiller, H. Sinn, T. Tschentscher, and M. Yurkov, "Coherence properties of the European XFEL", New Journal of Physics **12**, 035021 (2010).

[71] M. Born and E. Wolf, *Principles of optics* (Cambridge University Press, Cambridge, 2019).

[72] L. D. Landau and E. M. Lifshitz, *Electrodynamics of Continuous Media* (Pergamon Press, London, U.K., 1984).

[73] B. Lengeler, C. Schroer, J. Tümmler, B. Benner, M. Richwin, A. Snigirev, I. Snigireva, and M. Drakopoulos, "Imaging by parabolic refractive lenses in the hard X-ray range", Journal of Synchrotron Radiation **6**, 1153–1167 (1999).

[74] S. Terentyev, V. Blank, T. Kolodziej, and Yu. Shvyd'ko, "Curved diamond-crystal spectrographs for x-ray free-electron laser noninvasive diagnostics", Rev. Sci. Instr. **87**, 125117 (2016).

[75] H. J. McSkimin and P. Andreatch, "Elastic Moduli of Diamond as a Function of Pressure and Temperature", Journal of Applied Physics **43**, 2944–2948 (1972).

[76]S. Serkez, O. Gorobtsov, B. Sobko, N. Gerasimova, and G. Geloni, *ROSA: Reconstruction of Spectrogram Autocorrelation for Self-Amplified Spontaneous Emission Free-Electron Lasers*, 2018.

[77]I. Agapov, G. Geloni, S. Tomin, and I. Zagorodnov, "OCELOT: A software framework for synchrotron light source and FEL studies", Nuclear Instruments and Methods in Physics Research Section A: Accelerators, Spectrometers, Detectors and Associated Equipment **768**, 151–156 (2014).